Control of Optical Properties of Oxynitride Pigments and Phosphors

(酸窒化物顔料および蛍光体の光学特性の制御に関する研究)

SARDA NARENDRA GIRISH

Doctoral dissertation

Department of Chemical Science and Technology

Graduate School of Advanced Technology and Science

Tokushima University, Japan.

September 2016

Declaration

I certify that this work was carried out at the Department of Chemistry at University of Tokushima, Japan. This thesis contains no material which has been accepted for the award of any other degree in my name, in any university or other tertiary institute and to the best of my knowledge and belief, contains no material previously published or written by another person, except where due reference has been made in the text. Prior to the submission of this thesis, some work has been published as described in the relevant chapters herein.

Name – SARDA NARENDRA GIRISH Student Id Number - 5013430035

Signature –

Date -

Acknowledgement

I wish to show sincere appreciations to all those who have been supporting me during the past three years in Tokushima, Japan. I would like to express my special appreciation and thanks to my supervisor, Professor Dr. Toshihiro Moriga, he has been a tremendous mentor for me. I would like to thank him for encouraging my research and for allowing me to grow as a research scientist. His advice on both research as well as on my career have been invaluable. Because of his great support, I could get this great opportunity to work as a PhD student at University of Tokushima, Japan. Second, I would like to express my heartfelt gratitude to Professor. Geoffrey I. N. Waterhouse (Auckland University New Zealand) for discussing my scientific results and giving helpful advices to improve my scientific publications.

I would also like to thanks all the members of C-1 laboratory, in particular very deep thanks to Prof. Kei-ichiro Murai for his kind help. I would like to thanks Satoshi, Minami, and Hayashi for teaching me to use all the instruments which I have been used in my three years study; also I would like to thank Takeuchi, Harada and Namiko for their support in my experimental work. I am really grateful to Dr. Pankaj Koinkar and Koinkar family for supporting and taking care of me and treating me as a family member, because of them I could able to live in Japan away from my family. I would like to thank Dr. Amalnerkar and Late Dr. S.G.Joshi for recommending me Tokushima University also giving me valuable guidance whenever needed.

Last but not least, a special thanks to my parents. Mom and Dad, you have given me the greatest gift of all, education and the freedom of my choice. Words cannot express how grateful I am to my Grandma, Parents, Sister, Brother-in-law, Niece Mehek and many friends for their constant support, understanding and for being so close to me even while living so far away.

Table of Contents

List of Tables

Table **Page**

List of Figures

Figures **Page**

List of Papers

This thesis is based on the following papers:

- **Narendra G. Sarda**, Minami Omune, Takanori Hayashi, Andrew Chan, Satoshi Kataoka, Kei-Ichiro Murai, Geoffrey I.N. Waterhouse, Toshihiro Moriga, "Structural and optical properties of perovskite-type $LaTiO_2N$ synthesized using urea or thiourea as co-nitriding agents" Journal of European Ceramic Society, Volume 35, PP.3311-3317 (2015). **http://dx.doi.org/10.1016/j.jeurceramsoc.2015.02.019**
- **Narendra G. Sarda,** Hiroshi Fujigaki, Yuma Ogita, Andrew Chan, Kei-ichiro Murai, Toshihiro Moriga, Geoffrey I.N. Waterhouse, "Photoluminescence Properties of $(Ba_{1-(x+y)}Sr_xEu_y)_2Si_6O_{12}N_2$ Phosphors for White LED Applications" Journal of Nano Research, Volume 36, PP.1-7 (2016) **doi: 10.4028/www.scientific.net/JNanoR.36**
- **Narendra G. Sarda**, Takanori Hayashi, Andrew Chan, Yuta Takeuchi, Kyosuke Harada, Kei-Ichiro Murai, Geoffrey I.N. Waterhouse, Toshihiro Moriga, "Synthesis and Optical Studies of $La_{1.1}Ti_{1-x}W_x(O,N)_3$ Prepared by Sol-Gel Methodology." International Journal of Advanced Research, Volume 4, Issue 1, 1329- 1337, (2016), ISSN 2320-5407. **http://www.journalijar.com**
- **Narendra G. Sarda**, Takanori Hayashi, Yuta Takeuchi, Kyosuke Harada, Kei-Ichiro Murai, Toshihiro Moriga, "A New Synthesis Route of Perovskite-related Sr_2TaO_3N Oxynitride via $Sr_2Ta_6O_{10.188}$" accepted in AIP Conference Proceedings; as a proceeding of CC symposium of ICCMSE (2016).

Abstract

In this research study, a number of oxynitrides for different applications such as; $(Ba_{1-(x+y)}Sr_xEu_y)_2Si_6O_{12}N_2$ phosphors for white LED, $LaTiO_2N$ co-nitridation with urea or thiourea and W^{6+} doped $La_{1.1}Ti_{1-x}W_x(O,N)_3$ (X = 0 - 0.05) for non-toxic pigment applications; were synthesized and their structural as well as optical properties have been investigated. Further, synthesis mechanism of Sr_2TaO_3N also briefly discussed. Oxynitrides have been synthesized by solid state reaction under diluted hydrogen flow or by thermal ammonolysis of oxide precursors. The structural study of $Ba_3Si_6O_{12}N_2$ and perovskite-types oxynitrides has been carried out by powder X-ray diffraction, and optical properties have been explored.

$(Ba_{1-(x+y)}Sr_xEu_y)_2Si_6O_{12}N_2$ oxynitride phosphors were successfully synthesized via solid-state reaction method. Substitution of barium by strontium caused a redshift of emission due to decrease in the lattice volume of the $(Ba_{1-(x+y)}Sr_xEu_y)_2Si_6O_{12}N_2$ phosphors. Shrinkage of the oxynitride lattice and enhancement of discrepancy between 5d levels in Eu^{2+} attributed redshifts, so that the emission maximum ranged from green (520 nm) to yellow-green (548 nm). The optical properties of silicon rich $(Ba_{1-(x+y)}Sr_xEu_y)_2Si_6O_{12}N_2$ phosphors, illustrate their potential for white LED applications.

$La_2Ti_2O_7$ precursors were prepared by the sol-gel method. Mixtures of oxide precursor ($La_2Ti_2O_7$) and urea or thiourea were prepared, and then subjected to thermal ammonolysis at 950℃ for 5 h. In particular, the addition of urea was highly beneficial for $LaTiO_2N$ synthesis, yielding pure phase products with higher nitrogen content than $LaTiO_2N$ powders prepared in

the absence of urea was observed. This result illustrates more quick method and development in synthesis of oxynitrides powders.

A series of new $La_{1.1}(Ti_{1-x},W_x)(O,N)_3$ perovskite with different compositions (X = 0.01,0.02,0.03,0.04,0.05) were synthesized by a thermal ammonolysis of oxide precursors prepared via a sol-gel method. The decent W^{6+} doping and excess of La relative to Ti in the oxynitride showed positive effect on red-shifting of the absorption edge of $LaTiO_2N$ perovskite oxynitride.

Formation process of the new layered perovskite Sr_2TaO_3N oxynitride having a K_2NiF_4-type structure from oxide precursor with $Sr_6Ta_2O_{10.188}$ – type phase was examined under an ammonia flow. Excess amount of strontium deviated from the stoichiometric composition of Sr/Ta=2 also seemed to promote the formation of Sr_2TaO_3N under the ammonia flow. The synthesized Sr_2TaO_3N after two cycles of 24h-nitridation of the oxide precursors showed brighter reddish-orange colour than $SrTaO_2N$. The usage of oxide precursor $Sr_6Ta_2O_{10.188}$ was beneficial in fast formation of Sr_2TaO_3N in 48h nitridation, compared with several 15h heating cycles in flowing ammonia which has been reported by Marchand et al in 1999.

List of Symbols and Abbreviation

Å - Angstrom (length unit)

A - Crystallographic Unit Cell Parameter

at.% - Atomic Percent

°C - Celsius Degrees (temperature unit)

cm - Centimeter (length unit)

EDS - Electron Dispersive Spectroscopy

Eg - Bandgap energy

eV - Electron-Volt (energy unit)

g - Gram (weight unit)

h - Hours (time unit)

IR - Infrared

K - Kelvin (temperature unit)

kJ/mol - kilojoule/mole

kV - Kilovolt (voltage unit)

LED - Light-emitting diode

mA - Milliampere (current unit)

min - Minute (time unit)

mg - Milligram

ml - Milliliter

mm/µm - Micrometer (length unit)

mm - Millimeter (length unit)

mol% - Mole Percent

MPa - Mega-Pascal (stress or pressure unit)

Nm - Nanometer (length unit)

N - Nitrogen

NH_3 - Ammonia

O - Oxygen

O/N - Oxygen/Nitrogen

Pa - Pascal

SDC - The Sample Delivery Controller

SE - Secondary Electrons

SEM - Scanning Electron Microscopy

t - Tolerance factor

TEM - Transmission Electron Microscopy

UV - Ultraviolet

vol% - Volume Percent

Wt% - weight Percent

YAG - Yttrium aluminium garnet

XPS - X-ray photoelectron spectroscopy

XRD - X-ray diffraction

Θ - theta

1 L min^{-1} - 1 Litre per minute

□ - Anion Vacancies

Chapter 1

Introduction

Oxynitrides have received great attention because of their fascinating chemical and physical properties in the past two decades. Oxides are usually colourless, but the substitution of oxygen by nitrogen with lower electronegativity, enhances the absorption edge in many materials. Thus, oxynitrides may show bright colours. Due to excellent chemical and thermal stability as well as bright colour without containing toxic elements; oxynitride materials are a good candidate for ecofriendly inorganic pigments [5,6], phosphor materials [1,2], visible-light-driven photocatalysis [3,4] and dielectric materials [7]. This research work is basically focused on bandgap tuning in oxynitride compound through proper adjustment of the O/N ratio for the application of non-toxic pigments and oxynitride phosphors for white LEDs**.** A pigment is a material that changes the colour of reflected or transmitted light as the result of wavelength-selective absorption. Inorganic pigments have been used by mankind since ancient times, and still widely used in numerous industries, especially in those of paints, plastics and ceramics [5]. However, many of the inorganic pigments contain toxic metal ions like cadmium, lead, chromium and cobalt. The use of these metal ions is becoming strictly controlled and/or banned by many developed countries to protect human health and the environment. Red pigments based on cadmium sulfoselenide is particularly cause of concern due to cadmium itself is toxic and can enter the environment through waste-disposal sites and incineration plants. Recently, a number of researchers are developing a new ecofriendly inorganic pigment that exhibits excellent properties such as, thermal and chemical stability, opacity, tinting strength, dispersability, chromaticity which are equivalent to cadmium or toxic metal based pigments [5,8]. In recent years, perovskite-based inorganic pigments have been investigated. In 2000, Jansen and Letschert suggested to use $Ca_{1-x}La_xTaO_{2-x}N_{1+x}$

compounds to substitute reddish pigments based on problematic toxic heavy metal cadmium. They demonstrated that any colour in the range from light yellow through orange to deep red can be tailored by proper adjustment of the O/N ratio in the solid solution. Perez-Estebanez et al., Maeda et al. also showed that bandgap can be continuously tuned by varying the doping level of nitrogen. R.Aguiar et al. reported on perovskite-related oxynitrides of the ABO_2N type (A= Ca^{2+}, Sr^{2+}, Ba^{2+} and B = Ta^{5+}, Nb^{5+}) show yellow, orange, ochre and black colours [8,11]. Perovskite-type $LaTiO_2N$ oxynitrides are promising materials for applications such as non-toxic pigments, visible-light-driven photocatalysts and so on [9-10]. Previously, our research group has successfully demonstrated on a control of optical properties for $LaTiO_2N$ through adjustments of the cation and anions non-stoichiometry. The anion non-stoichiometry in the oxynitrides affected on the optical bandgap. The increase of O/N ratio in the oxynitrides $LaTiO_{2+x}N_{1-x}$ resulted in the enhancement of the optical bandgap to change the body colour from orange, yellow, green, grayish pale blue to white [25,36-39]. To obtain real red colour we think that; if the nitrogen content in the oxynitride increases, the bandgap will get narrower enough to show red colour.

There are three major factors which can affect on width of optical bandgap and vary the colour in oxynitride they are as follows –

1. Enrichment of nitrogen ratio in anions
2. Control the influence of B-anion-B bond angle / Increase in covalency decrease in bandgap
3. Influence of electronegativity of the B cation

Considering above factors it is possible to improve optical properties of oxynitrides for the application of white LED and ecofriendly red pigments.

In the present work we have demonstrated that;

- Ba^{2+} substitution with Sr^{2+} decreased the lattice volume of the $(Ba_{1-(x+y)}Sr_xEu_y)_2Si_6O_{12}N_2$ phosphors and was responsible for the redshift in the emission peak. The smaller cation has the larger electronegativity. That means the difference in averaged electronegativity between cation and anion becomes small when the smaller cation is selected. This strategy is applicable to the above concept number three.
- As an example for the first concept to vary the O/N ration in the oxynitride compound we have studied the enrichment of the nitrogen content in $LaTi(O_{1-x}N_y)_y$ via addition of urea and thiourea. Use of urea yielding pure phase $LaTiO_2N$ with higher nitrogen content attributes redshift in optical band as well as it becomes rapid method for the synthesis of oxynitride powders.
- The substitution of cations outcome in intense change in colour of the oxynitride perovskite which attributes fine-tune in the colour by doping with small amount of different cations. Appropriate doping of tungsten with high valence state and excess of lanthanum (La) compared to titanium (Ti) in the $La_{1.1}(Ti_{1-x},W_x)(O,N)_3$ oxynitride allow redshift of the absorption edge. In this case observed in colour change is due to different electronegativities of B cations.
- New synthesis route of Sr_2TaO_3N showing redder colour than $SrTaO_2N$. The band gap can be decreased by increasing or change in the crystallographic symmetry. $SrTaO_2N$ belongs to a cubic (3 dimensional) perovskite type, whereas Sr_2TaO_3N belongs to a tetragonal (2 dimensional) layered perovskite type. This suggests there should be some not ignorable distortion in three-dimensionally linked TaO_4N_2 octahedra in $SrTaO_2N$. Such distortion will be considerably more relaxed and covalent in two-dimensionally linked $TaO_2(O,N)_4$ octahedra. These relationships open the possibility to alter the optical band gap of oxynitrides.

1.1 Oxynitride Materials

Oxynitrides are Inorganic compound having general formula $M_x(O,N)_y$, where M is mainly of Transition metals and Ionic-covalent. Nitrogen and Oxygen have multiple similarities in chemical, structural and electronic characteristics such as electronegativity, polarizabilities, ionic radii and coordination number (Table 1.1). Hence they are substitute for each other [12]. Nitrides are thermodynamically less stable than oxide due to inimical electron affinity and high bond energy of the diatomic molecule N≡N. Thus, the preparation of nitrides is more difficult compared to the oxides. The synthesis of nitrides and oxynitrides are usually very difficult, but transition metal oxynitrides have been investigated intensively, due to the new synthetic methodology which has been developed in the last several years. Solid-State Reactions, Soft-chemistry method, Ammonolysis, Carbiothermal reduction, high-pressure synthesis for bulk or powder materials and magnetron sputtering, pulse laser deposition, plasma enhanced chemical vapor deposition for thin films these techniques were used to gain large quantity of Oxynitrides.

Table 1.1 Properties of Nitrogen and Oxygen

	Nitrogen	Oxygen
Anionic Charge (z)	-3	-2
Atomic polarizability ($Å^3$)	1.10	0.80
Bond energy A-A (kJ/mol)	941	498
Electronegativity	3.0	3.4
Electron affinity ($A \rightarrow A^{z-}$, kJ/mol)	1736	601
Ionic radii (Å) (for CN = IV)	1.46	1.38
Coordination number (CN)	II-VIII	II-VIII

Due to their substantial structural diversity, oxynitride materials exhibit a wide range of interesting physical and chemical properties like; thermal, mechanical, magnetic, electrical, superconductivity and optical properties (refractive index, reflectance, absorbance, bandgap, photoluminescence and transmittance). These properties can be explored for various industrial applications such as antireflection coatings, solar absorbers, heat mirrors, coloured pigments, visible-light-driven photocatalysts, spectral conversion phosphors and transparent windows and armors. In this work we have focused on perovskite-type structure related oxynitrides.

1.2 Structure of $Ba_3Si_6O_{12}N_2$

The structure of $Ba_3Si_6O_{12}N_2$ comprises a rigid network of corner-shared SiO_3N tetrahedra arranged in layers (Fig. 1.2). Ba^{2+} ions are located in the voids formed by the SiO_3N tetrahedral layers, and occupy two different crystallographic sites; one is a trigonal anti-prism site (distorted octahedron with six oxygen atoms) and the other is trigonal anti-prism site with six-oxygen and further capped with a nitrogen atom (7-fold coordination in total).

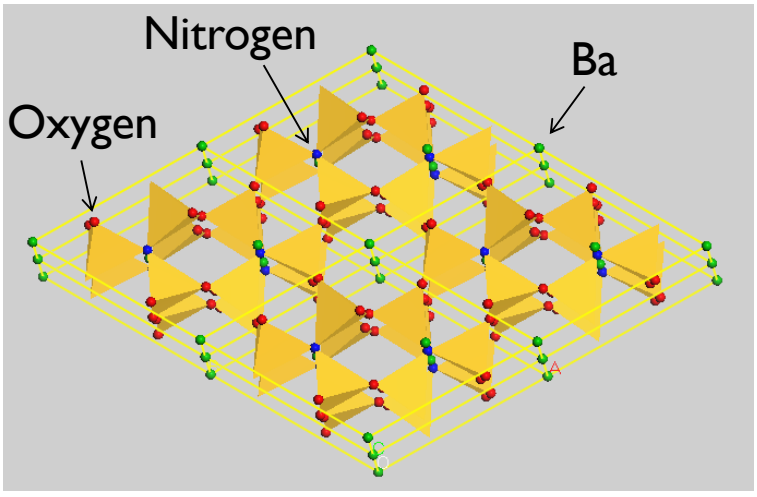

Fig.1.2 Structure of $Ba_3Si_6O_{12}N_2$ viewed along the c-axis. The structure is composed of layers of corner-sharing SiO_3N tetrahedra with Ba^{2+} ions occupying sites between the SiO_3N layers. The structure can tolerate high Ba^{2+} deficiency and remains stable even at Si/Ba ratios from 2 to 6 [47]

The network of corner-shared SiO_3N tetrahedra in the $Ba_3Si_6O_{12}N_2$ structure is very stable, and high Ba^{2+} deficiencies can be tolerated. $Ba_{3-x}Si_6O_{12}N_2$-type compounds, with Si/Ba ratios as high as 6, have been reported with little or no change in the crystal structure.

1.3 Perovskite Structure

The perovskite name was given by Russian mineralogist L.A. Perovski; he first discovered atomic arrangement structure in $CaTiO_3$. The perovskite structures have general formula ABO_3, where A indicates a conventionally large cation compared to B with low charge, for e.g. alkali or alkaline earth metal, rare earth metal, while B cations are transition metals. O is usually anion as an oxide or fluoride which bonds with both the cations [13].

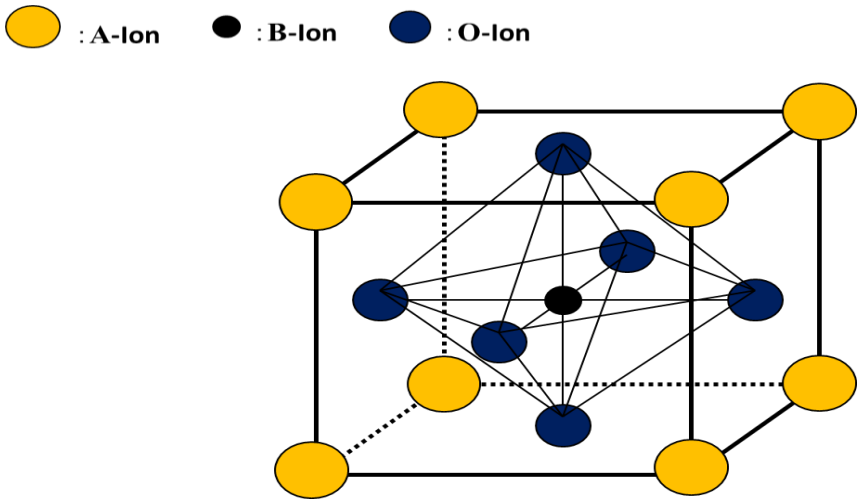

Figure 1.3.1 Cubic Perovskite structure [13]

In the ideal form the crystal structure of cubic ABO_3 perovskite can be described as consisting of corner sharing BO_6 octahedra with the A cation occupying the 12-fold coordination site formed in the middle of the cube of eight such octahedra. Briefly, the ideal perovskite structures can be simplified by $SrTiO_3$ as shown in Fig. 1.3.2. Sr is in the center

(coordinates 1/2, 1/2, 1/2), surrounded by eight smaller Ti (0,0,0) at the corners and twelve O anions at the midpoints of the cell ages (1/2,0,0;0,1/2,0;0,0,1/2).

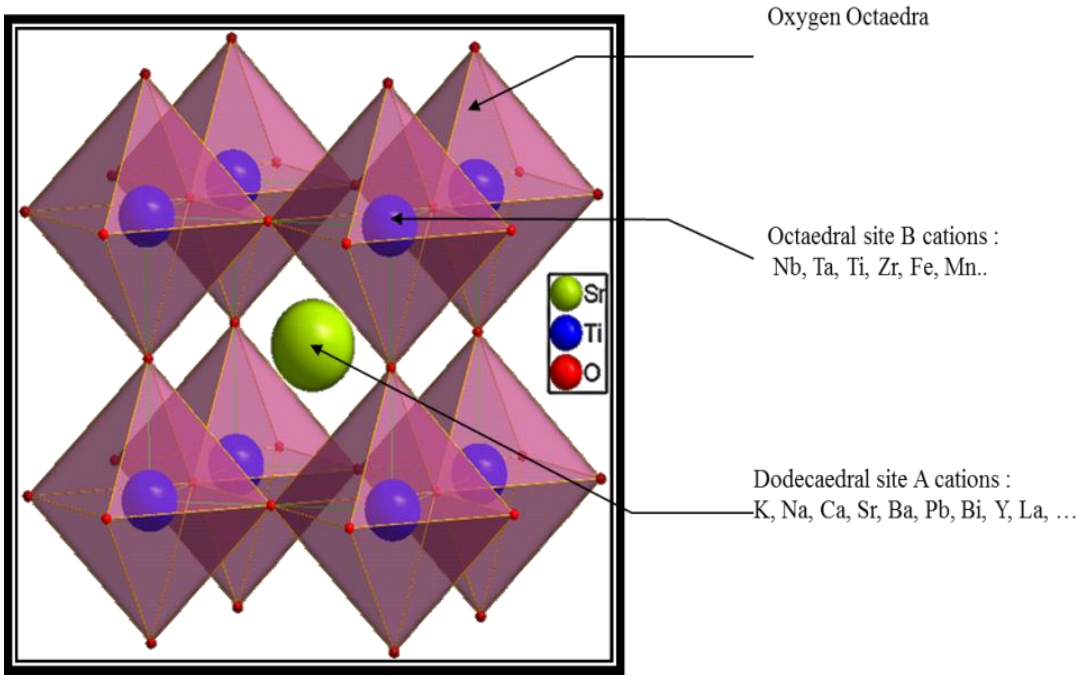

Figure 1.3.2 Crystal structure and atomic arrangement in $SrTiO_3$ [14]

Each Ti cation is coordinated to six O anion. The undistorted cubic perovskite has space group of $Pm\bar{3}m$. The octahedral coordination by oxygen of one corner Ti is shown, $Ti-O = a/2 = 1.953$ Å. Sr in the cube center is equidistant from all twelve oxygen's at edge center positions. The $Sr-O$ distance equals half the diagonal of any cell face, i.e. $a/\sqrt{2}$ or 2.76 Å. Each O has two Ti as it's nearest cationic neighbors, at 1.953 Å, and four Sr, coplanar with O at 2.76 Å.

In 1926 Goldschmidt were studied about structure distortions in perovskite and he defined tolerance factor [15]. Tolerance factor (t) is used to describe divergence of the real crystal structures from the ideal structure.

$$t = \frac{r_A + r_X}{\sqrt{2}(r_B + r_X)}$$

In order to have contact between cations and X anions rA + rX should equal to $\sqrt{2}(r_B+r_X)$, Where; $r_A$is the radius of A cation, r_B is the radius of B cation and r_x is the radius of the anion (usually oxygen). In general, when the value of t is close to 1, the perovskite phase will be formed. If t value is lower than 1, the perovskite phase will not form [16]. $SrTiO_3$ and $FeTiO_3$ are the best examples to explain this. t value of $SrTiO_3$ and $FeTiO_3$ is 1 and 0.863 respectively which adopts $FeTiO_3$ has ilmenite structure. Lower values of t lead to lowering of the symmetry of the perovskite structure. A Perovskite material shows many interesting and intriguing properties they shows high flexibility and a wide range of chemical and physical properties such as interesting optical properties which exhibits applications in photocatalysts for solar energy conversion, non-toxic pigments, white LED and so on.

1.4 Layered perovskite-type structure

Generally, K_2NiF_4 type structure consists of layers of corner-sharing NiF_6 octahedra sharing 4 vertices. These layers are separated by K^+ ions in nine fold coordination to fluorine instated of twelve in the cubic ABO_3 perovskite structure. The Sr_2TaO_3N oxynitride shown in Fig 1.4 with the tetragonal K_2NiF_4-type structure having space group I4/mmm can be described as two dimensional perovskite. The structure is body centered with the NiF_6 octahedron at the unit cell centre displaced by (1/2, 1/2, 1/2) from that at the cell origin.

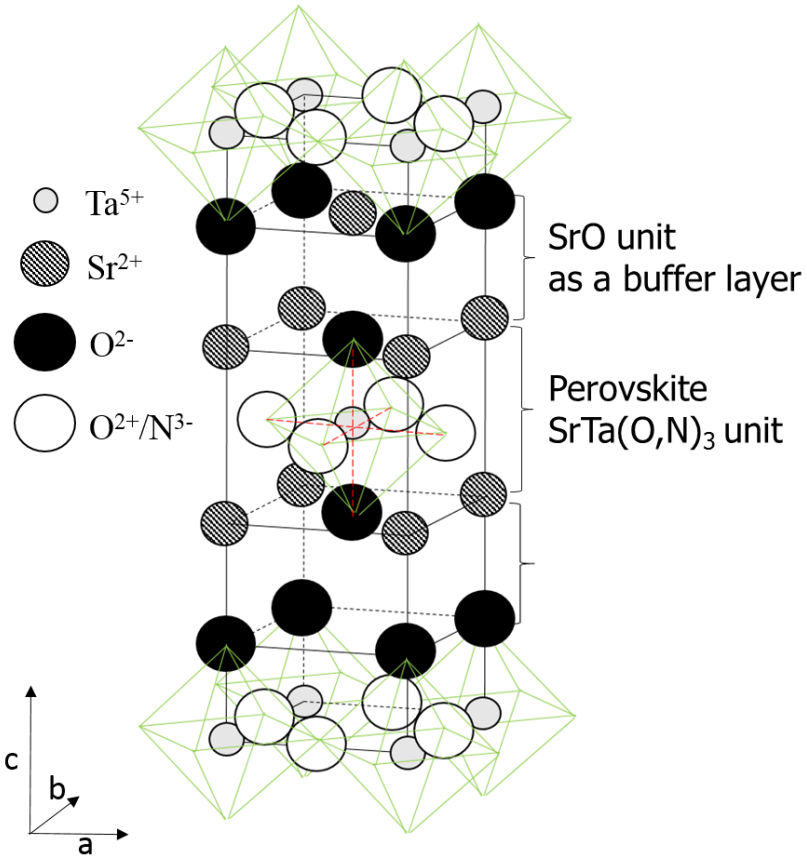

Figure 1.4 Crystal structure and atomic arrangement in Sr_2TaO_3N [56]

This structure is wieldy adopted by ternary oxides of the stoichiometry A_2BX_4 where one cation, A, is much larger than the other, B [17]. This contrasts with the spinel structure which has the same stoichiometry but occurs where A and B have similar ionic radii. Previously Marchad et.al. has studied the crystal structure determination of Sr_2TaO_3N in that they showed the structural arrangement consist of layers of corner-sharing $TaO_2(O,N)_4$ octahedra, apical sites being occupied primarily by oxygen and median sites by oxygen and nitrogen. The strontium atoms lie between the layers [56].

1.5 Optical properties of perovskite-type oxynitride

Physical properties of perovskite-oxide could be changed by cationic substitution. Owing to its flexibility, the perovskite structure can accept a large number of cationic substitutions, which allows fine tuning of the electronic structure, charge carrier concentration and accordingly electronic and optical properties of the materials. Different electronegativity (Table 1.1) shows that bonding in oxynitride should be more covalent compare to oxides. Therefore, smaller bandgap is expected. General, bandgap values for oxynitride have been already reported which is in between 1.8-3.3eV. Optical bandgaps of d^0- perovskite-type oxynitrides overlap with the solar spectrum, which makes these materials interesting for applications in visible-light-driven photocatalysts and ecofriendly pigments. In oxynitrides $AB(O,N)_3$, (A= La^{3+}, Ba^{2+}, B=Ti^{4+},Nb^{5+},Ta^{5+}) bandgap decreases with increasing A-cationic radius. For example $LaTiO_2N$ bandgap is 2.0-2.1eV and $BaNbO_2N$ bandgap value is 1.8eV. This is due to the relationship between the electronegativity of the B-site cation and optical bandgap for d^0- perovskite-type oxide.

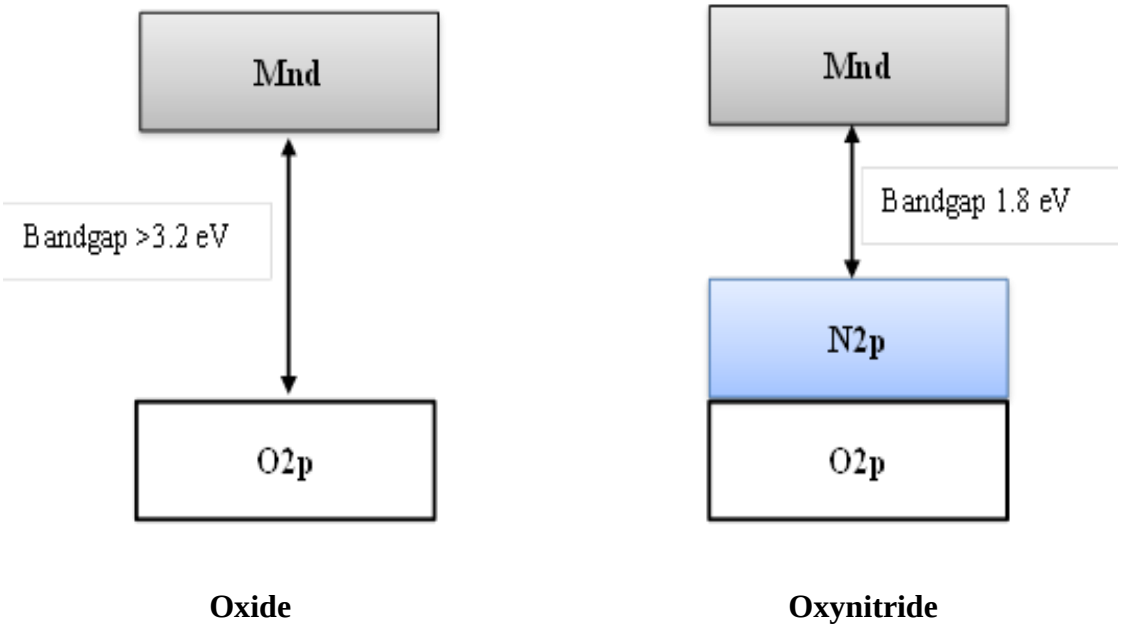

Fig.1.5 Band structure of oxide and oxynitride [29]

In such perovskite-type oxides and oxynitrides, the top of the valence band is dominated by orbitals of the constituting anion and the bottom of the conduction band is predominantly formed by the d orbitals of the transition metals. The incorporation of N^{3-} in the perovskite oxides results in a considerable bandgap reduction since the 2p orbital of nitrogen has a higher energy than that of 2p orbitals of oxygen. Consequently, the optical absorption edge shifts toward higher wavelength in the visible light region.

The width of the bandgap is determined by the extent of overlap of the valence orbitals and by the difference between the electronegativities of the cations and anions involved. It is also reported that distortion of bond angle B-(O,N)-B from 180^0 may reduce covalent character of the oxynitride, resulting in a wider bandgap. In trying to rationally develop new inorganic pigments, we have focused on widening of the bandgap by increasing the difference of electronegativities between the respective cationic and anionic elements and vice-versa. Whereas the electronegativities of the metals only vary in small steps, the substitution of one non-metal by another usually produces large shifts in electronegativity difference. In order to achieve fine-tuning of the bandgap, we have focused on materials containing two different non-metals.

1.6 Synthesis of perovskite-type Oxynitride

Thermal ammonolysis is used to synthesize oxynitride from oxide precursor. The best and simplest method for oxynitride synthesis is thermal ammonolysis, in which nitrogen source either N_2 or NH_3 are used as nitriding agent.

General reaction is given below

$$ABO_3 + NH_3 \longrightarrow AB(O,N)_3 + H_2O$$

$$2SrCO_{3(s)} + Ta_2O_{5(s)} + 2NH_{3\,(g)} \longrightarrow 2SrTaO_2N_{(s)} + 2CO_{2\,(g)} + 3H_2O_{\,(g)}$$

Recently; ammonia is a widely used as a nitriding agent because N_2 is insufficient as a nitridizing agent due to the very high thermodynamic stability which is arises from N≡N bonds (E_{diss} = 950kJ/mol). Hence, high activation energy is required for the direct reaction between N_2 and oxide. It was also proved experimentally that the H_2/N_2 mixtures do not promote effective nitridation either. Oxide mixtures and oxide carbonate mixture are among the most often used precursor for the perovskite-type oxynitrides synthesis.

Thermal ammonolysis is carried out temperature in a range of 650℃-1050℃ and atmospheric pressure. The reaction mechanism is still not well studied. However it has been suggested that the ammonia dissociates at the surface, with the formation of NH_2, NH, atomic N species and hydrogen. Hydrogen acts as a reducing agent that reacts with the lattice oxygen forming water, where the formation of H_2O provides the thermodynamic driving force in the reaction and creating the oxygen vacancies, which act as centers for the surface incorporation of N atom. Some thermodynamical and kinetic parameters (ammonia flow rate, pressure, temperature, and reaction time) play important role in ammonolysis process. All reaction is controlled by these parameters, which have an influence on the reactions thermodynamics.

1.7 Application of oxynitride as white LED

Oxynitride phosphors have recently attracted great attention for use in white LEDs due to their high quantum efficiency, low thermal quenching behavior, and high chemical and physical stability compared with conventional oxide phosphors [18-22]. The white LED is highly one of the most promising eco-friendly light sources, with much less CO_2 gas burnout to save energy consumption than conventional light sources such as incandescent lamp [60]. Generally, White-LEDs are fabricated by combining LED chips with phosphors. The efficiency of white-LEDs strongly depends on the luminescence properties and thermal stability of phosphor. Phosphors are key material for white-LEDs. Many different nitride and oxynitride phosphor materials have been developed targeting white LED applications, including $Sr_2Si_5N_8$, $SrSi_2O_2N_2$ and alpha- and beta-SIALONs. Particularly promising in this regard is the green oxynitride phosphor, $Ba_3Si_6O_{12}N_2:Eu^{2+}$ reported by the Mitsubishi Chemicals Group in 2009 [23]. There are three general methods used for synthesizing white LEDs [18]. The simplest and most practical approach is the coating of a blue-emitting InGaN LED with a blue-absorbing, yellow-emitting phosphor such as $YAG:Ce^{3+}$. However, the emission intensity of YAG-based phosphors in the red region of the visible spectrum is relatively weak, resulting in a poor rendering index and a pale white light. Further, the emission intensity of $YAG:Ce^{3+}$ phosphors drops sharply as the temperature increases, which is also undesirable for white LED applications.

This motivates the search for alternative yellow-emitting phosphors that have superior durability and thermal tolerance. In chapter 3, it has been briefly discussed on the synthesis, structural and optical characterization of silicon rich $(Ba_{1-(x+y)}Sr_xEu_y)_2Si_6O_{12}N_2$ phosphors, with strontium content (x)=0-0.6 and europium content (y) = 0.05-0.25. The optical properties of these phosphors are also compared with a commercial $YAG:Ce^{3+}$ phosphor to illustrate their potential for white LED applications

1.8 Application of oxynitride in non-toxic pigments

Perovskite-type oxynitrides are promising materials showing the potential application in many fields such as, harmless inorganic pigments, Phosphors for LED, Visible-light-driven photocatalysis, gas sensor and dielectric materials. Different kinds of oxynitrides have been synthesized in the past decades and their applications are also developing in various fields as it is already mentioned in sections 1.1 and 1.3.

Inorganic pigments have been used in art and wall decorations since prehistoric times, and today still find widespread use in coating technologies due to their attractive optical properties and excellent weather resistance. Many inorganic pigments commonly used in paints (e.g. CdS, CdSe and $PbCrO_4$) contain heavy metals that pose a potential environmental hazard. Accordingly, there are strong economic and environmental drivers to develop alternative, low cost and non-toxic inorganic pigments for the paint and printing applications. [35-37]

Especially, inorganic non-toxic red pigments are commercially high in demand due to their wide applicability. However, Fe_2O_3 has been widely used as an ecofriendly inorganic red pigment, but due to the unsatisfactory colour performance there is need to develop alternative pigment. A number of interesting approaches have been done and continued to elaborate alternative, low cost, non-toxic and satisfactory colour performance for the paint and desk-jet printing application. Jansen et al. have reported that the colours of the solid solutions $Ca_{1-x}La_xTaO_{2-x}N_{1+x}$ of the perovskite-type pigments could be tuned from yellow through orange to deep red by simple composition adjustment [31]. They demonstrated that any colour in the range from light yellow to deep red can be tailored by proper adjustment of O/N ratio in the solid solution.

Fig. 1.8.1 The colour change in the system with different N content [64]

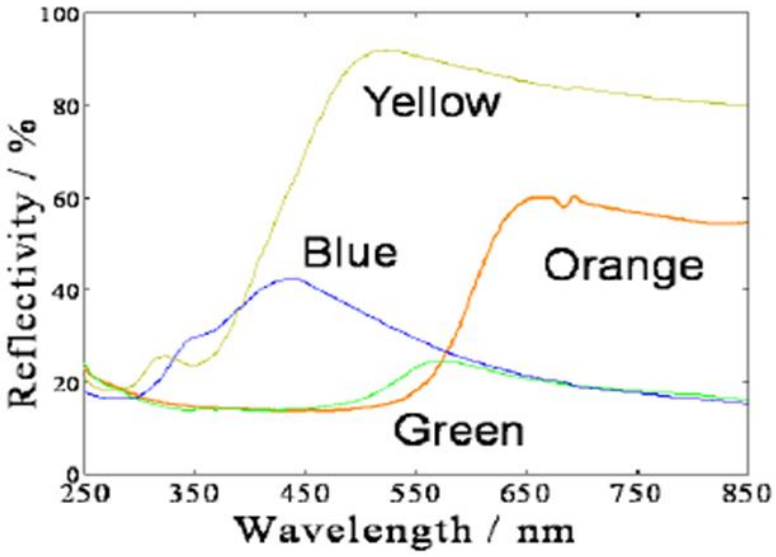

Fig. 1.8.2 Diffuse reflectance spectra of $LaTiO_{2+x}N_{1-x}$ Oxynitride powders [64]

In our previous research studies we have shown that; the colour of perovskite-type $LaTiO_{2+x}N_{1-x}$ can be tuned from reddish orange to very pale blue or light gray by simple composition adjustment in the anions. The perovskite-type material exhibit appropriate brightness good thermal as well as chemical stability. The colour change in the system $LaTiO_{2+x}N_{1-x}$ with variation of nitrogen content is shown in Fig. 1.8.1 and diffusion reflectance spectra are shown in Fig. 1.8.2.

Chapter 2

Experimental Methods and Characterization

- **Synthesis of Oxide precursor**

2.1 Soft Chemistry Synthesis

It is also called as pechini method. This method is used to prepare a homogeneous solution containing all the cationic ingredients. The solution is gradually dried and, depending on the species present, it may transform to a viscous sol containing particles of colloidal dimensions and finally to a transparent, homogeneous, amorphous solid known as a gel.

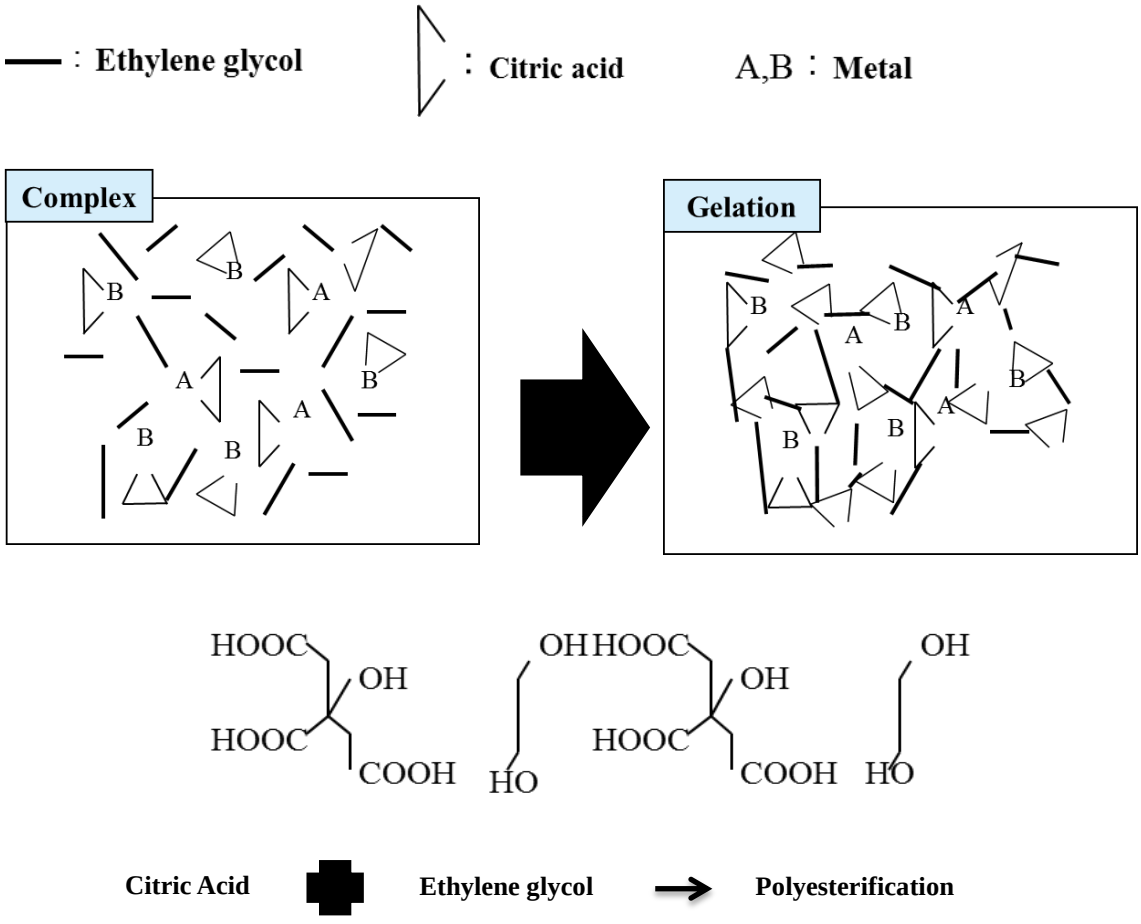

Figure 2.1.1 Scheme demonstrating the stabilization of the metallic cations in solution by citric acid [66]

The gel is then fired at high temperatures to remove various volatile components trapped in the pores of the gel or chemically-bonded organic-side groups and crystallize the final product. The reduction in the particle size by grinding the reaction mixture, even mechanically, can only achieve a limiting level of grain diameter, at best about 0.1 μm. However, chemical methods can be used to effectively reduce particle size still future and enhance reaction rates at a particular temperature.

The reagents for sol-gel syntheses are usually metal-organic compounds, especially alkoides such as titanium isopropoxide $Ti(O^{i}Pr)_4$ as a source of TiO_2, tetraethylorthosilicate (TEOS), $Si(OCH_2CH_3)_4$ as a source of SiO_2 and aluminum butoxide, $Al(OBu)_3$ as a source of Al_2O_3. The soft chemistry methods usually start from dissolving stoichiometric quantities of desired cations such as, nitrides, chlorides or alcoholates in an aqueous solution. Citric acid is used to promote the chelation of the cations. The citric acid stabilizes the dissolved cations in solutions avoiding their precipitation for example as hydroxide. The reagents which are usually the covalent liquids mixed in the appropriate ratios, often with an alcohol to promote miscibility of the alkoxide and H_2O. In chapter 4 and 5 this method is used to obtain $LaTiO_7$ oxide. Figure 2.1.2 illustrates the flow chart of synthesis procedures of metal-oxide precursor by the soft-chemistry method. Experimental details are briefly described in following chapters 4 and 5 respectively.

Flow chart diagram

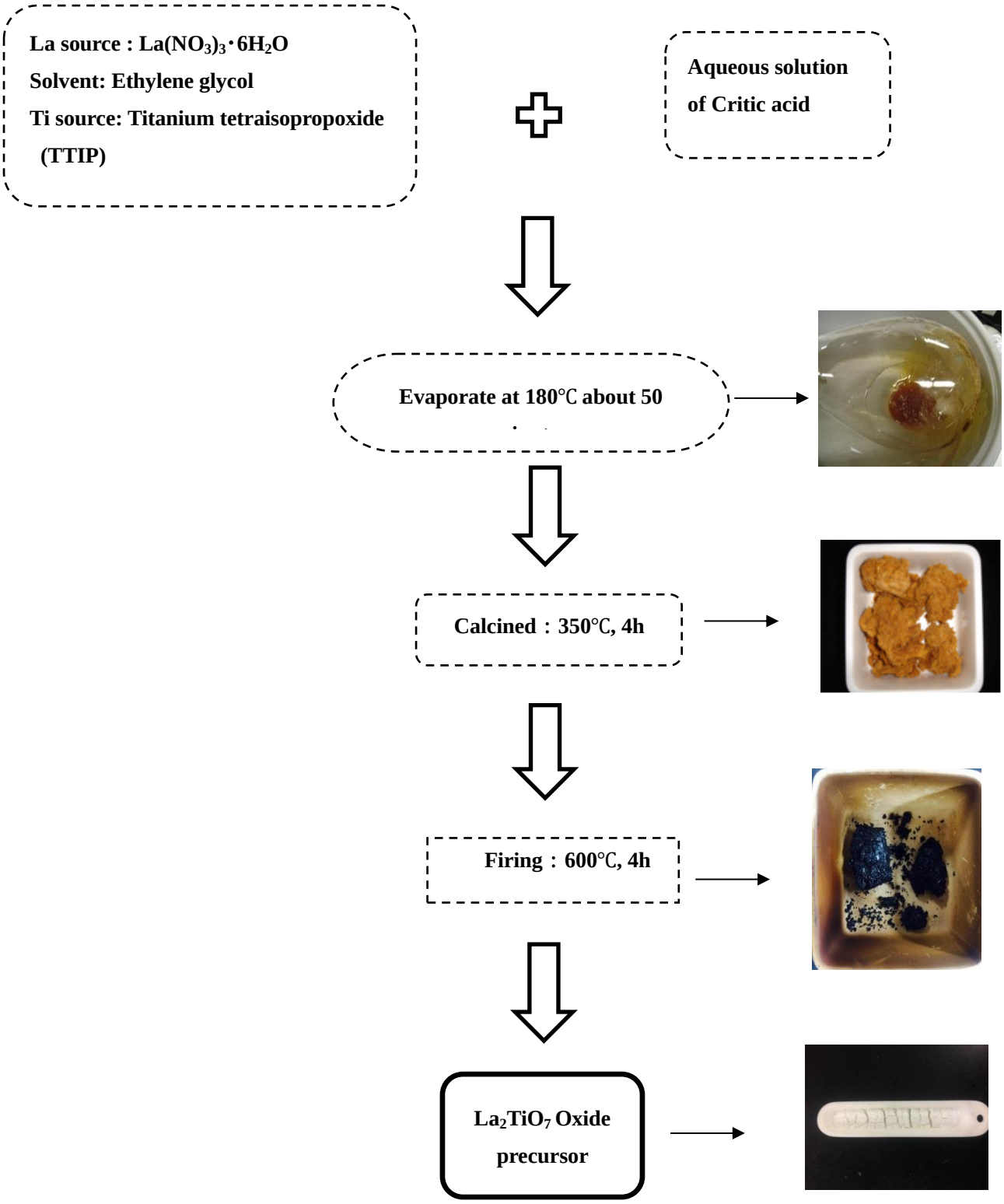

Figure 2.1.2 Synthesis procedures of metal-oxide precursor by the soft-chemistry method

2.2 Solid State reaction

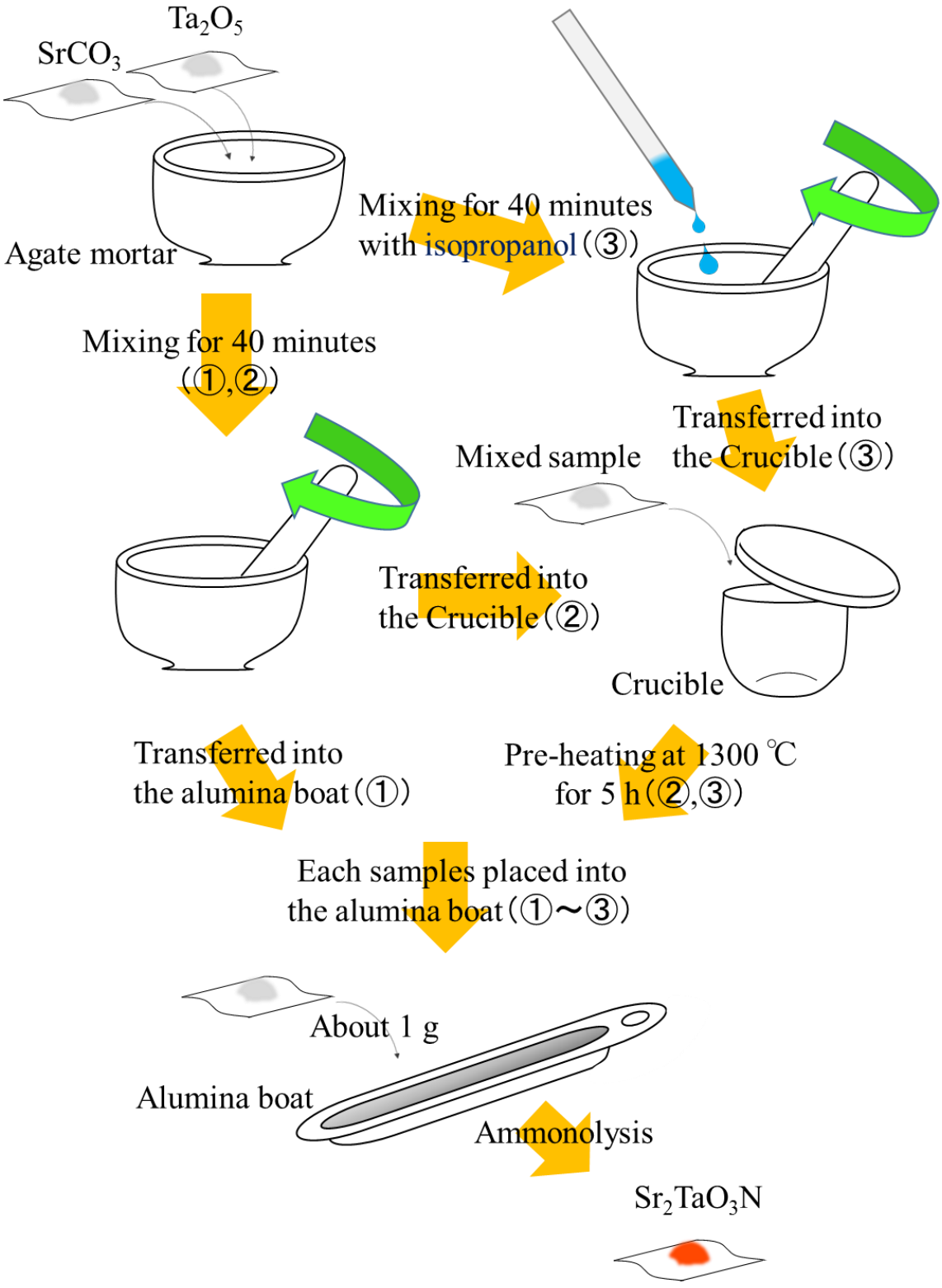

Figure 2.2.1 Synthesis of Sr_2TaO_3N by solid state reaction method

The Solid state reaction route is one of the oldest, simplest and most widely used synthesis methods for the preparation of polycrystalline solids. The oxides are well ground using agate mortar and pestle or ball mills. Solid do not react together at room temperature over normal time scales so there is need to treat them at high temperatures, for example 1000^{o}C to 1500 ^{o}C in order for the reaction to occur at an appropriate rate. The method is not much sophisticated also it is known as Shake n bake or beat n heat. Highly pure metal oxide were mixed together in stoichiometric ratios and preheated at appropriate temperature and time to remove moisture or carbonate. Finally ground using an agate pestle and mortar sometimes alcohol is used to improve particle contact during the reactions and homogeneity. The synthesis process is repeated several times to improve the purity of the compound.

The carbonates $BaCO_3$ (Kanto Chemicals, 99.9%), $SrCO_3$ (Kanto Chemicals, 96%), Si_3N_4 (Aldrich, 98.5%), SiO_2 (Aldrich, 99.8%), Eu_2O_3 (Kanto Chemicals, 99.5%) were used to prepare $Ba_3Si_6O_{12}N_2$ in chapter 3. In chapter 6 $SrCO_3$ (Kanto Chemicals, 96%) and Ta_2O_5 (Wako chemicals, 99.5%) were used to prepare Sr_2TaO_3N. Fig 2.2.1 shows the schematic diagram for synthesis of Sr_2TaO_3N and Fig. 2.2.2 shows general synthesis method of oxide precursor.

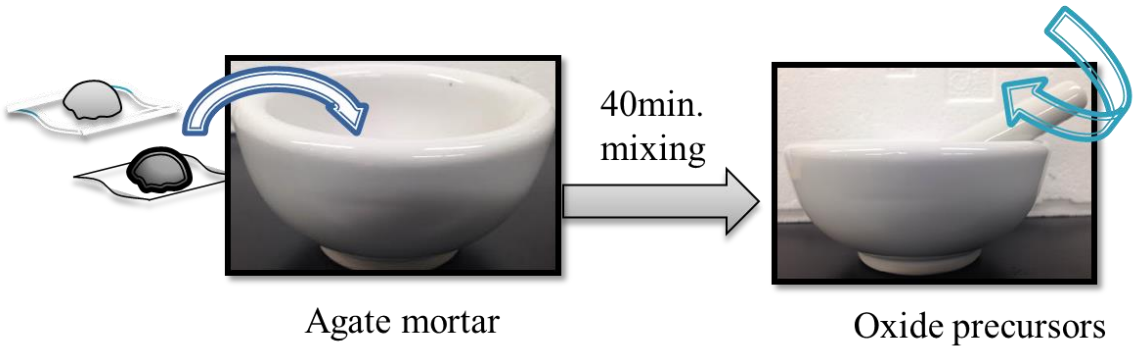

Figure 2.2.2 General synthesis of oxide precursor by solid state reaction method

2.3 Thermal Ammonolysis

All the oxynitride samples were prepared by a Thermal ammonolysis reaction. Experimental set up are shown in Fig.2.3.1.

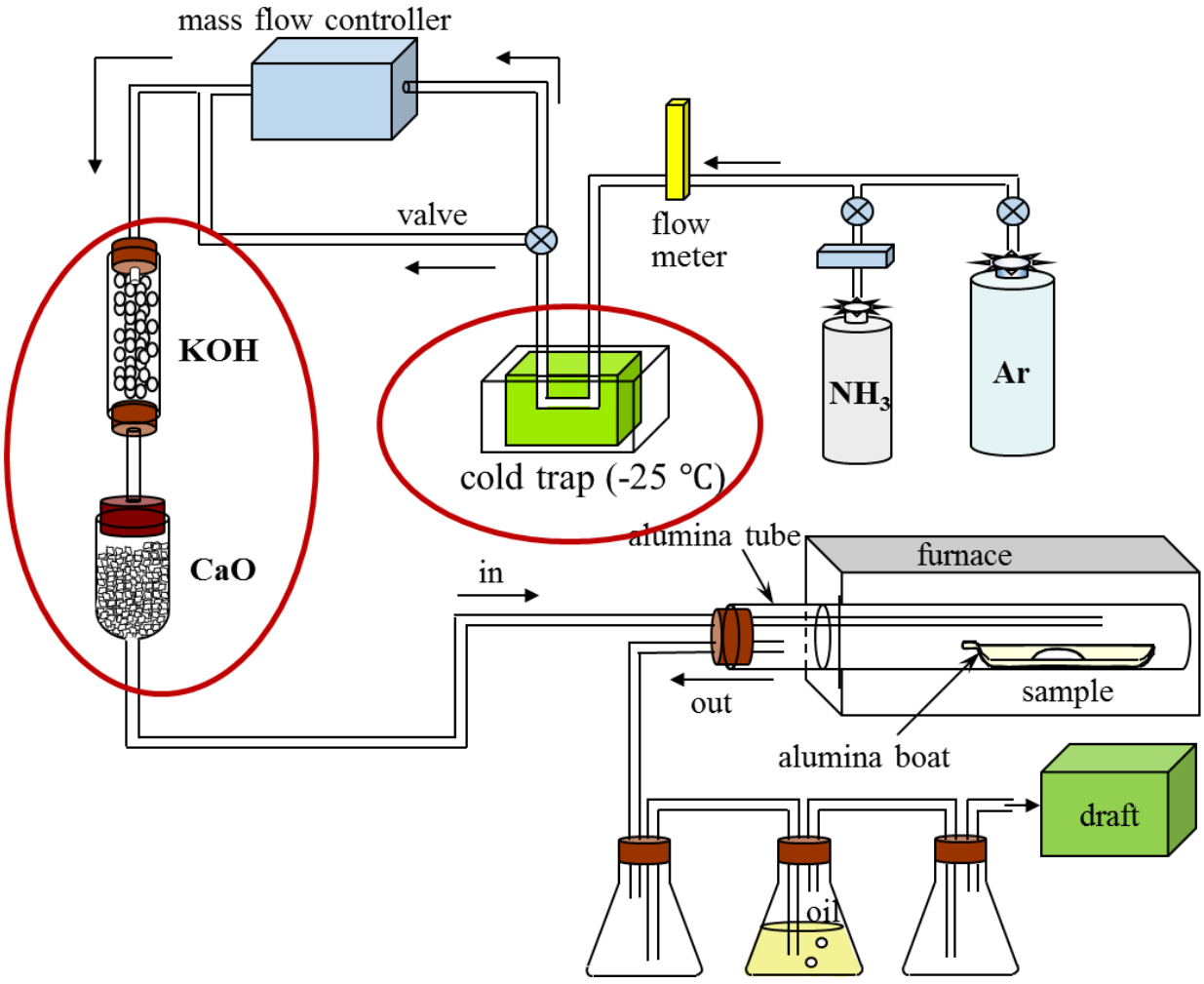

Figure 2.3.1 Thermal ammonolysis experimental set up

The powdered precursor was set in an alumina boat and placed in the alumina tube of horizontal silicon it tube furnace. Ammonia gas was passes over the sample for 30 minutes to expel air and temperature was raised to the nitriding temperature. Potassium hydroxide (KOH) and calcium oxide (CaO) were used as a drying agent. The flow volume of the NH_3 gas was $1dm^3$/min. The duration of nitridation was 5 hours. Condition of the nitridation varies with the obtaining final product. After the nitridation completed temperature set to 0℃ and

NH_3 gas was switched to argon gas when the temperature come down to 600℃. Both the argon and ammonia gases were used dried by passing through a soda lime cylinder and coiled coolant trap cooled at -25℃. After the nitridation was completed, the product was cooled down to the room temperature in the furnace.

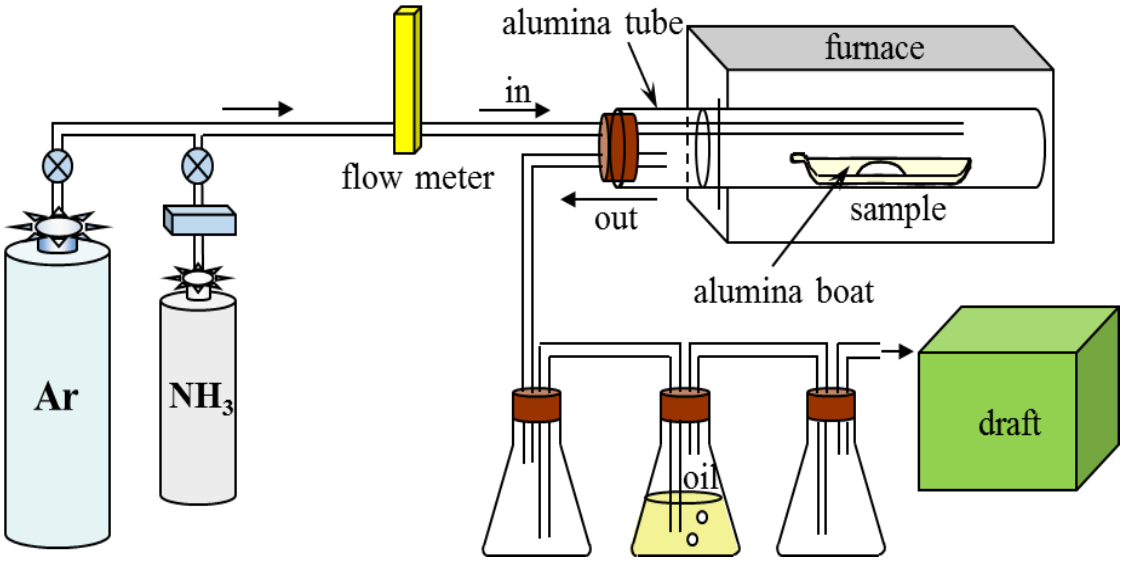

Fig.2.3.2 Schematic drawing of new nitriding set-up

In the new set-up cold-trap, KOH and CaO these three devices were removed and ammonia gas flow was directly attached into the tube furnace. Ammonia gas flowing path were reduced from 5 meter to 2 meter.

The general aims of the new set-up:

1. This change was done for the direct synthesis of the Sr_2TaO_3N to achieve the desired oxynitride in short time.
2. To obtain oxynitride powders with a uniform anionic composition.

2.4 Characterizations

2.4.1 XRD

X-ray diffraction (XRD) is a versatile, non-destructive analytical method to analyze material properties like phase composition, structure, texture and many more power samples, solid samples or even liquid samples. Identification of phases is achieved by comparing the X-ray diffraction pattern obtained from an unknown sample with pattern of a reference data base. This process is very similar to the identification of finger prints in crime scene investigations.

X- Ray powder diffraction is used in a wide variety of research and process control environments. For example:

1. Characterization of new materials at universities and research centers.
2. Process control in several industries like building materials, chemicals, pharmaceuticals, for instance phase composition and content.
3. Determination of polymorphism, API (Active Pharmaceutical Ingredient) concentration determination, API stability studies in the pharmaceutical industries.
4. Phase Identification of minerals in geological samples.
5. Optimization of fabrication parameters for wear-resistant ceramics and biomaterials.
6. Determination of the crystallinity of a phase.
7. Determination of amorphous phase contents in mixtures.

In our research work we used only powder sample for the XRD analysis. Powder is placed on the sample holder and other plate is used for pressing the sample. Other plate is rubbed on the sample so that sample holder can hold the sample for the analysis. This is one of the simplest methods of sample preparation for XRD measurements. The optimal particle size of powder diffraction samples is in the range of 1 to 5μm.

If the powder is too coarse this results in single points on the debye-Scherrer ring. Therefore point or liner detectors do not recognize all reflections which leads to incorrect intensity

ratios. If crystallites are much smaller than 1μm, reflections are broadened.

So main thing while preparing sample for XRD measurement is-

Do not treat the original sample more than necessary.

We can formulate a general rule for d-spacing in cubic crystals:

$$d = \frac{a}{\sqrt{h^2 + k^2 + l^2}} \quad [67]$$

Where a is the lattice constant and h,k and l are the indices of the planes.

When x-rays encounter a crystalline material, they are diffracted by the planes of the atoms within the crystal. The diffraction angle, denoted by the Greek letter theta (θ), depends on the wavelength, denoted by the Greek letter lambda(λ), of the x-rays and the distance d between the planes:

$$n\lambda\ (n=1) = 2d\sin\theta \quad \textit{Bragg's law} \quad [67]$$

The phase composition of the products was examined by powder X-ray diffractometry (Rigaku RINT-2500VHF+) and (Rigaku SmartLab X-ray diffractometer). XRD data was recorded over the 2θ range 10-90^{o} using a monochromatized CuKα source (λ = 1.5406 Å) operated at 40 kV and 150 mA. Phase identification was made with reference to the JCPDS database. XRD is the most applied analysis method in solid-state chemistry, because it identifies the crystalline structure, also quantitatively. Additionally, it is non-destructive, fast, simple and only small amount of sample is required.

2.4.2 O/N analysis

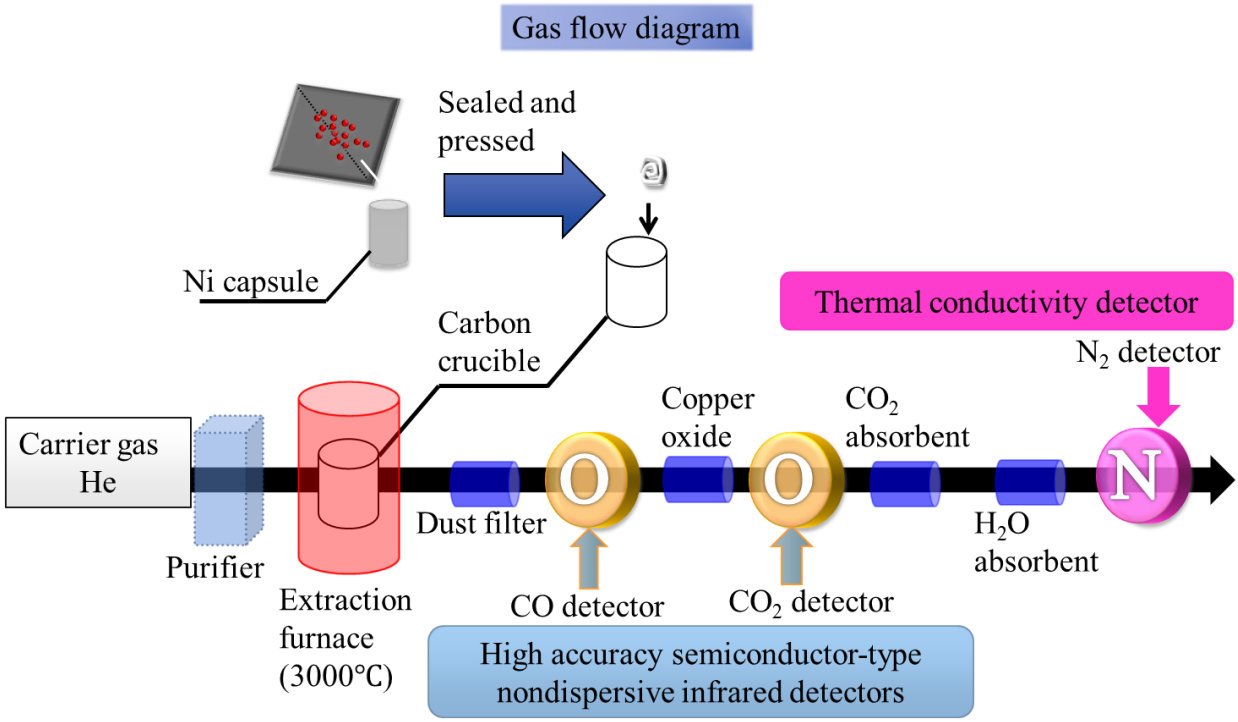

Figure 2.4.2 Gas flow diagram of the EMGA-820 Hot gas extraction technique [61]

Oxygen Nitrogen analysis was done by using EMGA-820 O/N analyzer. The device is a ceramic dedicated analyzer that can be quantitatively analyzed simultaneously oxygen and nitrogen content in the various ceramics with high accuracy and repeatability suiting to cutting-edge technology's R & D as well as quality control in the market of steel, new materials, catalyst and so on. The oxygen is measured as carbon monoxide and carbon dioxide by a non-dispersive infrared detector and the nitrogen by a thermal conductivity detector [61]. The 0.02 g of sample was placed in a graphite crucible and the crucible is maintained between the upper and the lower electrode of the impulse furnace. A high current power passes through the crucible to create a high temperature up to 3000 ^{o}C. The oxide in the

sample reacts with the graphite crucible and is extracted as carbon monoxide (CO) and carried together with the carrier gas. The extracted gas is directly analyzed after the dust filter. According to the oxygen concentration, it is determined by CO or CO_2 after pass throw Copper oxide used as oxidizer with non-dispersive Infra-Red analyzer (NDIR). The Hydrogen is determined with a non-dispersive Infra-red analyzer as H_2O after H_2 passes through the oxidizer. The nitrogen in the sample is extracted as nitrogen gas and its concentration is determined by a thermal conductivity detector (TCD). The hot gas extraction is a good technique since it takes few minutes to determine the O/N content of a sample. Yttrium oxide and silicon nitride were used as calibration standards for oxygen and nitrogen respectively.

2.4.3 Particle size distribution

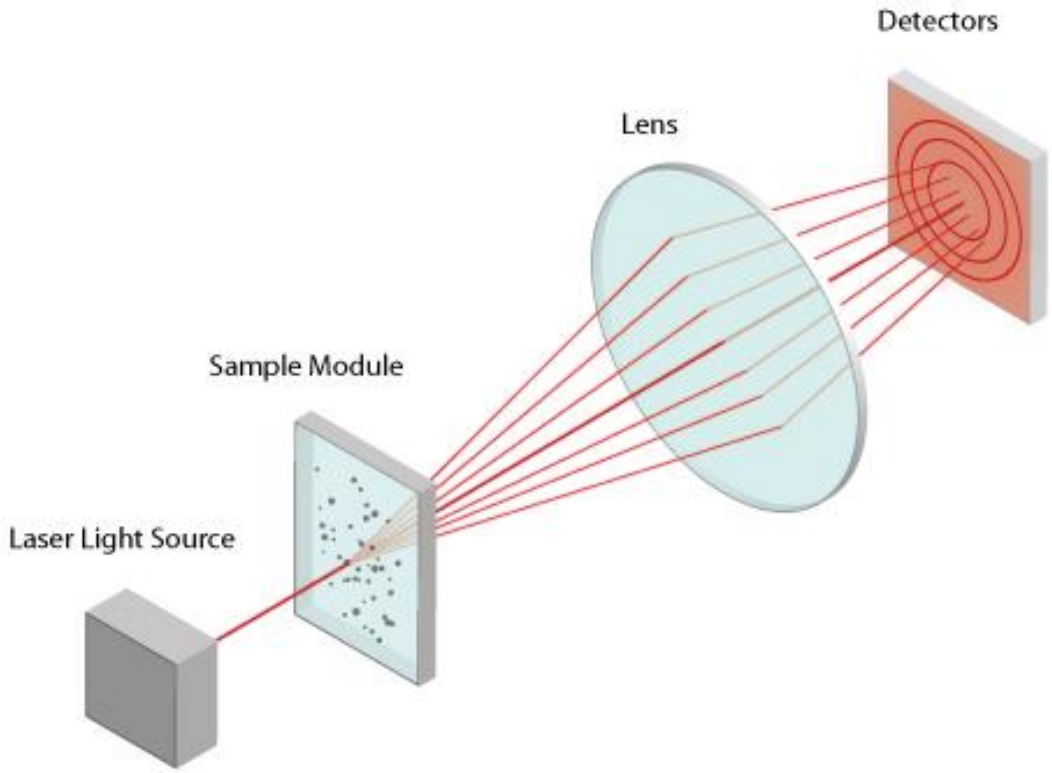

Figure 2.4.3.1 TRI LASER system [62]

Particle Size affects several properties of particulate materials and is an important index of quality and performance. For this reason it is important to measure and control the particle size distribution of many products. Recently, Laser Diffraction which is also called as Static Light Scattering has become one of the most popular technique used for the particle size distribution. Samples can be analyzed by either a liquid suspension or dry dispersion basis.

As shown in Fig 2.4.3.1 Laser beam is passed through the sample material which results in the laser light scattered at a wide range of angles. Detectors measure the intensity of light scattered at that position.

Fig.2.4.3.2 Particle size analyzer (Microtrac HRA X-100)

Particle size distribution of the oxynitride sample was measured by laser diffraction particle size analyzer (Microtrac HRA X-100). The Sample Delivery Controller (SDC) works in conjunction with several Microtrac Laser Diffraction systems. The SDC is fully automated and is designed to deliver a well-dispersed sample quickly and accurately. The sampler is equipped with a built-in ultrasonic probe to disperse the particles as they flow through the system to ensure consistent sample dispersion during measurement. Dispersion vessels are made up of surgical- grade stainless steel to protect the instrument from the corrosion. It is compactible to analyze organic or inorganic samples. It also includes self-cleaning mechanism which ensures no carry over from previous measurements.

The SDC is competent of delivering Wet dispersion or Dry Powder materials. 20mg of a powder sample was added to 7ml of an aqueous solution containing 0.2wt% of sodium hexametaphosphate and dispersed in the solution with ultrasonic waves. Results are shown and discussed in chapter 4 and 5 respectively.

2.4.4 X-ray photoelectron spectroscopy (XPS)

X-ray photoelectron spectroscopy (XPS), also known as Electron Spectroscopy for chemical analysis (ESCA) is a widely used technique to investigate the chemical composition of the surface. The valence state of each element in the oxynitride samples were evaluated by X-ray Photoelectron Spectroscopy (XPS). The XPS analyses were carried out in a KRATOS AXIS ULTRA instrument, equipped with an ultrahigh vacuum analytical chamber of base pressure ~2 x 10^{-9} Torr (=~3 x 10-7 Pa), a monochromatized Al K∝ X-ray source, a non monochromatized dual-anode X-ray source (Mg/Al), a hemispherical electron energy analyzer with multi-channel detector, an Ar^{+} sputter gun and a charge-compensating low-energy electron system. For XPS analysis, samples were lightly ground using a mortar and pestle, pressed into thin pellets, then mounted on stainless-steel stubs using double-sided

adhesive tape. The grinding was gentle to avoid damages to the samples, but was sufficient to overcome the effect of surface segregation and modification, especially surface oxidation of the samples during storage. All spectra presented here were excited using monochromatized Al K∝ radiation (hv = 1486.6eV), and with the hemispherical electron energy analyzer operated in the fixed analyzer transmission (FAT) mode. The charge-compensating low-energy electron system was used to minimize specimen charging during X-ray irradiation. The binding energy scale was calibrated using adventitious hydrocarbon referencing (C 1s = 285.0 eV).

Survey spectra, used in the quantitative analysis of the various elements present in each sample, were collected over the binding energy range 12000-0 eV (0.5 eV increments) at an analyzer pass energy of 80 eV. Elements identified in the samples were described in the chapter 4. To improve the signal-to-noise spectra were accumulated and added to produce a spectrum.

2.4.5 UV-Vis diffuse reflectance spectroscopy

Optical properties of the oxynitride powders were investigated by UV-Vis diffuse reflectance spectroscopy (JASCO V-550 DS) in the wave length range 250~900 nm. The measurements were performed in a double beam configuration using blank substrate as a reference. A PTFE (poly-tetrafluoroethylene) compact was used as a reference. 0.08 g of oxynitride powder for each samples were used to make pellet by manual compression molding machine. Approximately 10 mm diameter and 1 mm thickness of pellet were prepared for the UV-measurement. The bandgap of the oxynitrides was estimated based on the onset of diffuse reflectance. Results were briefly discussed in chapter 3, 4 and 5 respectively.

2.4.6 Scanning Electron Microscopy (SEM) S-4700 Hitachi

Scanning Electron Microscopy (SEM) uses a focused electron probe to extract structural and chemical information point by point from region of interest in the sample. The high spatial resolution of an SEM makes it a powerful tool to characterize a wide range of specimens at the nanometer to micrometer length scales.

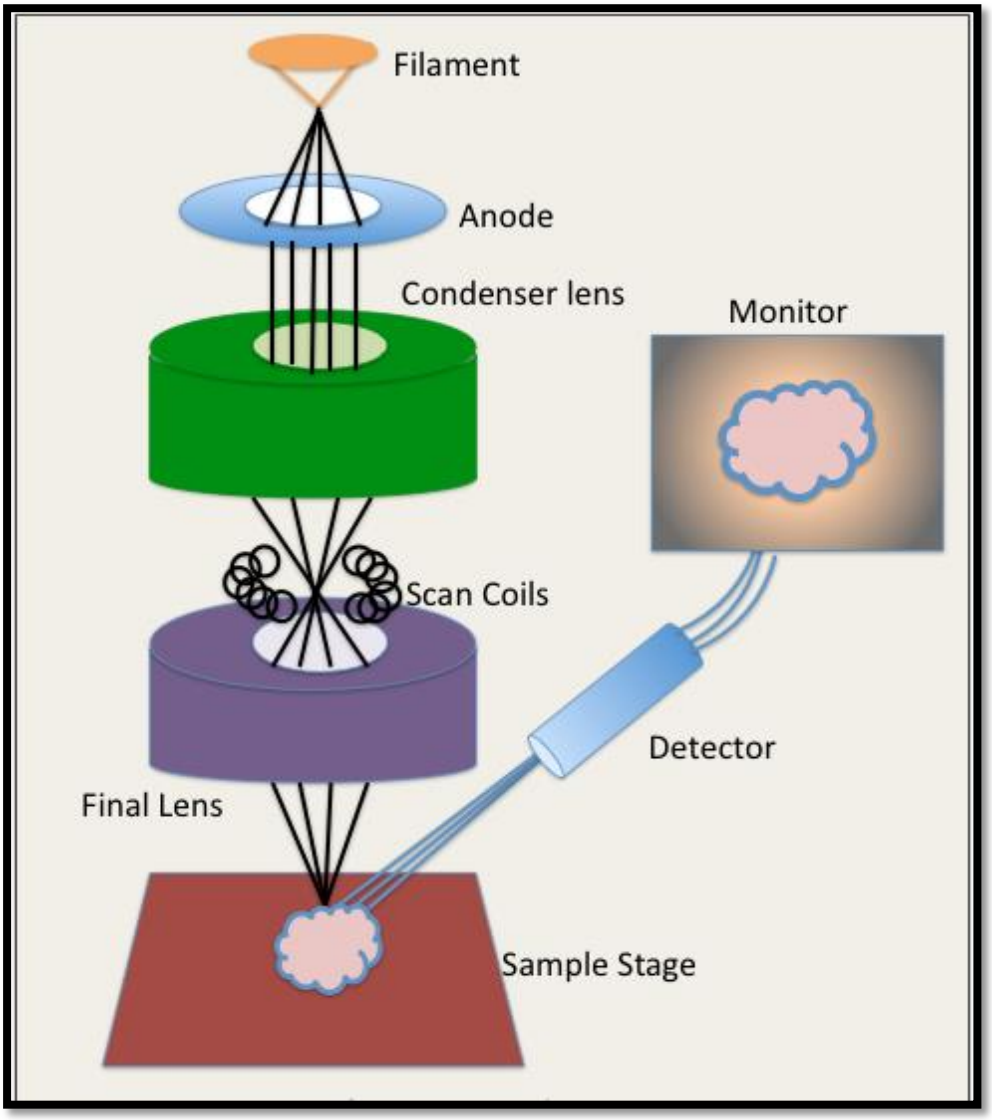

Figure 2.4.6.1 Instrumentation of SEM [63]

In most applications, data are collected over a selected area of the surface of the sample and a 2- dimensional image is generated that displays spatial variations in these properties.

Area ranging from approximately 1 cm to 5 microns in width can be imaged in a scanning mode using conventional SEM techniques (magnification ranging from 20X to approximately 30,000X, spatial resolution of 50 to 100nm). The SEM is also capable of performing analyses of selected point locations on the sample, this approach is especially useful in qualitatively or semi-quantitatively determining chemical compositions, crystalline structure and crystal orientations. The SEM uses electrons instead of light to form an image. A beam of electrons is produced at the top of the microscope by heating of a metallic filament. The electron beam follows a vertical path through the column of the microscope. It makes its way through electromagnetic lenses which focus and direct the beam down towards the sample. Once it hits the sample, other electrons backscattered or secondary are ejected from the sample. Detectors collect the secondary or backscattered electrons, and convert them to a signal that is sent to a viewing screen similar to the one in an ordinary television, producing an image.

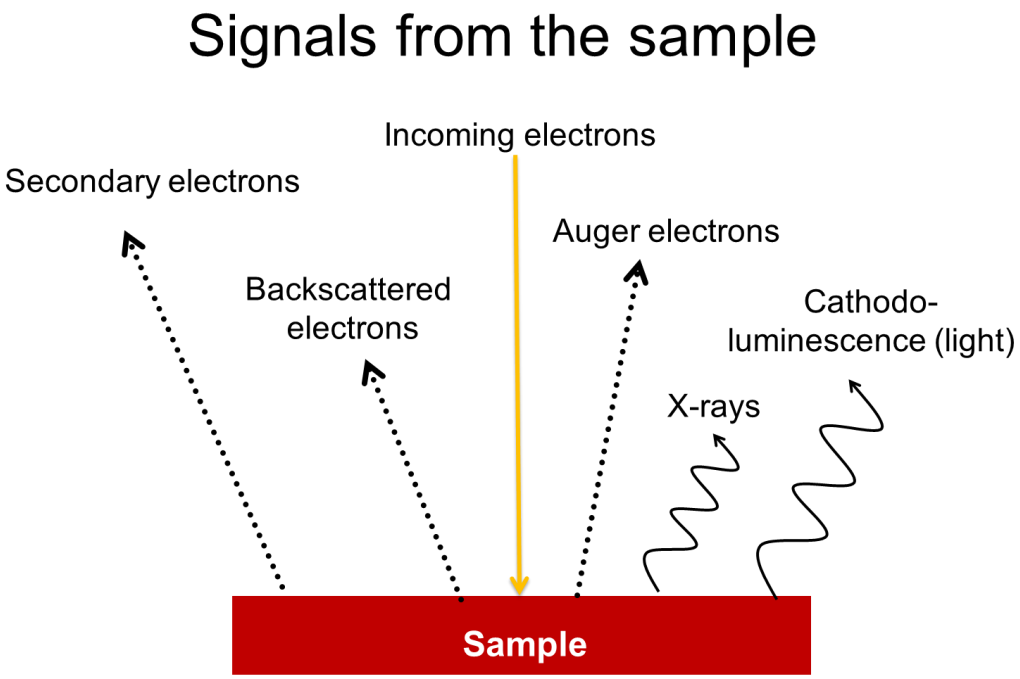

Figure 2.4.6.2 Types of the Signals Scattered from the sample [63]

The types of signals produced by a SEM include Secondary electrons (SE), backscattered electrons (BSE), characteristic X-rays (photon), visible light (cathodoluminescence-CL) and heat. Secondary electrons and backscattered electrons are commonly used for imaging samples; secondary electrons are most valuable for showing morphology and topography on samples. Due to their low energy, these electrons originate within a few nanometers from the surface. The luminousness of the signal is proportional to the number of secondary electrons that reach to the detector. Backscattered electrons are beam electrons that are reflected from the sample by elastic scattering. The most important contrast mechanism of BSE is the dependence of the backscattering coefficient on the mean atomic number. It can be used to detect contract between areas with different chemical composition. Since the brightness of the BE image tends to increase with the atomic number. X-ray generation is produced by inelastic collisions of the incident electrons with electrons in discrete (shells) of atoms in the sample that can be detected by EDS (Energy dispersive spectroscopy). EDS is able to identify the chemical elements presented in the analyzed sample. Results were discussed in chapter 5. A Hitachi S-4700 SEM (Japan, Tokushima University) and Philips XL-30 field emission gun scanning electron microscope (New Zealand, Auckland University) were used for all the oxynitride samples.

2.4.7 TEM

Electron diffraction and high resolution studies were done by transmission electron microscopy (TEM). The voltage for the TEM varies between the different models from 100 kV to 400 kV. Resolution in TEM is much higher than SEM and can achieve 0.5nm. The energy of the electrons determines the relative degree of their penetration in a specific sample from which useful information may be obtained. Electrons are accelerated in the same way as in the SEM, but pass through the specimen. TEM is often used to determine the detailed

crystallography of materials. It is complementary tool to other crystallographic methods such as X-ray diffraction. A copper grid with a holey carbon film was used to mount a small amount of the Sr_2TaO_3N oxynitride samples. Electron diffraction micrographs were obtained by using a JEOL 2100F at 200kV field emission electron microscope.

2.4.8 XRF

X-ray fluorescence (XRF) is an analytical technique that uses the interaction of x-rays with a material to determine its elemental composition. XRF is suitable for solid, liquid, powders, alloy as well as thin films. There are two main XRF methodologies –

a) Energy dispersive (EDXRF)

b) Wavelength dispersive (WDXRF)

The range of detectable elements varies according to instrument configuration and set up, WDXRF analyze oxygen through uranium (O → U).

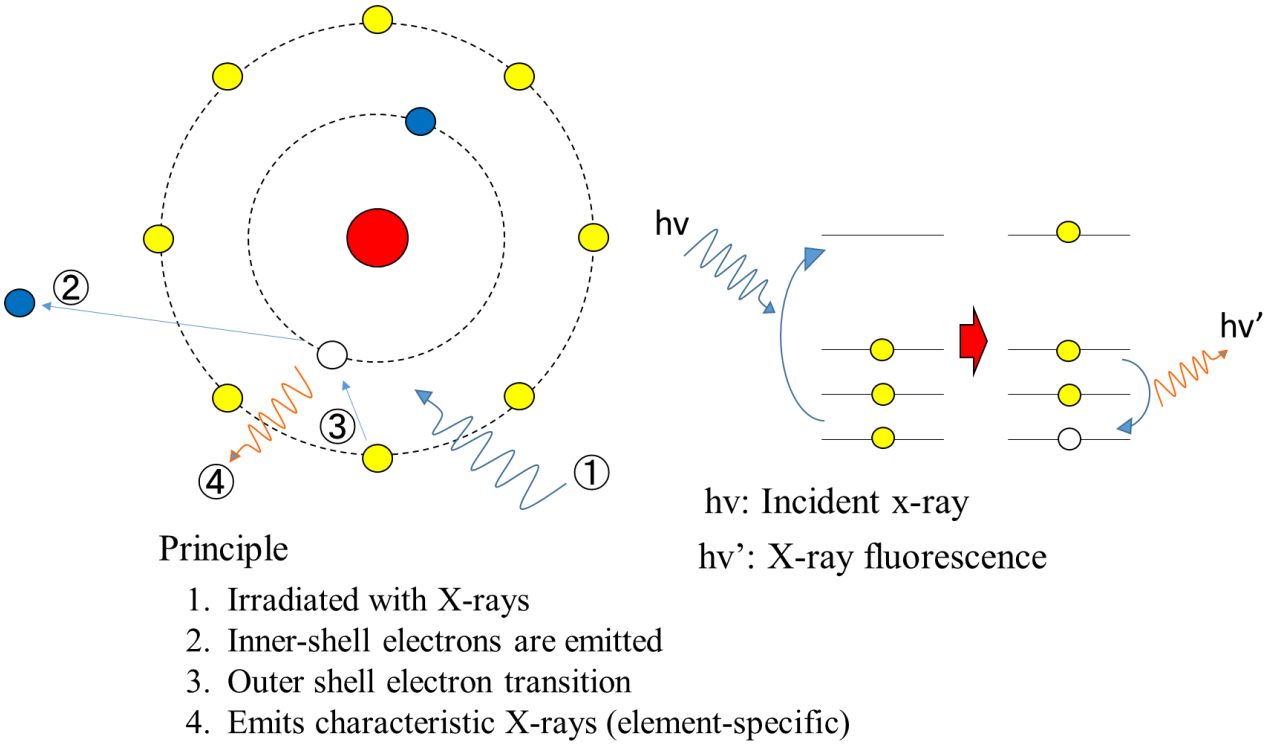

Figure 2.4.8 Mechanism of X-ray fluorescence [65]

XRF is widely used as a fast characterization tool in many analytical labs across the world, for applications as diverse as metallurgy, forensics, polymers, electronics, archaeology, environmental analysis, geology and mining. In this research work Rigaku supermini 200 wavelength dispersive (WDXRF) X-ray fluorescence spectrometer were used for the elemental analysis.

Chapter 3

$(Ba_{1-(x+y)}Sr_xEu_y)_2Si_6O_{12}N_2$ Phosphors for White LED Applications

3.1 Introduction

In the present study, we focus on the synthesis, structural and optical characterization of silicon rich $(Ba_{1-(x+y)}Sr_xEu_y)_2Si_6O_{12}N_2$ phosphors, with strontium content (x) = 0-0.6 and europium content (y) = 0.05-0.25. The optical properties of these phosphors are also compared with a commercial YAG:Ce^{3+} phosphor to illustrate their potential for white LED applications. $(Ba_{1-(x+y)}Sr_xEu_y)_2Si_6O_{12}N_2$ oxynitride phosphors were successfully synthesized by the solid-state reaction method at 1200°C under a H_2(5%) + N_2(95%) atmosphere. The Sr^{2+} content (x) was varied in the range 0-0.6 and the Eu^{2+} content varied in the range 0.05-0.25, with the Si/(Ba+Sr+Eu) ratio fixed at 3. In our previous study it was found that the silicon-rich phosphor $(Ba_{0.95}Eu_{0.05})_2Si_6O_{12}N_2$ with Si/(Ba+Eu) = 3 demonstrated a stronger emission intensity compared to the parent compound $(Ba_{0.95}Eu_{0.05})_3Si_6O_{12}N_2$ with Si/(Ba+Eu) = 2. In addition, silicon-rich phosphors were easier to isolate in pure form by the solid state reaction method than the parent phosphor with Si/(Ba+Eu) = 2. An excess of silicon in the form of SiO_2 was proposed to act as a flux to promote the formation of a nearly stoichiometric $(Ba_{0.95}Eu_{0.05})_2Si_6O_{12}N_2$ phase [24]

3.2 Experimental

The $(Ba_{1-(x+y)}Sr_xEu_y)_2Si_6O_{12}N_2$ phosphors were synthesized by using solid-state reaction method [19]. $BaCO_3$ (Kanto Chemicals, 99.9%), $SrCO_3$ (Kanto Chemicals, 96%), Si_3N_4 (Aldrich, 98.5%), SiO_2 (Aldrich, 99.8%), Eu_2O_3 (Kanto Chemicals, 99.5%) were used as starting materials. The required amounts of each compound were mixed for 40 min in agate mortal and then fired at 1200 ^oC for 5 h under a 5% H_2 in N_2. The molar ratio Si/(Ba + Sr +

Eu) of 3 was fixed for all samples. X-ray diffraction data (Rigaku RINT-2500VHF+ with a CuKα source) was collected in the 2θ range of 10-80°. Photoluminescence spectra were measured at room temperature using a fluorescent spectrophotometer (FP-8300, JASCO Japan). Spectra were excited at 365 nm or 460 nm, and emission spectra recorded over the range 400-700 nm.

3.3. Result and Discussion

Fig. 3.3.1 shows powder XRD patterns for the $(Ba_{0.95-x}Sr_xEu_{0.05})_2Si_6O_{12}N_2$ phosphors with a Sr content (x) of 0-0.6 (i.e. a Sr ratio of 0-60%, respectively). At Sr ratios up to 50%, the XRD patterns for all samples were near identical and typical for $Ba_3Si_6O_{12}N_2$-type materials. The data confirms the ability of the parent $Ba_3Si_6O_{12}N_2$ structure (Fig.1.2) to tolerate both significant Ba^{2+}-site cation deficiency and also Ba^{2+} substitution by smaller Sr^{+} and Eu^{2+} cations. A $SrSiO_3$ impurity was identified when the Sr ratio was increased to 60% (Fig. 3.3.1).

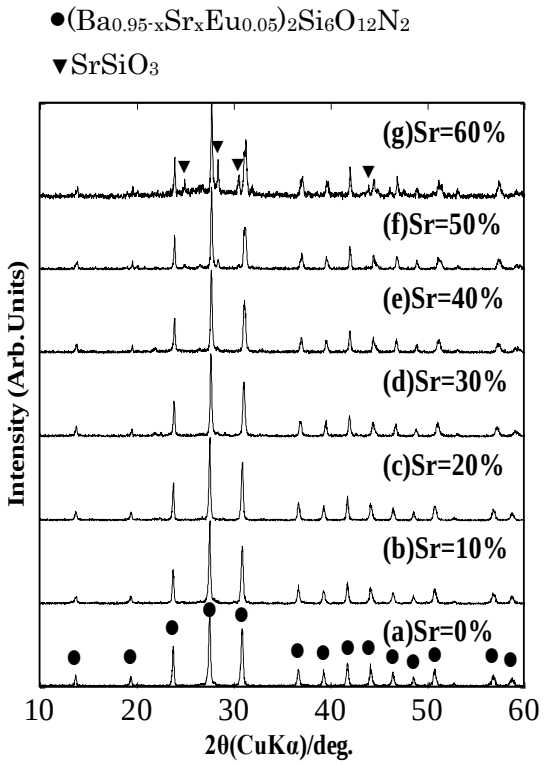

Fig.3.3.1 XRD patterns for $(Ba_{0.95-x}Sr_xEu_{0.05})_2Si_6O_{12}N_2$ phosphors (x= 0-0.6). The circles show the phosphor peaks, the triangles the $SrSiO_3$ phase formed at high Sr ratios

As expected, the substitution of Ba^{2+} by Sr^{2+} resulted in a progressive decrease in the a-axis and c-axis lattice parameters, and thus a significant reduction in the overall unit cell volume (Fig. 3.3.2). As the Sr ratio was increased from 0-50%, the a-axis lattice parameter decreased by 0.049 nm (-0.65%) and the c-axis parameter by 0.060 nm (-0.92%). These decreases are reasonable considering the relative ionic radii of Ba^{2+} (149 ppm) and Sr^{2+} (132 ppm).

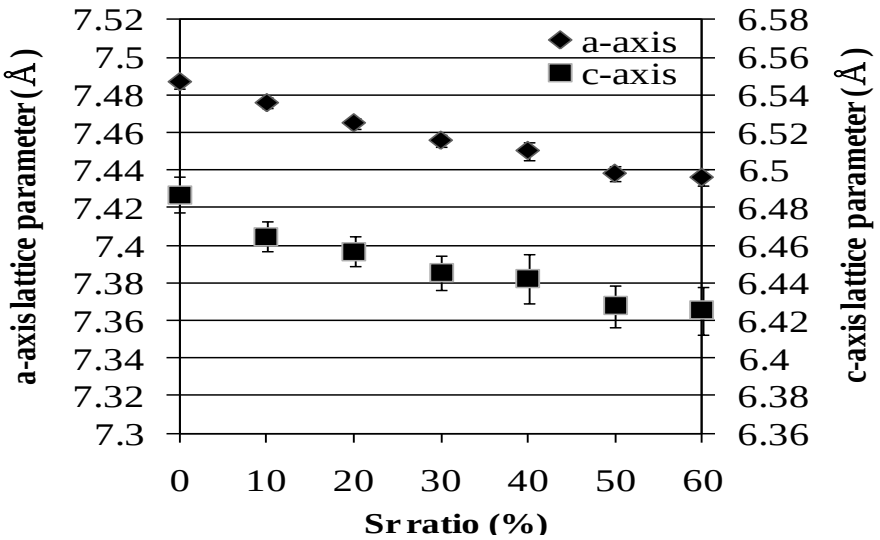

Fig. 3.3.2 Lattice parameters of $(Ba_{0.95-x}Sr_xEu_{0.05})_2Si_6O_{12}N_2$ phosphors as a function of barium substitution by strontium

The decrease in the unit cell parameters and unit cell volume with Ba^{2+} replacement by Sr^{2+} were expected to change the emission properties of the $(Ba_{1-(x+0.05)}Sr_xEu_{0.05})_2Si_6O_{12}N_2$ phosphors, since the oxygen coordination sphere around the Eu^{2+} cations (also on Ba^{2+} sites) was expected to be distorted accordingly. This is confirmed visually in Fig.3.3.3, where a progressive red-shift in the emission from green to yellow-green was observed as the Sr ratio was increased from 0-50 %.

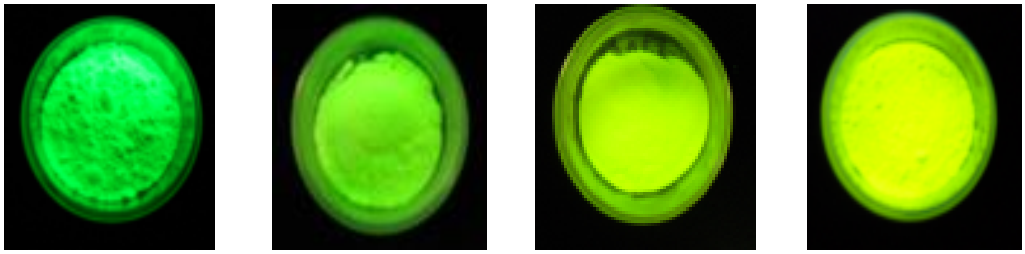

Sr 0% **Sr 10%** **Sr 20%** **Sr 50%**

.

Fig.3.3.3 Digital photographs of $(Ba_{0.95-x}Sr_xEu_{0.05})_2Si_6O_{12}N_2$ phosphors (x= 0-0.5) under UV (365 nm) excitation

Figure 3.3.4 shows emission spectra for $(Ba_{0.95-x}Sr_xEu_{0.05})_2Si_6O_{12}N_2$ phosphors excited under UV irradiation. The emission spectra result from 5d to 4f electronic transitions of the Eu^{2+} cations, and confirm a progressive red-shift in the emission wavelength on substitution of Ba^{2+} with Sr^{2+}. Interestingly, the emission intensity decreased almost linearly with the Sr^{2+} ratio in the range 0-50% (Table 3.3.1.)

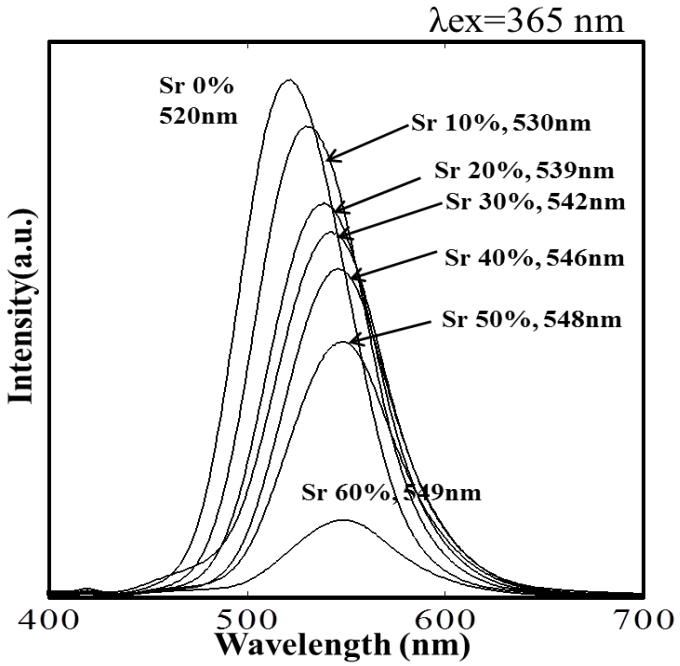

Fig.3.3.4 Emission spectra of $(Ba_{0.95-x}Sr_xEu_{0.05})_2Si_6O_{12}N_2$ phosphors (x=0-0.6) under UV (365 nm) excitation

.

Fig. 3.3.5 shows the emission peak wavelength plotted against the a-axis and c-axis lattice parameters for the $(Ba_{0.95-x}Sr_xEu_{0.05})_2Si_6O_{12}N_2$ phosphors. The data supports the hypothesis that Sr^{2+} doping and the associated lattice shrinkage affects the local coordination of Eu^{2+} cations (by altering Eu-O and possibly Eu-N distances and bond angles), resulting in the redshift in emission wavelengths of the phosphors.

Table 3.3.1 Emission peak maximum and normalized emission intensity for $Ba_{0.95-x}Sr_xEu_{0.05})_2Si_6O_{12}N_2$ phosphors (x=0-0.6) under UV (365 nm) excitation

Sr ratio	0%	10%	20%	30%	40%	50%	60%
λ (nm)	520	530	539	542	546	548	549
Intensity (%)	100	91	76	70	63	49	15
N/O ratio	0.216	0.205	0.191	0.190	0.188	0.179	0.167

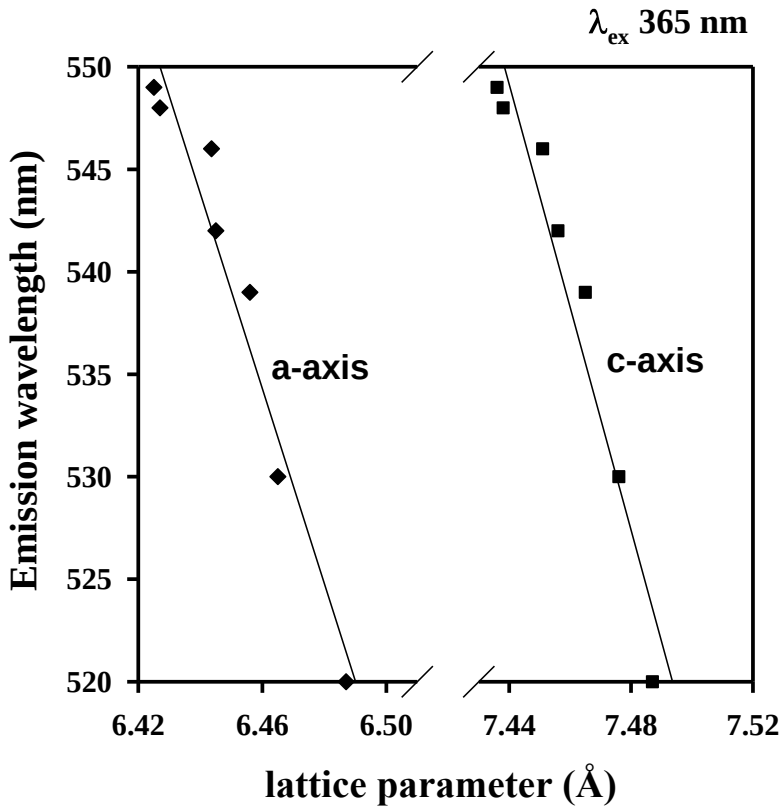

Fig.3.3.5 Relationship between the emission wavelength and the lattice parameters for $(Ba_{0.95-x}Sr_xEu_{0.05})_2Si_6O_{12}N_2$ phosphors phosphors (x=0-0.6)

It is useful to speculate further on the exact cause of the redshift seen in the emission profiles of Fig. 3.3.4 with the introduction of Sr^{2+}. Fig.3.3.6 shows one possibility, wherein the introduction of Sr^{2+} into the crystal structure modifies the octahedral crystal field of the Eu^{2+} cations, increasing the 5d octahedral crystal field splitting and stabilizing the t_{2g} orbitals involved in the emission process. The resulting decrease in the energy gap between the t_{2g} and 4f states red-shifts the emission maximum.

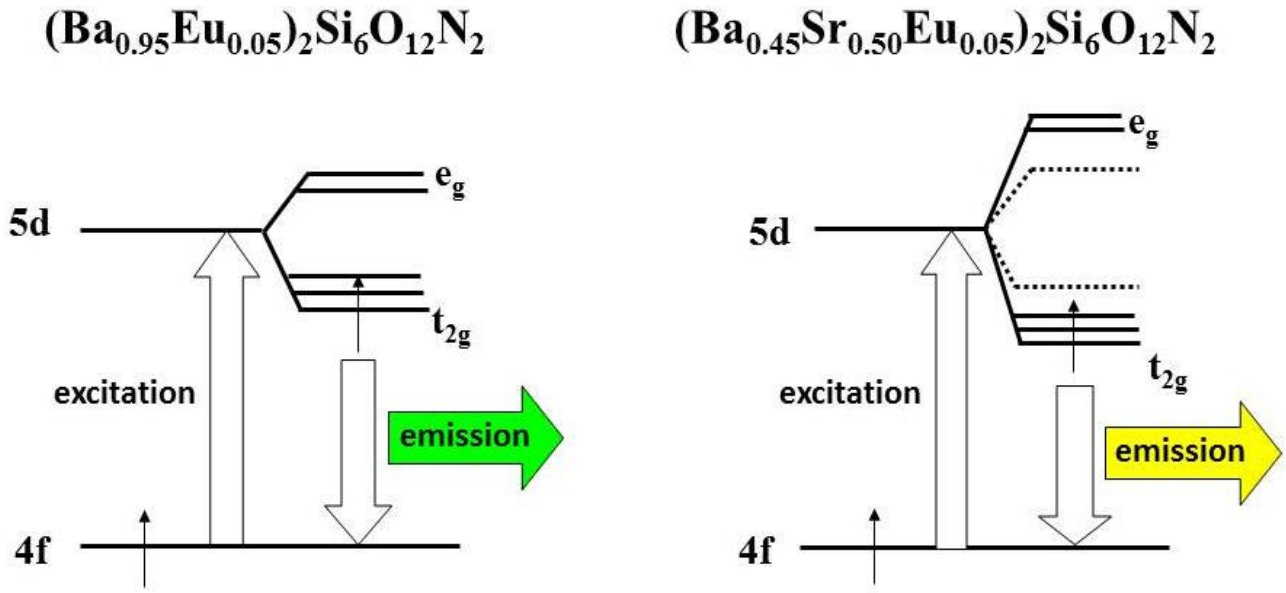

Fig. 3.3.6 Schematic diagrams showing excitation and emission processes in $(Ba_{0.95}Eu_{0.05})_2Si_6O_{12}N_2$ and $(Ba_{0.45}Sr_{0.50}Eu_{0.05})_2Si_6O_{12}N_2$

The decrease in the emission intensity with Ba^{2+} substitution by Sr^{2+} (Fig. 3.3.4, Table 3.3.1) was likely of chemical origin, relating to the anion stoichiometry in the $(Ba_{0.95-x}Sr_xEu_{0.05})_2Si_6O_{12}N_2$ phosphors. Table 3.3.1 shows that the N/O ratio in the phosphors decreased progressively with increasing Sr ratio. Thus, the efficiency of the emission process appears to depend strongly on the anion composition, with higher N/O ratios being optimal.

Fig. 3.3.7 shows XRD patterns for $(Ba_{0.8-y}Sr_{0.2}Eu_y)_2Si_6O_{12}N_2$ phosphors synthesized at different Eu^{2+} ratios and a fixed Sr ratio of 20 %. The XRD data shows that that $(Ba_{0.8-y}Sr_{0.2}Eu_y)_2Si_6O_{12}N_2$ phosphors are stable and can be prepared as a pure phase at Eu^{2+} ratios between 5-25 %, and possibly even higher loadings. This is not surprising, since the ionic radius of Eu^{2+} (131 pm) is almost identical to that of Sr^{2+} (132 pm), for which substitution at Sr^{2+} ratios up to 50 % in $(Ba_{0.95-x}Sr_xEu_{0.05})_2Si_6O_{12}N_2$ could be tolerated.

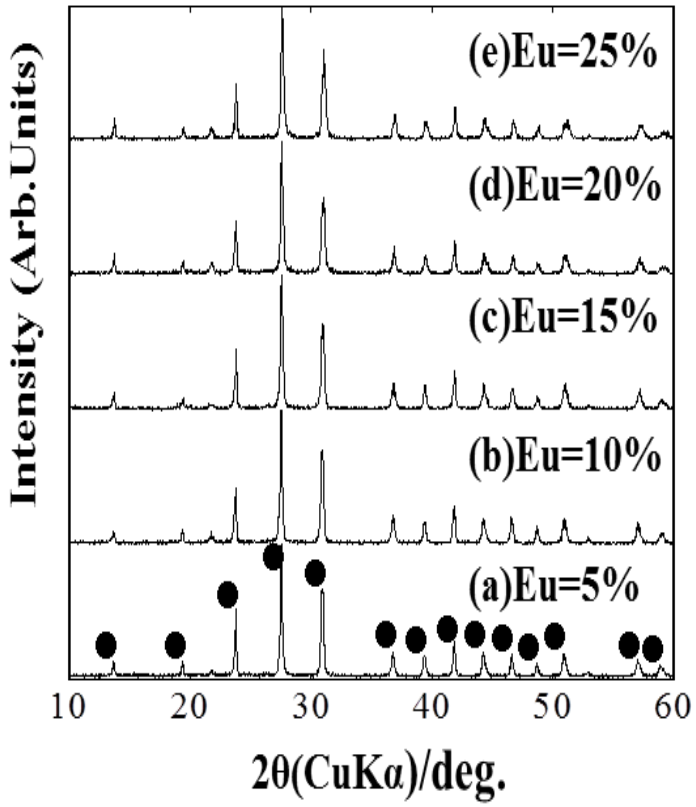

Fig.3.3.7 XRD patterns for $(Ba_{0.8-y}Sr_{0.2}Eu_y)_2Si_6O_{12}N_2$ phosphors (y= 0.05-0.25). The circles show the phosphor peaks. No impurity phases were identified

Fig.3.3.8 shows that the emission intensity of $(Ba_{0.8-y}Sr_{0.2}Eu_y)_2Si_6O_{12}N_2$ phosphors excited at 460 nm increased with Eu ratios up to 15% (i.e. y = 0.15), but then decreased at higher Eu

ratios. The data confirms that the Eu^{2+} in the phosphors efficiently absorbs blue light. The emission maximum red-shifted slightly with increasing Eu ratio and was centred around 539 nm for the $(Ba_{0.65}Sr_{0.2}Eu_{0.15})_2Si_6O_{12}N_2$ phosphor. Importantly, the emission intensity of the $(Ba_{0.65}Sr_{0.2}Eu_{0.15})_2Si_6O_{12}N_2$ phosphor was approximately twice that of a commercial YAG:Ce^{3+} phosphor under the same 460 nm excitation. The internal quantum efficiency of the $(Ba_{0.65}Sr_{0.2}Eu_{0.15})_2Si_6O_{12}N_2$ phosphor was approximately 73% at room temperature.

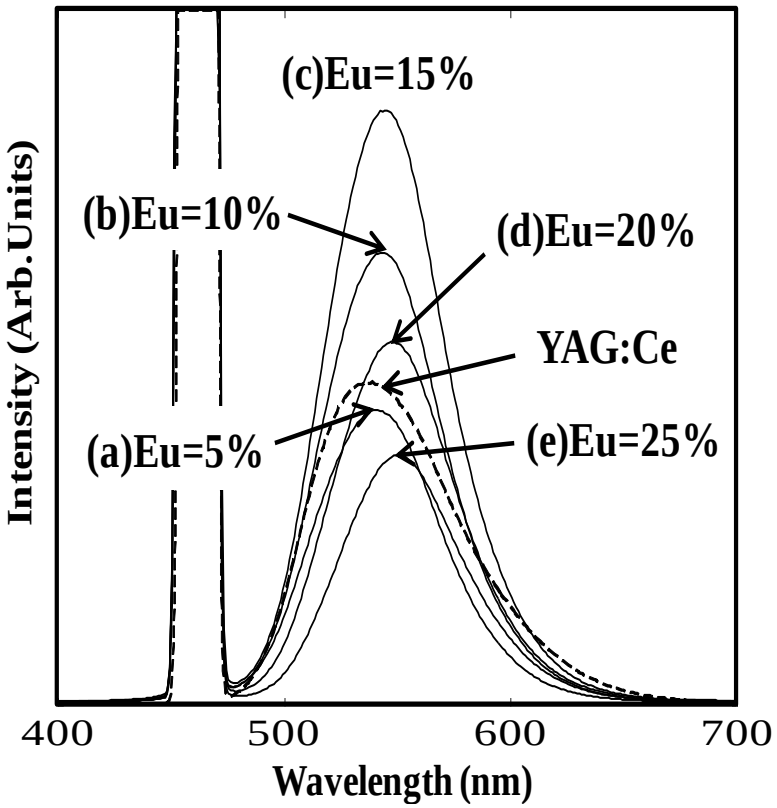

Fig.3.3.8 Emission spectra for $(Ba_{0.8-y}Sr_{0.2}Eu_y)_2Si_6O_{12}N_2$ phosphors (y= 0-0.25) and a YAG:Ce^{3+} phosphor. All spectra were excited at 460nm

Results confirm the potential of $(Ba_{1-(x+y)}Sr_xEu_y)_2Si_6O_{12}N_2$ phosphors for white LED applications. Currently we are attempting to further optimize the Si/(Ba + Sr + Eu) ratio and anion (N/O) stoichiometries in these materials to further redshift the emission maximum whilst maintaining high emission intensities.

3.4. Conclusion

$(Ba_{1-(x+y)}Sr_xEu_y)_2Si_6O_{12}N_2$ oxynitrides with a Si/(Ba + Sr + Eu) ratio of 3 demonstrate considerable promise as yellow emitting phosphors for white LED applications. Substitution of Ba^{2+} by Sr^{2+} up to x = 0.5 (at y = 0.05) causes shrinkage of the oxynitride lattice and redshifts the emission maximum from green (520 nm) to yellow-green (548 nm). The emission intensity decreased with Sr incorporation which coincided with a lowering of the N/O content in the phosphors. A $(Ba_{0.80-y}Sr_{0.20}Eu_y)_2Si_6O_{12}N_2$ phosphor, with y = 0.15, displayed superior emission characteristics to a commercial YAG:Ce^{3+} phosphor at room temperature under blue light (460 nm) excitation.

Chapter 4

Perovskite-type $LaTiO_2N$ synthesized using co-nitriding agents

4.1 Introduction

Inorganic pigments have been used in art and wall decorations since prehistoric times, and today still find widespread use in coating technologies due to their attractive optical properties and excellent weather resistance. Many inorganic pigments commonly used in paints (e.g. CdS, CdSe and $PbCrO_4$) contain heavy metals that pose a potential environmental hazard. Accordingly, there are strong economic and environmental drivers to develop alternative, low cost and non-toxic inorganic pigments for the paint and printing applications. Perovskite-type oxynitrides, especially $LaTiO_2N$, are very promising in this regard. The incorporation of nitrogen into metal oxides results in a considerable reduction in the bandgap, because N^{3-} is less electronegative than O^{2-}. As a consequently, the optical bandgap shifts toward higher wavelength in the visible light region. For example on nitriding $La_2Ti_2O_7$ to $LaTiO_2N$ the absorption edge red shifts from 3.2 eV to 2.2 eV. In this work, precursor mixtures of $La_2Ti_2O_7$ and urea or thiourea were prepared by sol-gel method and then subjected to thermal ammonolysis at 950^oC for 5 h. The products formed at different $La_2Ti_2O_7$:urea or $La_2Ti_2O_7$:thiourea mass ratios were systematically characterized by SEM, XRD, particle size distribution analysis, BET, UV-Vis, XPS and O/N analysis. The aims of the study were in two-fold; a) to establish the viability of using co-nitriding agents for the thermal ammonoloysis synthesis of oxynitrides; and b) to investigate the structure, purity and optical properties of the resulting $LaTiO_2N$ powders.

4.2 Experimental

Lanthanum nitrate hexahydrate, titanium tetraisopropoxide, ethylene glycol, citric acid, urea and thiourea were obtained from Wako Pure Chemical Industries, Ltd., Japan, and used without further purification. Ammonia gas was obtained from Sumitomo Seika Chemicals Co., Ltd., Japan, and passed through a cold trap to remove water vapour.

$LaTiO_2N$ powders were synthesized by the thermal ammonolysis of a $La_2Ti_2O_7$ precursor. Briefly lanthanum nitrate hexahydrate (2.165 g, 0.005 mol) and titanium tetra-isopropoxide (1.279 g, 0.0045 mol) were added to ethylene glycol (24.7g) at room temperature with constant stirring. A slight molar excess of La relative to Ti was used as this is beneficial for achieving bright orange $LaTiO_2N$ powders [31-33]. Citric acid (19.1 g) and distilled water (20 g) were then added to give a homogeneous solution. The resulting solution was then heated to 180 °C under constant stirring until a transparent gel formed. The transparent gel was first calcined at 350 °C for 4 h, and then calcined at 650 °C for 4 h to yield amorphous $La_2Ti_2O_7$.

To investigate the effect of the urea and thiourea addition on the thermal ammonolysis synthesis of $LaTiO_2N$, the $La_2Ti_2O_7$ precursor was physically mixed by grinding with urea (mass ratio $La_2Ti_2O_7$:urea = 1:2.5 or 1:5) or thiourea (mass ratio $La_2Ti_2O_7$:thiourea = 1:1, 1:2, 1:3, 1:4 and 1:5). The resulting powders were transferred to a 10 cm alumina boat which was then placed in an alumina tube reactor. Argon was flowed through the tube reactor, and then the reactor heated from room temperature to 950 ^oC at 15 ^oC min^{-1} under a flow of of ammonia gas (1 L min^{-1}). The samples were kept at 950 ^oC for 5 h under flowing ammonia, and then quickly cooled to room temperature (switching from ammonia gas to helium once the temperature was below 500 ^oC). The products were removed from the furnace, lightly ground in a mortar and pestle, and then subjected to detailed characterization.

4.3 Product characterization

The phase composition of the $LaTiO_2N$ products was examined by powder X-ray diffractometry (Rigaku RINT-2500VHF+). XRD data was recorded over the 2θ range 10-90^o using a monochromatized CuKα source (λ = 1.5406 Å) operated at 40 kV and 150 mA. Phase identification was made with reference to the JCPDS database. A laser diffraction particle size analyzer (Microtract HRA X-100) was used to determine the particle size of the oxynitride powders. For the analysis, oxynitride (20 mg) was dispersed in 7 mL of an aqueous sodium hexametaphosphate solution (0.2 wt.%). Particle sizes and morphologies were also evaluated by SEM (Philips XL-30 field emission gun scanning electron microscope). All micrographs were collected at an electron gun accelerating voltage of 5 kV. Specimens were mounted on black carbon tape and platinum sputter coated for analysis. The La:Ti ratio of the products was determined by XRF and inductively coupled plasma-atomic emission spectroscopy (ICP-AES, Seiko Instruments SPS1500VR). Anion contents were determined by the hot gas extraction method using a Horiba EMGA-920 analyzer (O/N analyzer). For the analysis, the sample was accurately weighed into a graphite crucible with Ni-Sn as flux and then heated to 3000 °C. Specific surface areas were determined by N_2 physisorption at 77 K according to the BET method (Micromeritics Tristar3000). X-ray photoelectron spectroscopy (XPS) was used to evaluate the near surface region chemical composition of the oxynitride products. XPS data were collected on a Kratos Axis UltraDLD Spectra were excited using monochromatic Al Kα X-rays (1486.7 eV) with the X-ray source operating at 100 W, and the spectra referenced against C 1s = 285.0 eV for adventitious hydrocarbons.

4.4 Results and discussion

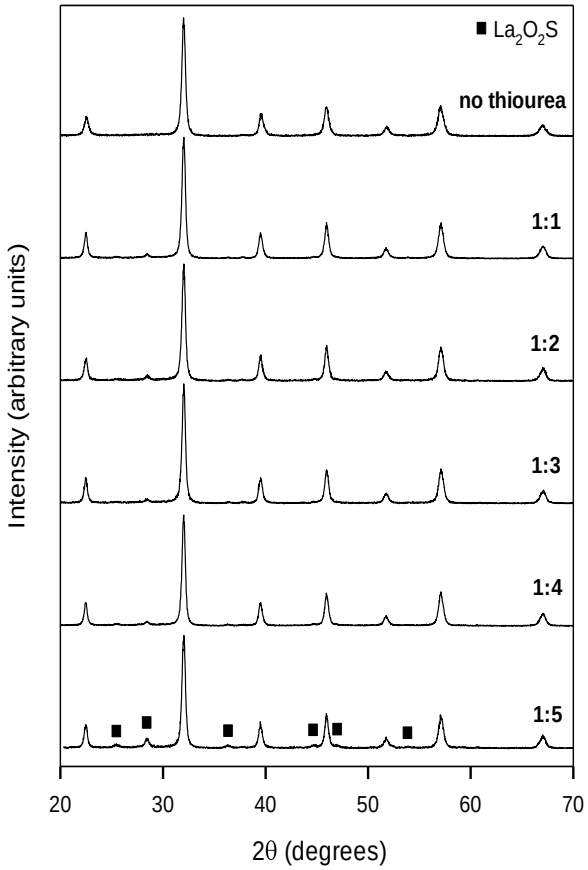

Fig. 4.4.1 Powder XRD patterns for $LaTiO_2N$ powders synthesized by the thermal ammonolysis method at 950 ^oC with thiourea as the co-nitriding agent. The mass ratio $La_2Ti_2O_7$:thiourea is shown on the right

Fig. 4.4.1 shows powder XRD patterns for the products obtained by the thermal ammonolysis of $La_2Ti_2O_7$:thiourea mixtures at 950 ^oC for 5 h. The sample prepared in the absence of thiourea shows peaks characteristic for perovskite-type $LaTiO_2N$ (JCPDS card No. 48-1230). Identical XRD patterns were obtained for $LaTiO_2N$ synthesized using urea as a co-nitriding agent (not shown). The XRD patterns for products prepared using thiourea as the co-nitriding agent were dominated by peaks due to $LaTiO_2N$, but also contained a La_2O_2S impurity (JCPDS card No. 27-0263). The La_2O_2S content in the products increased in proportion to the $La_2Ti_2O_7$:thiourea precursor ratio.

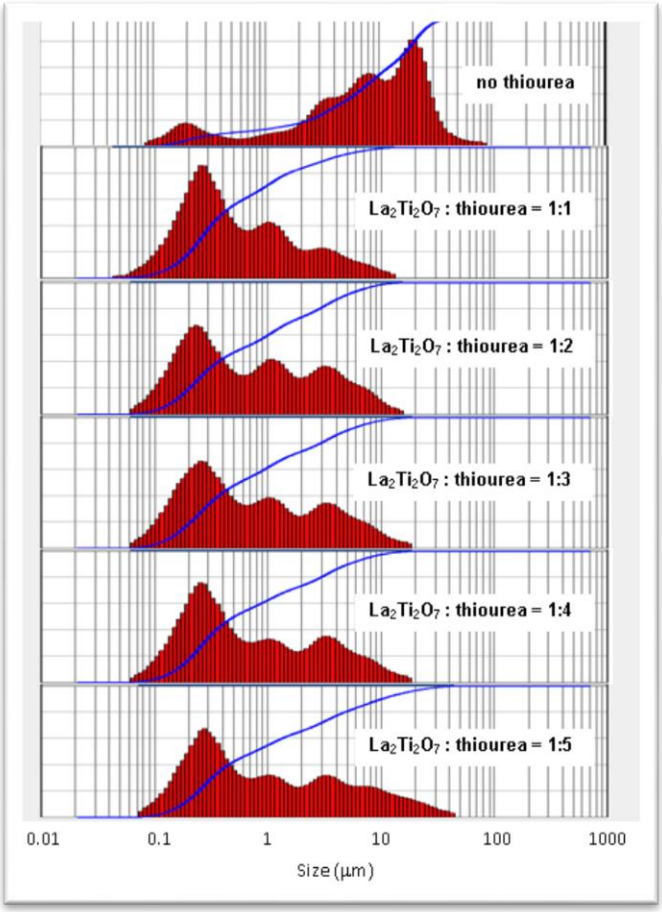

Fig. 4.4.2 Particle size distributions for $LaTiO_2N$ powders synthesized by the thermal ammonolysis method at 950 ^oC using thiourea as a co-nitriding agent

The particle size distribution of the $LaTiO_2N$ powders synthesized using thiourea as the co-nitriding agent are shown in Fig. 4.4.2 Median particles sizes are summarised in Table 4.4.1. In the absence of urea or thiourea, the median particle size of the $LaTiO_2N$ powder was 8.622 µm. The addition of urea or thiourea reduced the median particles size to < 1 µm. SEM confirmed a decrease in particle size when co-nitriding agents were used (Fig. 4.4.3).

The reduction in the median particle size of the $LaTiO_2N$ powders when using urea or thiourea and co-nitriding agents may be attributable to the higher extent of nitridation achieved (Table 4.4.1, O/N bulk ratio).

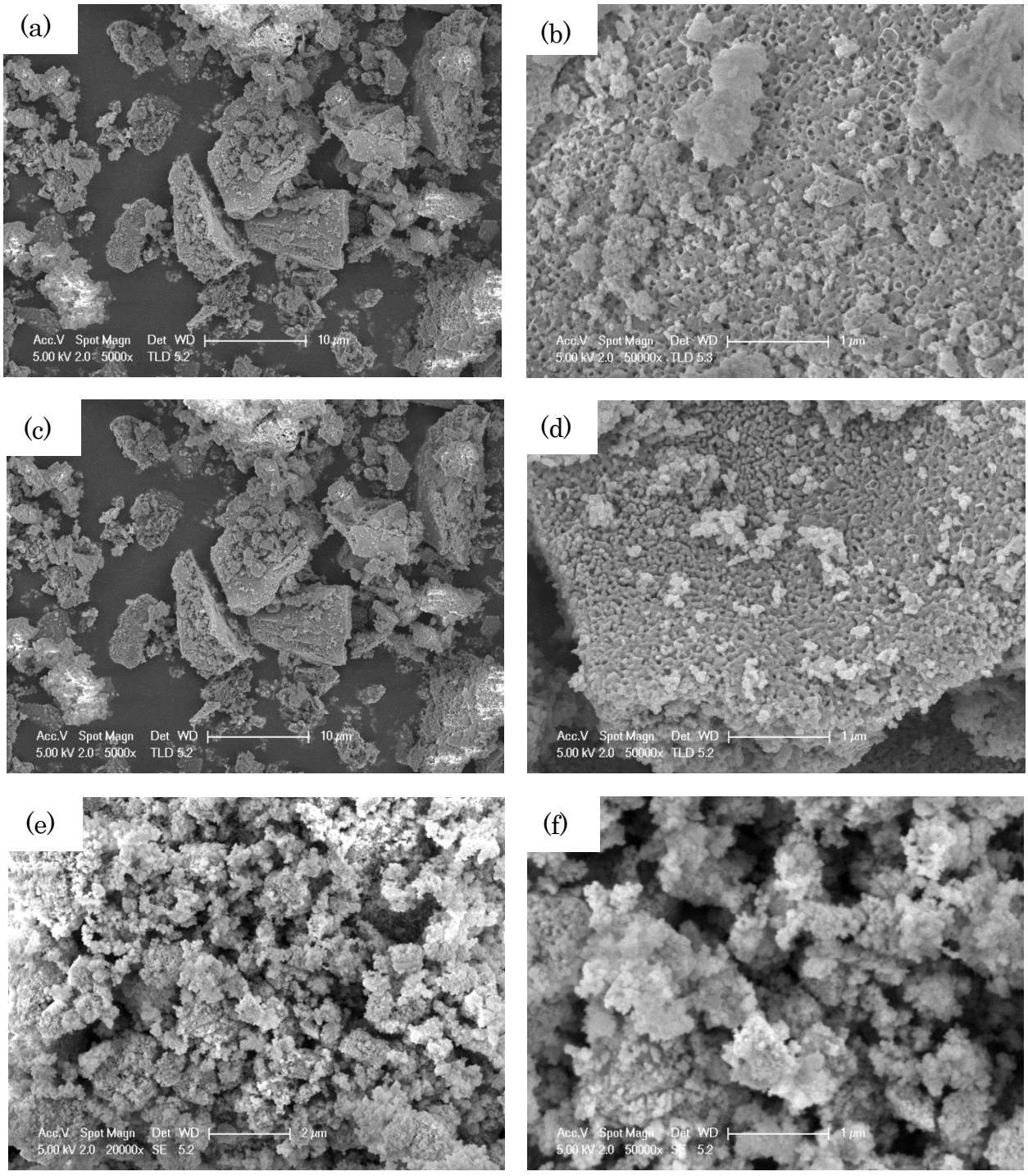

Fig. 4.4.3. SEM images for $LaTiO_2N$ powders synthesized by the thermal ammonolysis method at 950 ^oC (NH_3 1 L min^{-1}) with (a), (b) no co-nitriding agent; (c), (d) urea as the co-nitriding agent, molar ratio $La_2Ti_2O_7$:urea = 1:5, and (e), (f) thiourea as the co-nitriding agent, molar ratio $La_2Ti_2O_7$:thiourea = 1:5. Images on the right were all taken at 50000× magnification

The ammonolysis of $La_2Ti_2O_7$ to $LaTiO_2N$ at 950 ^oC can be written as;

$$La_2Ti_2O_{7(s)} + 2NH_{3(g)} \rightarrow 2LaTiO_2N_{(s)} + 3H_2O_{(g)} + \square$$

where $\square$ represents an anion vacancy. The accumulation of anion vacancies during nitridation introduces internal porosity into the $LaTiO_2N$ products, direct evidence for which can be seen in the SEM images of Fig. 4.4.3(b) and 4.4.3(d). The $LaTiO_2N$ products prepared using urea or thiourea were more nitrided than that prepared without co-nitriding agent (see O/N ratios, Table 4.4.1), and hence are expected to be more porous. For the particle size distribution measurements, the product powders were dispersed in aqueous sodium hexametaphosphate solution (0.2 wt.%) and then briefly ultrasonicated to achieve a stable dispersion. The ultrasonication step may have fragmented the porous $LaTiO_2N$ networks, with the effect being greater for the more porous powders prepared using urea or thiourea as co-nitriding agents. For $LaTiO_2N$ powders prepared using thiourea as the co-nitriding agent, the addition co-formation of La_2O_2S as a byproduct should also be considered and may also influence the particle size results**.**

Table 4.4.1 Summarised physical and optical data for $LaTiO_2N$ powders synthesized by thermal ammonolysis of $La_2Ti_2O_7$ at 950 ^oC in the absence or presence of urea or thiourea as co-nitriding agents

Ammonolysis precursor	Mean particle size (μm)	BET surface area (m^2g^{-1})	O (wt.%)	N (wt.%)	O/N molar ratio	Composition*	Colour	E_g (eV)
$La_2Ti_2O_7$	8.62	14.7	16.11	3.74	3.77	$LaTi(O_{0.79}N_{0.21})_{2.97}$		2.22
$La_2Ti_2O_7$:urea								
1:2.5	0.902	14.9	15.55	4.35	3.13	$LaTi(O_{0.76}N_{0.24})_{2.81}$		2.17
1:5	0.785	14.0	15.55	4.27	3.21	$LaTi(O_{0.79}N_{0.21})_{2.97}$		2.20
$La_2Ti_2O_7$:thiourea								
1:1	0.405	14.5	16.00	4.03	3.48	$LaTi(O_{0.78}N_{0.22})_{3.01}$		2.22
1:2	0.595	15.8	15.72	3.99	3.45	$LaTi(O_{0.78}N_{0.22})_{2.95}$		2.21
1:3	0.554	15.2	15.60	4.09	3.34	$LaTi(O_{0.77}N_{0.23})_{2.95}$		2.25
1:4	0.500	17.2	15.50	4.09	3.31	$LaTi(O_{0.78}N_{0.23})_{2.93}$		2.18
1:5	0.752	17.0	14.77	4.44	2.91	$LaTi(O_{0.75}N_{0.25})_{2.87}$		2.14

*** S in products obtained using thiourea as a co-nitriding agent was not quantified or included in the composition calculation.**

The optical properties of the different $LaTiO_2N$ products were evaluated using UV-Vis reflectance measurements, results for which are presented in Fig. 4.4.4. $LaTiO_2N$ prepared in the absence of urea or thiourea had a composition $LaTi(O_{0.79}N_{0.21})_{2.97}$ and a bandgap (E_g) of 2.22 eV (Fig.4.4.4(a), Table 4.4.1).

Similar values were found for $LaTiO_2N$ powders prepared using urea as a co-nitriding agent (Table 4.4.1), with the reflectivity above the absorption edge decreasing slightly when the $La_2Ti_2O_7$:urea precursor ratio was changed from 1:2.5 to 1:5. The decrease in reflectivity above the absorption edge was far more dramatic for $LaTiO_2N$ powders synthesized using thiourea as the co-nitriding agent (Fig. 4.4.4(b)). The powder prepared at a $La_2Ti_2O_7$:thiourea ratio of 1:5 was of very dark brown colour (Table 4.4.1), with a reflectivity less than 5% above the absorption edge (Fig. 4.4.4(b)). To explain the darkening of the $LaTiO_2N$ powders when thiourea was used as the co-nitriding agent, the concomitant formation of La_2O_2S needs to be considered (c.f. Fig. 4.4.2). La_2O_2S is a white solid and as such is not directly responsible for the darkening of the products. However, the formation of La_2O_2S will modify the La:Ti ratio of the $LaTiO_2N$ products, eventually resulting in an excess of Ti relative to La. Our previous studies have shown that ammonolysis of oxide precursors with La:Ti ratios less than 1 (i.e. 0.8 or 0.9) results in very dark $LaTiO_2N$ powders due to the presence of excess bulk Ti^{3+} centers [36-38].

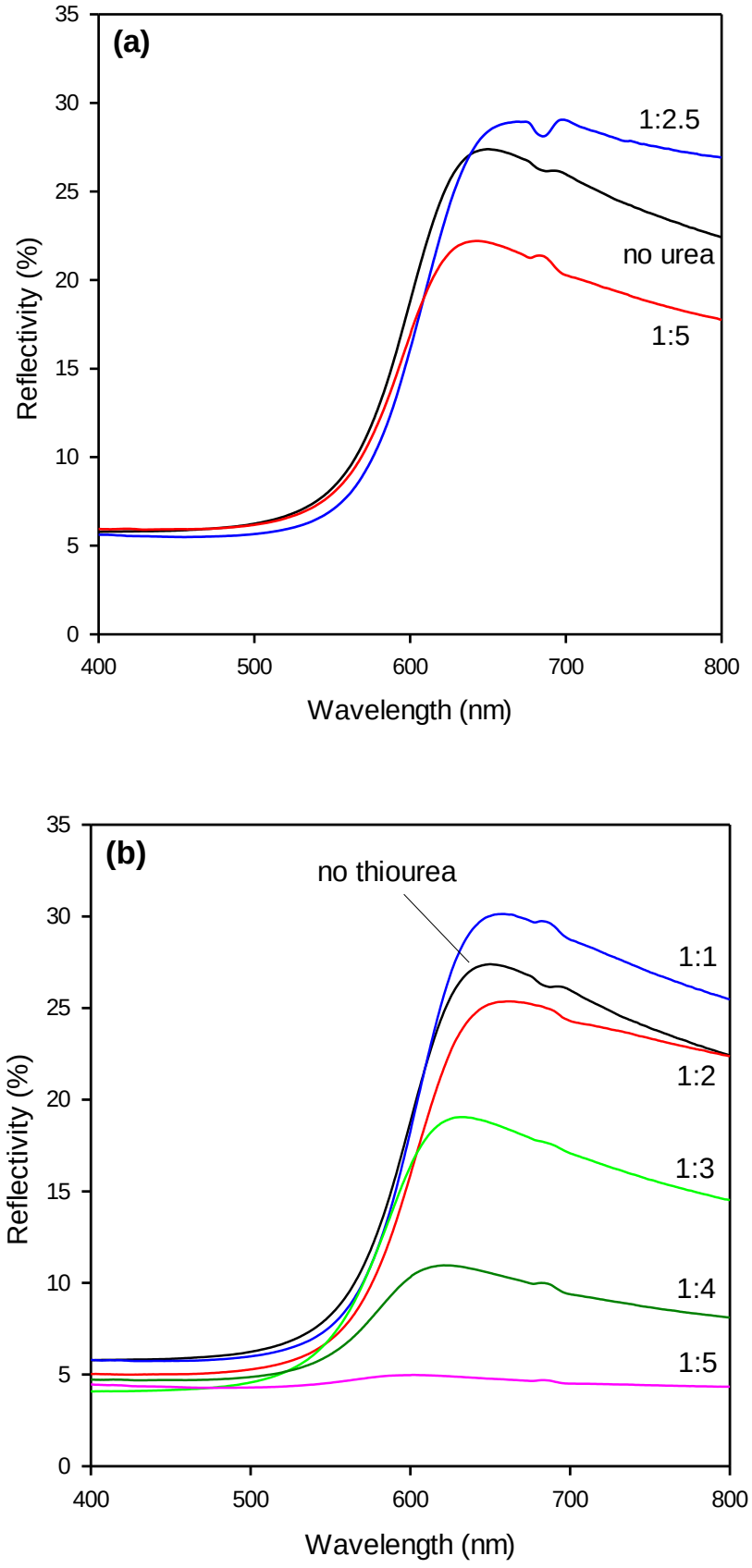

Fig. 4.4.4. UV-Vis reflectance spectra for (a) $LaTiO_2N$ powders synthesized using urea as a co-nitriding agent; and (b) $LaTiO_2N$ powders synthesized using thiourea as a co-nitriding

The progressive decrease in the reflectivity of the powders in Fig. 4.4.4(b) with increasing thiourea content in the precursor mixture can be rationalised on this same basis. It should be noted that the $LaTiO_2N$ structure can tolerate an excess of La relative to Ti without affecting the optical properties [36-38].

XPS was used to examine the near surface region chemical composition of the $LaTiO_2N$ products. Of particular interest were the speciation of titanium and sulfur in the $LaTiO_2N$ powders sysnthesized using thiourea as a co-nitriding agent. Fig. 4.4.5(a) and 4.4.6(b) show Ti 2p and N 1s XPS spectra, respectively, for $La_2Ti_2O_7$ and $LaTiO_2N$ powders synthesized with different amounts of urea as a co-nitriding agent.

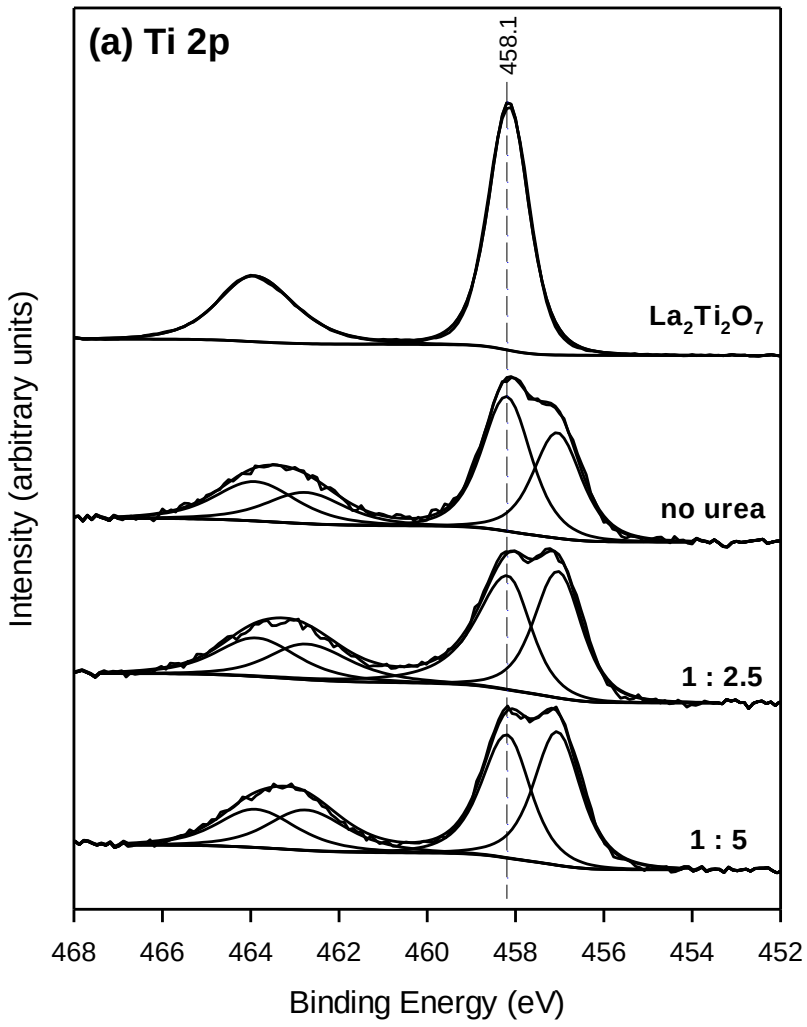

As expected, the $La_2Ti_2O_7$ powder showed peaks at 458.1 and 463.9 eV, assigned to the Ti $2p_{3/2}$ and Ti $2p_{1/2}$ peaks, respectively, of Ti^{4+}. Following ammonolysis, additional Ti 2p peaks appear on the low binding energy side of the Ti^{4+} features, which are assigned to Ti^{3+} species (Ti $2p_{3/2}$ = 457.0 eV). Core level electrons in Ti^{3+} species experience a weaker coulombic attraction to the nucleus than electrons in Ti^{4+} species, which accounts for the shift of the Ti 2p peaks to lower binding energies upon Ti^{4+} reduction to Ti^{3+}

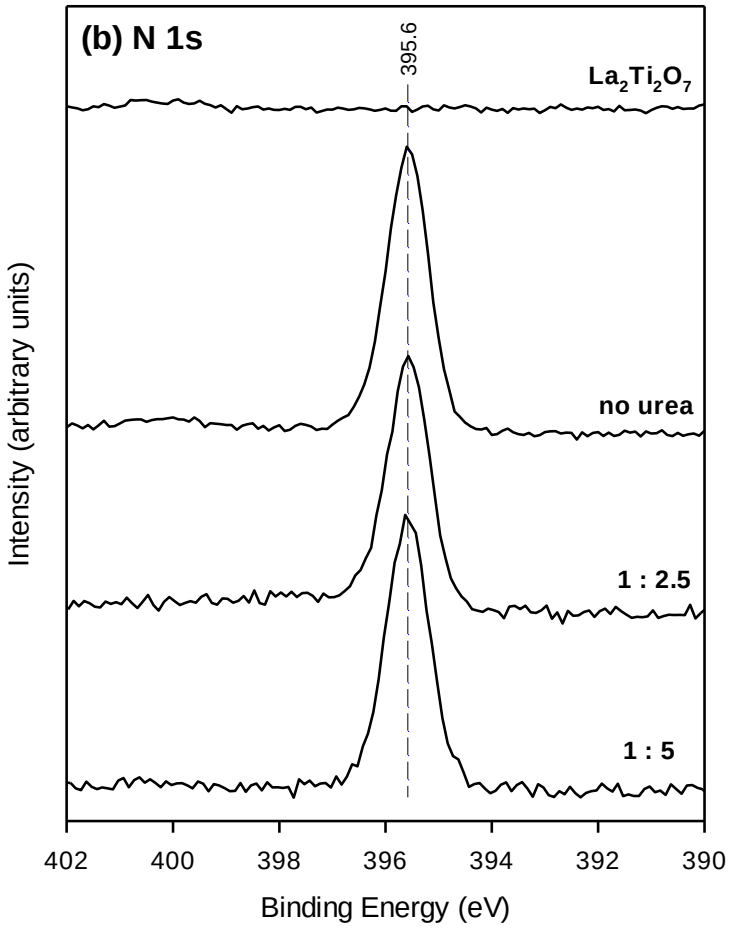

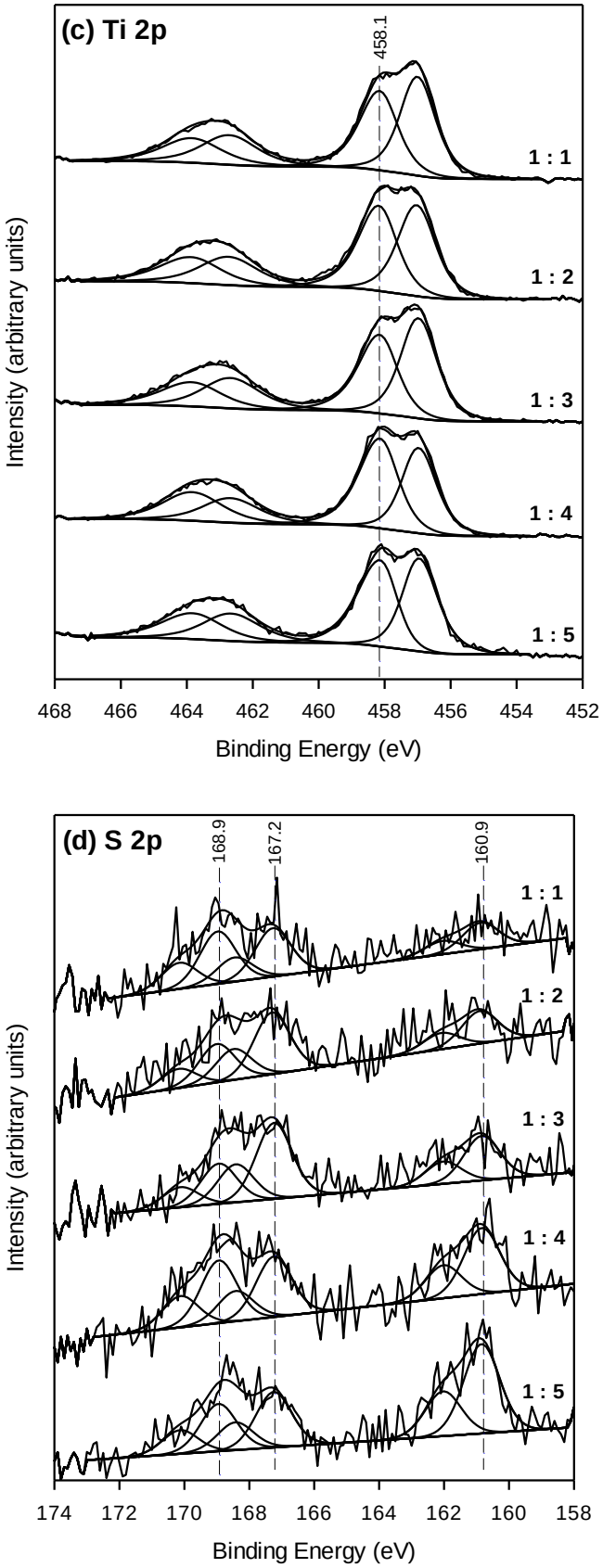

Fig. 4.4.5. (a) Core level Ti 2p and N 1s XPS spectra for $La_2Ti_2O_7$ and $LaTiO_2N$ powders prepared using urea as a co-nitriding agent; (b) Core level Ti 2p and S 2p XPS spectra for $LaTiO_2N$ powders prepared using thiourea urea as a co-nitriding agent

Table 4.4.2 Summarised XPS data for $LaTiO_2N$ powders synthesized by thermal ammonolysis of $La_2Ti_2O_7$ at 950 ^oC in the absence or presence of urea or thiourea as co-nitriding agents

$LaTiO_2N$ precursor	Atom ratios			
	La/Ti	N/Ti	S/Ti	Ti^{3+}/Ti^{4+}
$La_2Ti_2O_7$	1.17	0.53	0.00	0.78
$La_2Ti_2O_7$: urea				
1:2.5	1.35	0.62	0.00	0.92
1:5	1.30	0.60	0.00	1.06
$La_2Ti_2O_7$: thiourea				
1:1	1.24	0.59	0.14	1.15
1:2	1.28	0.57	0.13	1.01
1:3	1.27	0.63	0.20	1.17
1:4	1.29	0.63	0.20	0.83
1:5	1.30	0.66	0.23	1.00

The formation of Ti^{3+} on nitridation of $La_2Ti_2O_7$ and $LaTiO_2N$ agrees with theory, since the nitridation is accompanied by the creation of anion vacancies about Ti cations (B sites in the perovskite lattice).

The N/Ti and Ti^{3+}/Ti^{4+} ratios found for the $LaTiO_2N$ powders synthesized in the presence of urea (Table 4.4.2) were higher than values determined for $LaTiO_2N$ synthesized without urea, confirming a greater extent of nitridation when urea was used. The data lends strong support to the argument that urea is a highly beneficial co-nitridation agent for the synthesis of $LaTiO_2N$. All $LaTiO_2N$ powders were characterized be a single N 1s feature at 395.6 eV (Fig. 4.4.5(b)), which is characteristic for N^{3-} in $LaTiO_2N$. The N/Ti ratios determined by XPS (Table 4.4.2) were in good general accord with those obtained by bulk chemical analysis (Table 4.4.1). All samples showed a higher La/Ti ratio than that expected by theory (~1.1), suggesting the surface segregation of La^{3+} accompanied $LaTi_2ON$ formation.

The Ti^{3+}/Ti^{4+} ratios in the $LaTiO_2N$ powders prepared using thiourea as a co-nitriding agent were similar to those of powders prepared using urea as the co-nitriding agent (Fig. 4.4.5(c), Table 4.4.2). Results suggest that an excess of bulk Ti^{3+} species, rather than surface Ti^{3+} species, is responsible for the dark colour of the $LaTiO_2N$ powders prepared using large excesses of thiourea as the co-nitriding agent. An EPR investigation would be useful for quantifying the amount of bulk Ti^{3+} species in the $LaTiO_2N$ powders.

Three distinct sulphur containing species were identified by XPS in the $LaTiO_2N$ powders prepared in the presence of thiourea (Fig.4.4.5(d)). Each species is characterised by a S $2p_{3/2}$ and 2 $p_{1/2}$ doublet, in a characteristic 2:1 peak area ratio with a spin-orbit splitting of 1.25 eV. The binding energy of the S $2p_{3/2}$ feature at 160.9 eV is typical for sulphide species (formally S^{2-}), [46] and is assigned to surface La_2O_2S. This assignment was supported by the fact that this feature intensified progressively as the thiourea content in the precursor mixture increased (c.f. Fig. 4.4.2, where the La_2O_2S impurity phase also intensified progressively with

increasing thiourea content). Species at higher binding energies are readily assigned to sulphite (S $2p_{3/2}$ = 167.2 eV, formally S^{5+}) and sulphate (S $2p_{3/2}$ = 168.9 eV, formally S^{6+}) [46]. This study demonstrates that the combined use of XPS and bulk chemical analyses is a powerful tool for probing the chemical composition of oxynitrides.

4.5 Conclusion

$LaTiO_2N$ powders were successfully synthesized by thermal ammonolysis using urea or thioruea as co-nitriding agents. The addition of urea was highly beneficial in this regard, yielding phase pure $LaTiO_2N$ powders with a higher nitrogen content compared to powders synthesized by ammonolysis in the absence of urea. The use of thiourea as the co-nitriding agent proved less beneficial, due to the concomitant formation of La_2O_2S which adversely impacted the optical properties of $LaTiO_2N$. Results guide the developed of improved and more rapid methods for the synthesis of oxynitride powders.

Chapter 5

Tungsten doped perovskite-type $LaTiO_2N$

5.1 Introduction

Perovskite-type oxynitride having general formula $La_{1.1}(Ti_{1-x},W_x)(O,N)_3$ with different compositions (X = 0.01,0.02,0.03,0.04,0.05) were synthesized by a thermal ammonolysis of oxide precursors prepared via a sol-gel method. Due to their low cost and high colouration efficiency WCl_6 used as a doping material [50,54] (Sun et al., 2014 and Maegli et al., 2014). Recently, the introduction of tungsten has been shown to redshift the bandgap of $LaTiO_2N$ to 2.1 eV. In our previous studies we found the phenomenon that slight excess of titanium over lanthanum ($La_{1-x}Ti_{1+x}O_2N$) reduced the reflectivity in the longer wavelength region after the absorption edge. A molar excess of La relatively to Ti was taken for achieving more reddish coloured W^{6+} doped $LaTiO_2N$ powder. To date, no such study has been reported for the decent tungsten doped $LaTiO_2N$ oxynitride via sol-gel method in an attempt to produce red coloured pigment, motivating a detailed investigation. The aim of this study was to investigate the effect of tungsten doping on the optical properties of $LaTiO_2N$ and in an attempt to produce vivid red pigments. The products formed with different composition were systematically characterized by XRD, SEM-EDS, particle size distribution analysis, UV-vis and oxygen/nitrogen analysis.

5.2 Experimental

$La(NO_3)_3.6H_2O$, titanium isopropoxide, ethylene glycol, citric acid and WCl_6 were obtained from Wako Pure Chemical Industries, Ltd., Japan were used as starting materials. Ammonia gas was obtained from sumitomo Seika Chemicals Co., Ltd., Japan.

A series of five different compositions of perovskite-type $La_{1.1}(Ti_{1-x}W_x)(O,N)_3$, (X= 0.01,0.02,0.03,0.04,0.05) powders were prepared via a sol-gel method with subsequent nitridation by thermal ammonolysis. First, $La(NO_3)_3.6H_2O$ (2.381g, 0.0055mol) and titanium isopropoxide (1.279g, 0.0045mol) were added to ethylene glycol (24.7g) at room temperature with constant stirring. WCl_6 were dissolved in ethanol (20g) and then added into the above solution. A molar excess of La relatively to Ti was taken.

Citric acid (19.1g) and distilled water (20g) were then added to give a homogeneous solution. More details were described in reference (Sarda et al., 2015). Further, prepared precursor was heated under a NH_3 flow of 1dm3/min for 5h at 950℃. After the nitridation was complete, the product was cooled down to room temperature in the furnace. Throughout these experiments, the amount of Lanthanum nitrate hexahydrate was fixed and the molar ratio of the cations (lanthanum, titanium and tungsten) was according to La/Ti/W = 1.1/1-x/x, where the value of x was changed to obtain the desired substitution levels.

5.3 Product characterization

Phase purity was checked by X-ray diffraction (Rigaku Smart lab X-ray diffractometer). The incident X-rays had a wavelength of 1.5406Å (Cu-Kα). XRD data was recorded over the 2θ range 20-80^o operated at 40 kV and 150 mA. Phase identification was made with reference to the JCPDS database. Optical diffuse reflectance spectra were measured with a double beam spectrometer (JASCO V-550DS). The La:Ti ratio of the products was determined by XRF. Anion contents were determined by the hot gas extraction method using a Horiba EMGA-920

analyzer (O/N analyzer). For the analysis, the sample was accurately weighed into a graphite crucible with Ni-Sn as flux and then heated to 3000 °C. Oxygen in the sample was converted into CO while nitrogen evolved in its molecular form. The amount of both gases was determined using infrared and thermal conductivity detectors. Particle size distribution of the oxynitride sample was measured by laser diffraction particle size analyzer (Microtrac HRA X-100). Morphologies and particle size were also evaluated by SEM (Philips XL-30 field emission gun scanning electron microscope). Secondary electron detectors coupled with EDS (Energy-Dispersion Spectroscopy). The SEM-EDS provides detailed imaging information about the morphology and surface texture of individual particles, as well as elements composition of the samples. A relatively low acceleration voltage of 15 kV was used [53] (Lu et al., 2004). Specimens were mounted on black carbon tape and platinum sputter coated for analysis. The surface distributions were collected from SEM images using different magnifications.

5.4 Result and Discussion

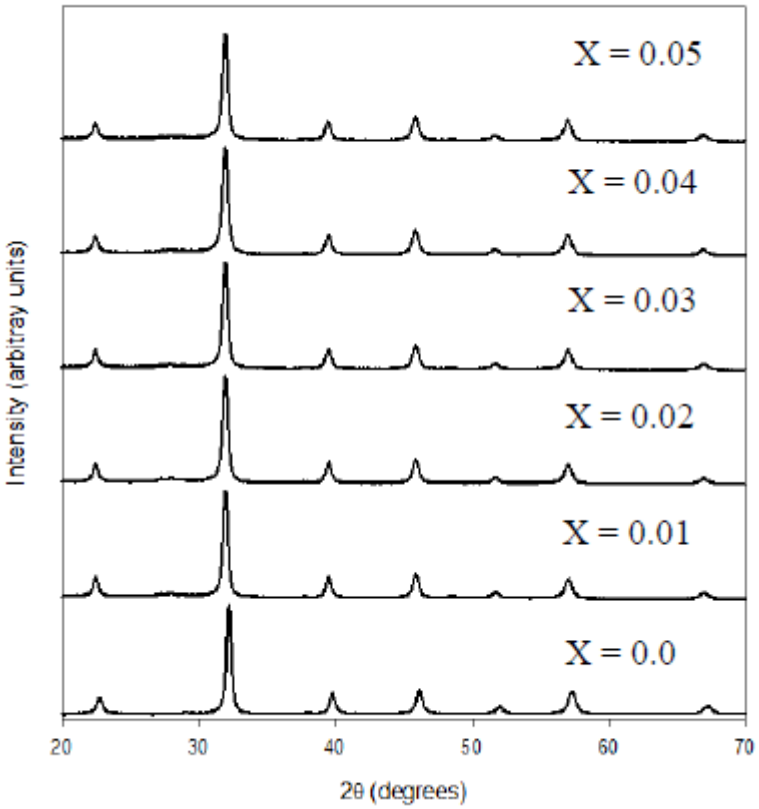

Fig.5.4.1 X-ray powder diffraction patterns of the $La_{1.1}(Ti_{1-x}W_x)(O,N)_3$ powders

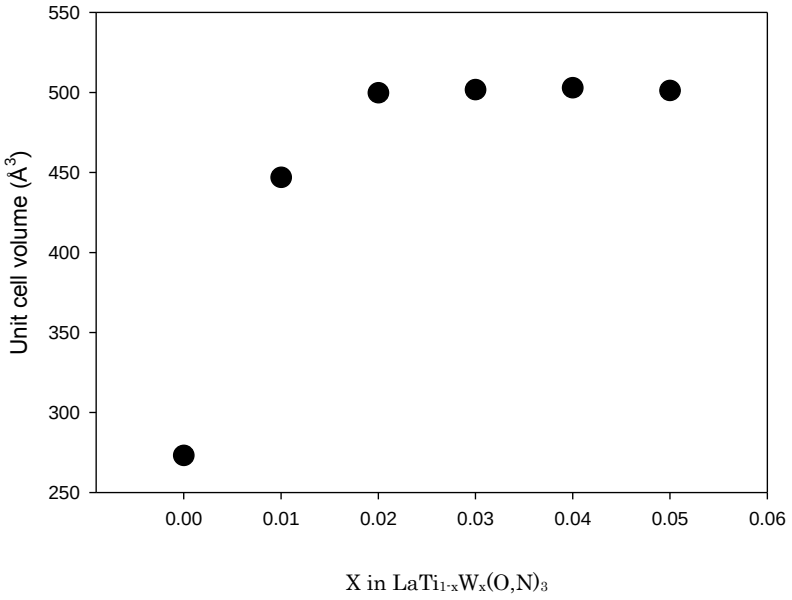

Fig.5.4.2 Unit cell volume of the W^{6+} content in $La_{1.1}(Ti_{1-x}W_x)(O,N)_3$ powders

The powder X-ray diffraction patterns of the $La_{1.1}(Ti_{1-x}W_x)(O,N)_3$, shown in Fig.5.4.1, revealed that all the samples could be assigned to the single phase of the perovskite. No indications for impurity phases were found with increasing doping amount of tungsten. An expansion of the unit cell parameters with increasing tungsten content was observed as a shift of the peak position of the reflections towards lower 2θ angles. Fig.5.4.2 shows that the volume of the unit cell indeed increases with increasing tungsten content. The structural refinements were calculated by CellCalc Ver.2.20 software.

Table 5.4.1 Summarized physical and optical data for $La_{1.1}Ti_{1-x}W_x(O,N)_3$ powders

Sample	Mean particle size (μm)	O (wt.%)	N (wt.%)	O/N	Composition	Colour	E_g (eV)
X = 0.0	8.62	16.11	3.74	3.77	$LaTi(O_{0.79}N_{0.21})_{2.97}$		2.28
X = 0.01	2.83	15.91	3.31	4.21	$La_{1.1}Ti_{0.99}W_{0.01}(O_{0.81}N_{0.19})_{3.12}$		2.19
X = 0.02	3.54	16.81	2.87	5.13	$La_{1.1}Ti_{0.98}W_{0.02}(O_{0.84}N_{0.16})_{3.2}$		2.18
X = 0.03	2.81	16.73	3.42	4.5	$La_{1.1}Ti_{0.97}W_{0.03}(O_{0.82}N_{0.18})_{3.27}$		2.16
X = 0.04	4.64	16.43	3.45	4.17	$La_{1.1}Ti_{0.96}W_{0.04}(O_{0.81}N_{0.19})_{3.25}$		2.19
X = 0.05	1.81	15.94	3.2	4.35	$La_{1.1}Ti_{0.95}W_{0.05}(O_{0.81}N_{0.19})_{3.1}$		2.18

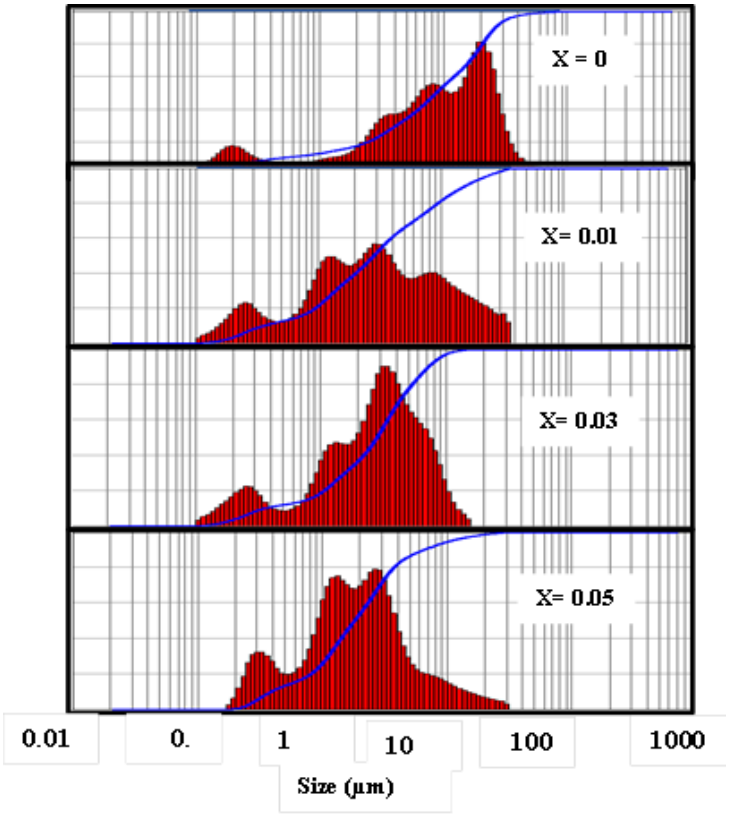

Fig.5.4.3 Particle size distributions of $La_{1.1}Ti_{1-x}W_x(O,N)_3$ where X= 0, 0.01,0.03 and 0.05 respectively

The particle size distribution of the $La_{1.1}(Ti_{1-x}W_x)(O,N)_3$ powders with different compositions is shown in Fig.5.4.3. Median particle sizes are summarized in Table 5.4.1. The median particle size of the $LaTiO_2N$ powder was 8.622µm in the absence of W^{6+}. Tungsten doping reduces the median particle sizes to <4µm. SEM images of the $La_{1.1}(Ti_{1-x}W_x)(O,N)_3$where (X= 0, 0.01, 0.03 and 0.05) are shown in Fig. 5.4.4 respectively. SEM confirmed a decrease in particle size when tungsten doping and excess of La relative to Ti was used in the oxynitride powders (Maegali et al., 2014). From Fig.5.4.4 (b), (c) and (d) it can be observed that, with an increase in the tungsten doping amount from X=0.01 to 0.05, the number of the dispersed particles increased and the finely powdery particles were seen.

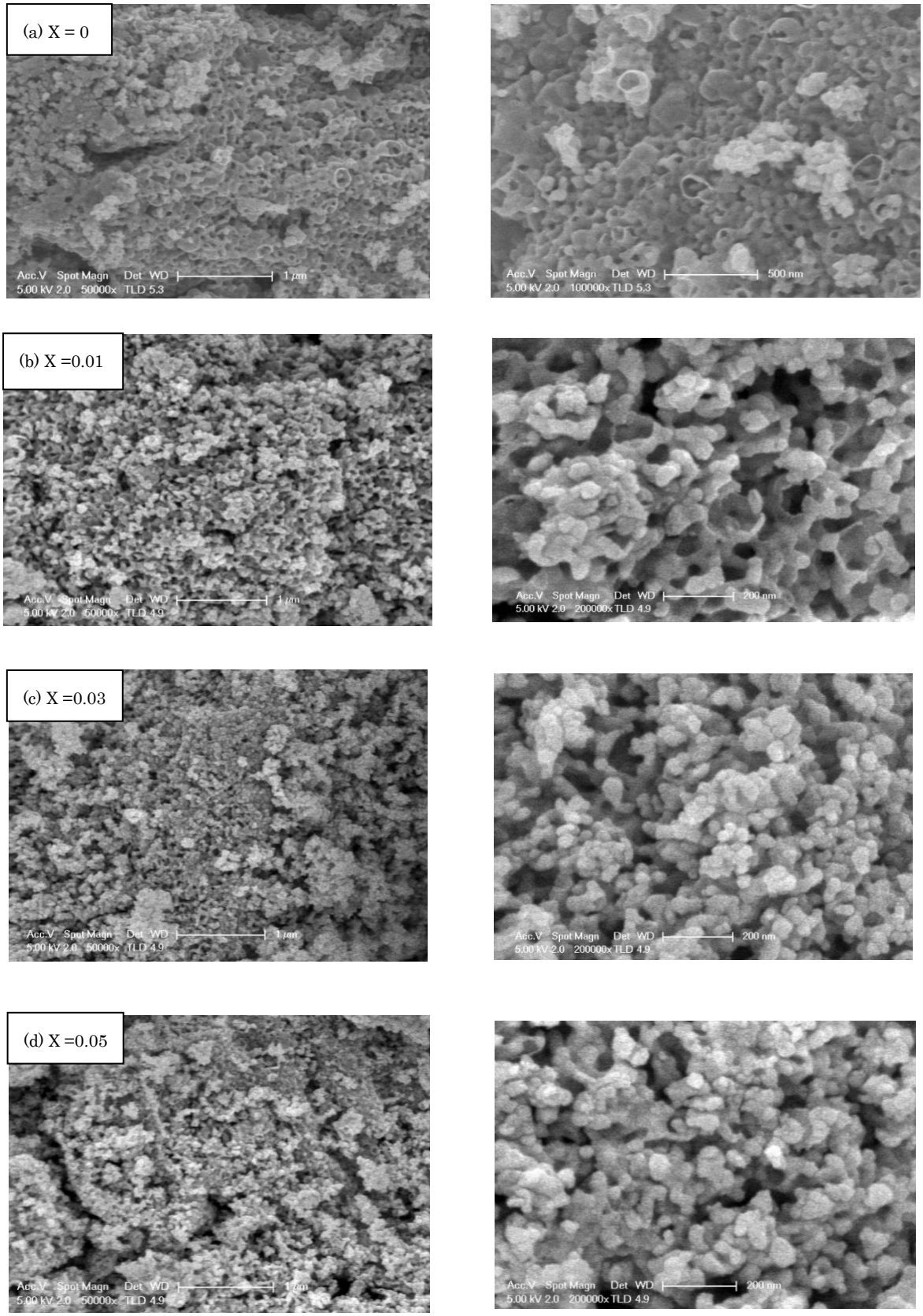

Fig.5.4.4. Scanning electron microscopy (SEM) micrographs of $La_{1.1}(Ti_{1-x}W_x)(O,N)_3$ powders, where (a) x=0, (b) x=0.01, (c) x=0.03 and (d) x= 0.05 respectively

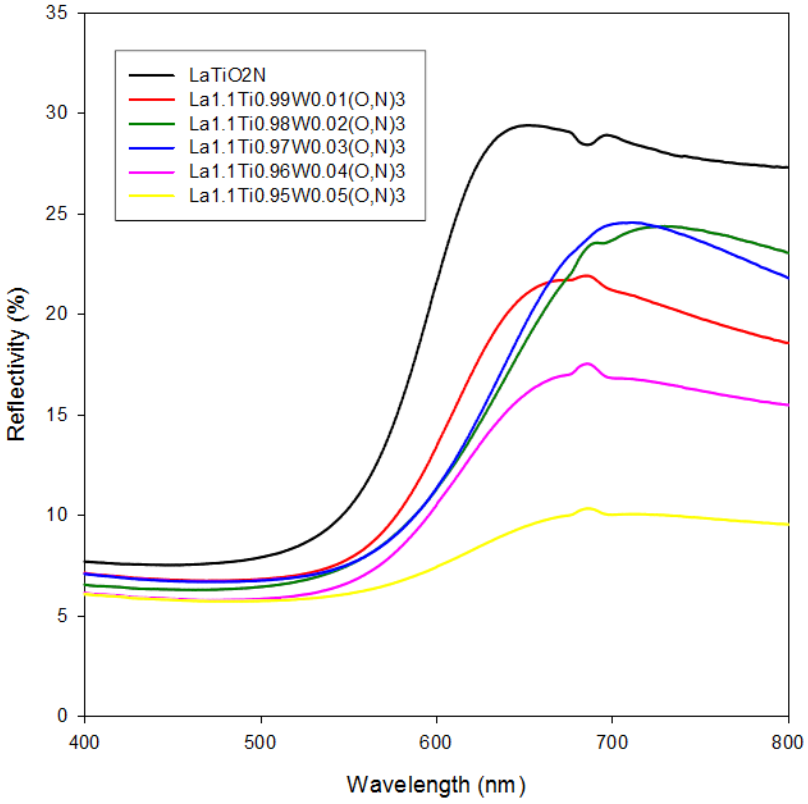

Fig.5.4.5 UV-vis reflectance spectra for $La_{1.1}(Ti_{1-x}W_x)(O,N)_3$

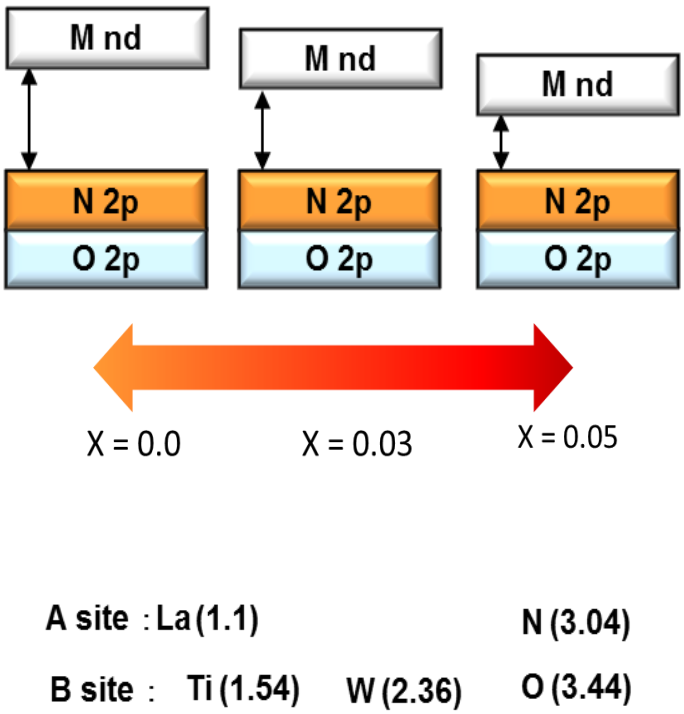

Fig.5.4.6 Schematic sketch of electronegativity of the B cation on the optical bandgap in oxynitride perovskite

The UV-vis absorption spectra of the oxynitride are shown in Fig.5.4.5 In order to compare the absorption edges between the crystalline non doped $LaTiO_2N$ and tungsten doped $La_{1.1}(Ti_{1-x}W_x)(O,N)_3$. Precursor which were prepared for the comparison with their corresponding oxynitrides, showed bandgaps <3eV. This value is higher than the visible light energy, which can explain colourlessness. The optical absorption edge of the $LaTiO_2N$, had a cut of at 545 nm, which correspond to an optical bandgap of 2.28eV. The optical absorption edge of the W^{6+} doped $La_{1.1}(Ti_{1-x}W_x)(O,N)_3$ was extended to 575 nm, which is equivalent to an optical bandgap 2.16 eV. The absorption edge shifts to longer wavelengths is due to they have narrower bandgaps. This results cannot be illustrate by atomic bond distance values, because W^{6+} and Ti^{4+}has almost same ionic radius (0.60Å and 0.605Å) in an octahedral coordination. (Aguiar et al., 2008 and Maegli et. al., 2014) have claimed that, redshift and/or colour changes are not only the nitrogen content, but also from different electronegativities of the B cations. The influence of different electronegativites of the B cations is schematically showed in Fig.5.4.6. showed that as tungsten content increases electronegativity of the B cation increases and it ascribe to decrease in bandgap and/or redshift (Maegli et. al., 2014).

The powder prepared at $La_{1.1}Ti_{0.95}W_{0.05}(O,N)_3$ was of reddish-brown in colour with median particle size <2µm (Table 5.4.1), showed low reflectivity above the absorption edge (Fig.5.4.5) it attributes the presence of a mixed valent state for Ti^{3+}/Ti^{4+}. However, in our previous work we have reported that, when the oxynitrides contained more titanium than stoichiometric composition, resulting in deterioration of reflectivity in the longer wavelengths of the absorption edge and showed the darkening in the colour. Inversely, the oxynitride contained excess of La relative to Ti can endure without affecting the optical properties [52] (Masuda et al., 2009 ,b, and Sarda et al., 2015) .

Table 5.4.2. Elemental composition of $La_{1.1}Ti_{1-x}W_x(O,N)_3$ measured by EDS

Sample	Element Atomic Weight							
	La	**Ti**	**O**	**N**	**Nb**	**W**	**Pt**	**Total**
$La_{1.1}Ti_{0.99}W_{0.01}(O,N)_3$	11.8	9.1	50.5	27.2	0	0.5	0.9	100
$La_{1.1}Ti_{0.98}W_{0.02}(O,N)_3$	11.4	8.4	53.3	25.4	0	0.6	0.9	100
$La_{1.1}Ti_{0.97}W_{0.03}(O,N)_3$	12.7	9.2	50.8	25.3	0	1	1	100
$La_{1.1}Ti_{0.96}W_{0.04}(O,N)_3$	12.3	9	51.2	25.4	0	1.2	0.9	100
$La_{1.1}Ti_{0.95}W_{0.05}(O,N)_3$	12.7	9.4	49.4	26	0	1.5	1	100

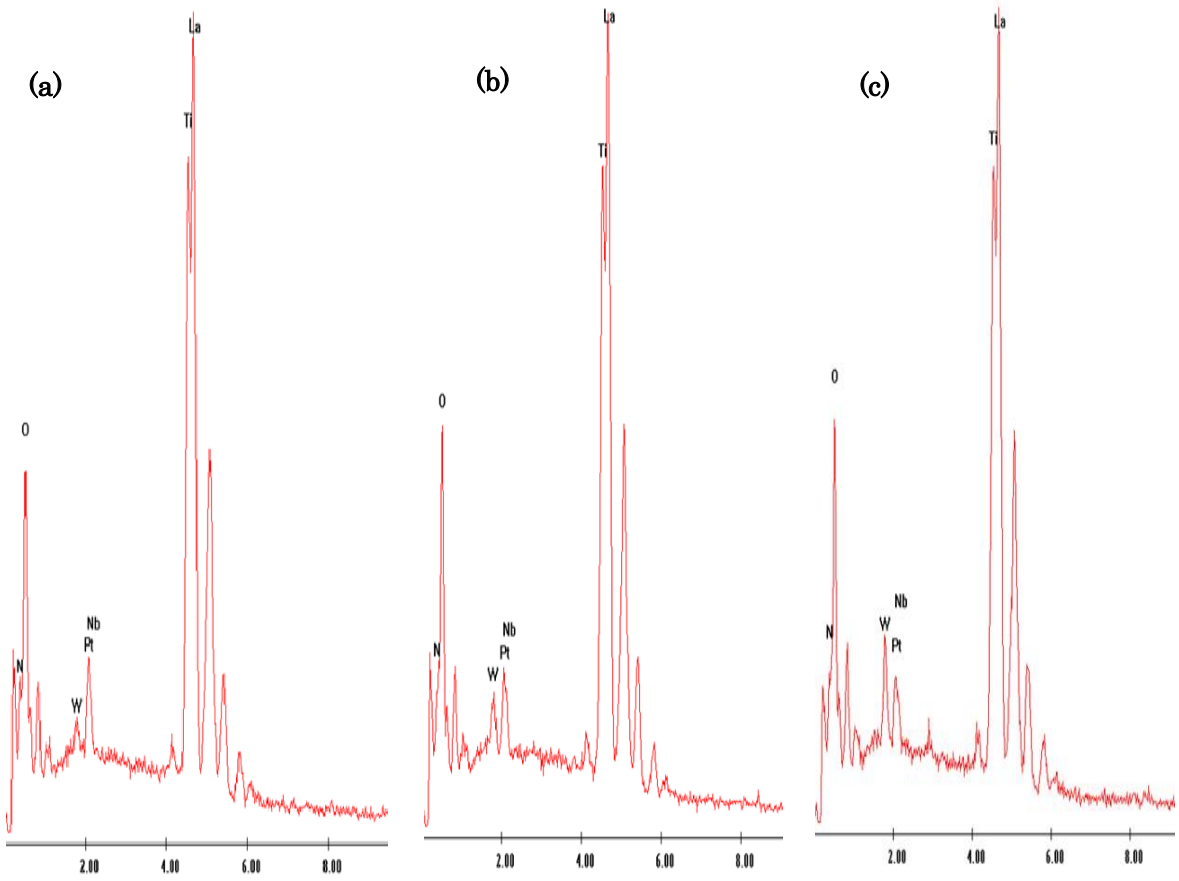

Fig.5.4.7. EDS spectra of (a) $La_{1.1}Ti_{0.99}W_{0.01}(O,N)_3$, (b)$La_{1.1}Ti_{0.97}W_{0.03}(O,N)_3$ and (c)$La_{1.1}Ti_{0.95}W_{0.05}(O,N)_3$

Fig.5.4.7 shows the elemental composition of $La_{1.1}Ti_{1-x}W_x(O,N)_3$,where, (X= 0.01,0.03 and 0.05) were studied by Energy-dispersion spectrometer (EDS) respectively. La, Ti, O and N were found as main elements. Platinum (Pt) was also detected which arises due to platinum coting were used for SEM observation. The elemental compositions obtained by EDS in the (Table 5.4.2) evidence of nitrogen deficiency in all the composition. It has been already reported by (Maegli et al., 2014) the presence of oxygen-rich intermediate-phases on atomic scale and without periodic ordering is possible; therefore such intermediate phases are not detectable by XRD (Aguiar et al., 2008). Results from Table 5.4.1 showed O/N ratio gradually increases with increasing tungsten content. This phenomenon is attributed to the difference in electronegativity between oxygen and nitrogen. The substitution of nitrogen by oxygen, a more electronegative element, involves an increase in iconicity of the bonding.

5.5 Conclusion

Different compositions of perovskite-type $La_{1.1}Ti_{1-x}W_x(O,N)_3$ were synthesized by thermal ammonolysis of oxide precursor prepared by a sol-gel method. There were no deterioration was seen with excess of La on the structural and optical properties of the oxynitride. No impurities were detected by XRD. Appropriate doping of W^{6+} and excess of La relative to Ti in the oxynitride allowed redshifting of the absorption edge. UV-visible diffuse reflectance spectra showed the bandgap in the range of 2.28 eV- 2.16 eV $La_{1.1}Ti_{1-x}W_x(O,N)_3$. Colour of the pigment strongly depends on the light reflection from their surface and materials near inside the surface would hardly contribute to the colour. Therefore, excess of La in the given composition and very small amount of tungsten is fruitful way to increase the brightness of the oxynitride samples. Further work is focused on the XPS and crystal structure of the $La_{1.1}Ti_{1-x}W_x(O,N)_3$ in order to conclude the relationship with its body colour.

Chapter 6

New Synthesis approach of layered perovskite-type Sr_2TaO_3N

6.1 Introduction

Marchand and his coworkers firstly reported inorganic ecofriendly yellow-red pigments having perovskite structure obtained by niobium and tantalum oxynitride[56]. Sr_2TaO_3N was the first example of a Ruddlesden-Popper phase containing only tantalum and an alkaline-earth metal which shows K_2NiF_4-type structure. They have been reported that in order to synthesize perovskite-related Sr_2TaO_3N oxynitride require several NH_3 flow heating cycles such a long-term nitridation as long as 120-300h was required to obtain pure Sr_2TaO_3N [57-58]. However, by our proposed synthesis approach and mechanism, it is possible to make a Sr_2TaO_3N; 2:1 phase within a short period of time. In the present investigation; synthesis of new perovskite-type Sr_2TaO_3N oxynitride by direct Solid state synthesis and the subsequent characterization by X-ray diffraction measurements are studied. From Rietveld refinements, it was found that Sr_2TaO_3N have a K_2NiF_4- type structure with space group I4/mmm which can be described as two dimensional perovskite [56]. Sr_2TaO_3N oxynitride was prepared by reaction between ammonia and the felicitous mixture of alkaline-earth carbonate-tantalum oxide at 1000˚C using two thermal ammonolysis cycles of 24 h with intermediate regrinding. In this study; we have successfully demonstrated that using the oxide precursor, it is possible to make a Sr_2TaO_3N phase within a shorter period of the nitridation and synthesized Sr_2TaO_3N with brighter orange colour than $SrTaO_2N$ than the previous paper reported by Marchant et al. (*J. Solid State Chem.*, **146**: 390-393(1999)).

6.2 Experimental

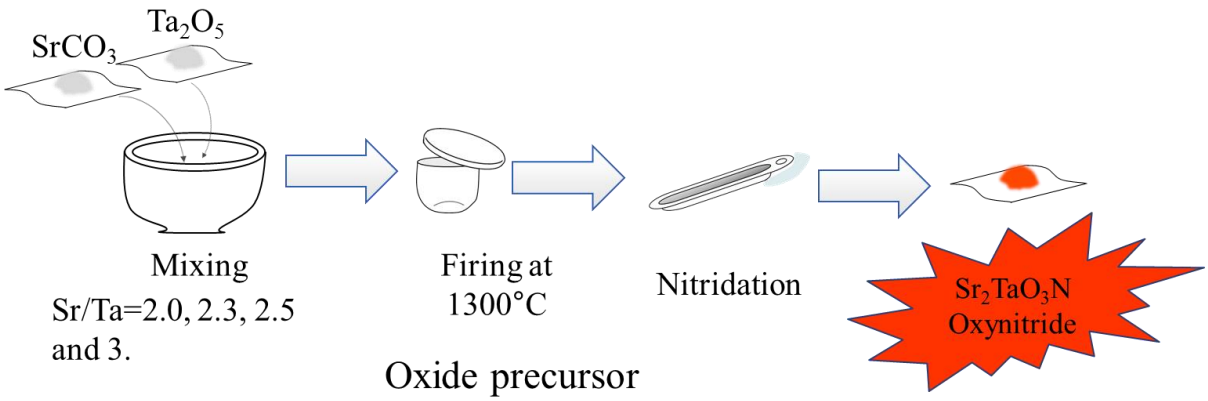

Samples with molar ratios of Sr/Ta = 2, 2.3, 2.5 and 3 were prepared as starting compositions for Sr_2TaO_3N. High-purity strontium carbonate ($SrCO_3$ Kanto Chemicals, 96%) and tantalum oxide (Ta_2O_5 Wako pure Chemicals Co., 99.9%) powders were used. They were mixed for 40 minutes with alumina mortar and pestle, and then fired at 1300˚C in air for 5h. The reactants were nitrided under an NH_3 flow (500ml/min) at 1000˚C for 24 hours. The ammonolysis was repeated twice with an intermediate regrinding. Crystalline phases of the powders were characterized by powder X-ray diffraction (Rigaku SmartLab X-ray diffractometer) with CuKα radiation at a source power of 40 kV and 150 mA. X-ray intensity was monitored by a 1D detector D/tex Ultra 250 [59] and the X-ray data was recorded over the 2θ range of 5-80°. Phase identification was made with a reference to the JCPDS database. The lattice parameters were calculated by CellCalc Ver.2.20 software.

6.3 Results and discussion

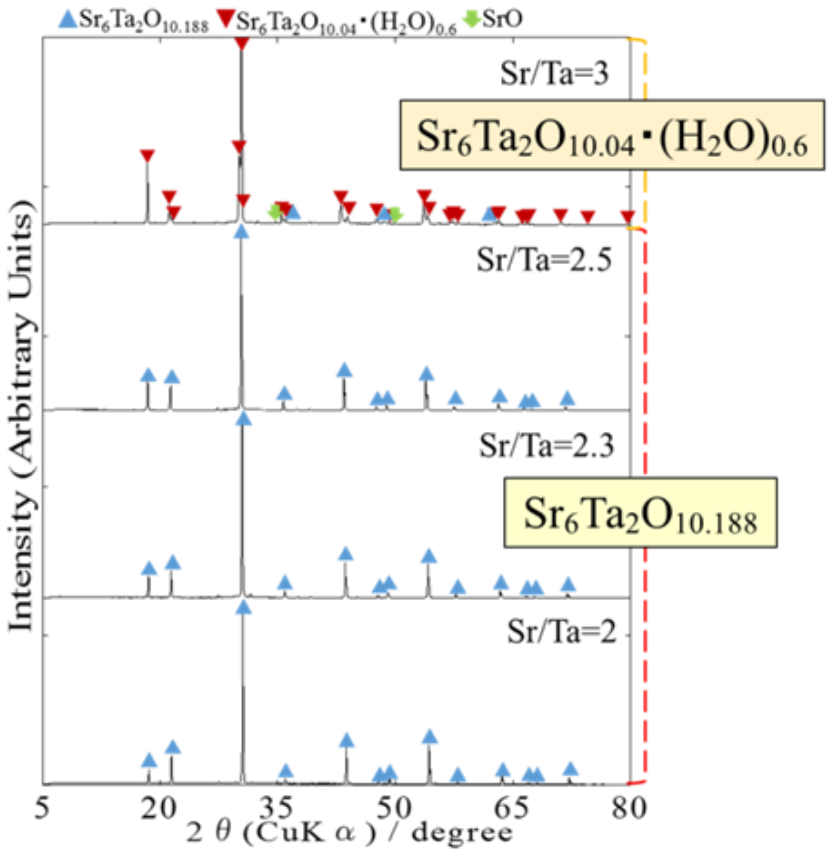

Figure 6.3.1 XRD patterns of oxide precursors for Sr_2TaO_3N, with Sr/Ta=2.0, 2.3, 2.5 and 3.0

Figure 6.3.1 illustrates XRD patterns of the oxide precursors fired at 1300°C in air. From the XRD results it was confirmed that monophasic, cubic $Sr_6Ta_2O_{10.188}$ were obtained for $2 \leq Sr/Ta \leq 2.5$, independent of their composition, while at Sr/Ta=3, the orthorhombic $Sr_6Ta_2O_{10.04} \cdot (H_2O)_{0.6}$ were formed. The cubic $Sr_6Ta_2O_{10.188}$ would possess a considerable amount of Sr-deficiency distributed statistically.

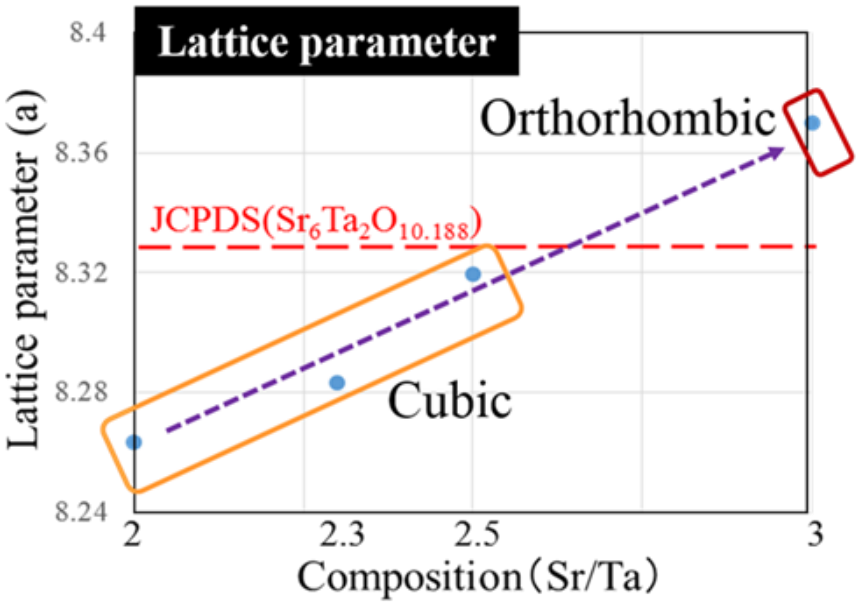

Figure 6.3.2 Lattice parameter a of the oxide precursors as a function of Sr/Ta

Figure 6.3.2 shows lattice constant a of the products, where the hypothetical lattice constant for the orthorhombic oxide $Sr_6Ta_2O_{10.04}\cdot(H_2O)_{0.6}$ at Sr/Ta=3 was calculated from the volume, using a geometric mean of obtained lattice parameters. The parameters varied linearly as a function of Sr/Ta, and the plot of the geometric mean of the orthorhombic parameters for Sr/Ta=3 was located on a linear extrapolation of the relationship.

The XRD patterns showed in Figure 6.3.3 correspond to phase identification of the products after 24h nitridation. At Sr/Ta=3.0, the peaks at 2θ=14° and 31° were unique in Sr_2TaO_3N. The doublet peaks with the first and second strongest intensities around 2θ =31° indicated that Sr_2TaO_3N was the major phase in the product. The relative intensities appeared in the doublet peaks are the same as reported in JCPDS card No. 01-072-7943 for $Sr_6Ta_2O_{10.188}$. At $2.0 \leq Sr/Ta \leq 2.5$, the peaks characteristic of Sr_2TaO_3N were very weak and major peaks could be assigned to $Sr_6Ta_2O_{10.188}$. The strongest peak around 2θ =31° is common to both singlet peak for Sr_2TaO_3N (JCPDS No. 01-089-8340) and one of the doublet peaks for $Sr_6Ta_2O_{10.188}$. However, the accompanied peak neighbor to the strongest one was significantly weak and the position was consistent with the strongest peak of $SrTaO_2N$

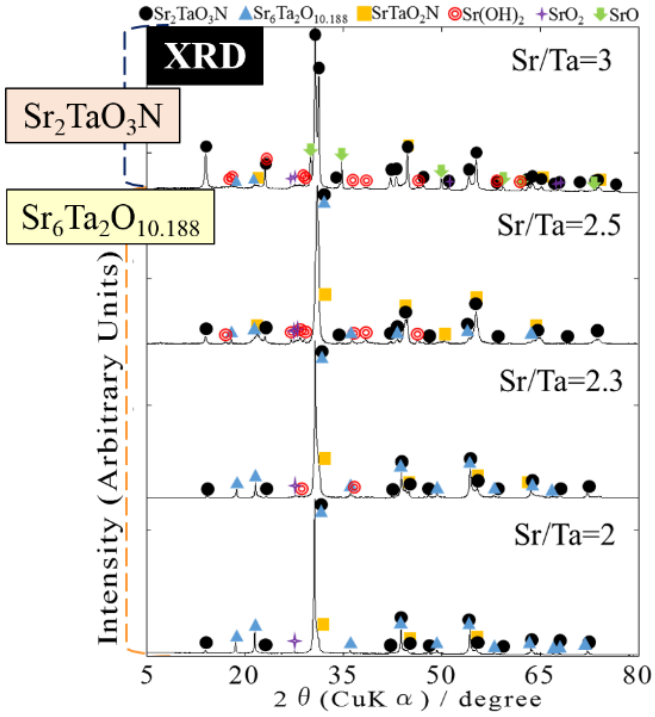

Figure 6.3.3 XRD patterns of products after 24h nitridation

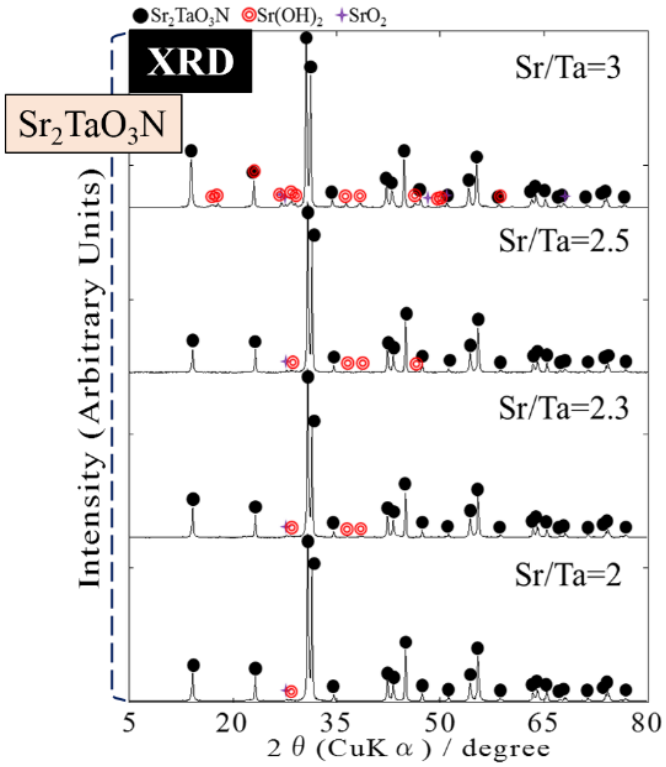

Figure 6.3.4 XRD patterns of products after 48h nitridation

(JCPDS card No. 01-078-1457). It means that the formation of $SrTaO_2N$, in which Sr/Ta=1, was detected even in the strontium-rich product with Sr/Ta≥2.0. From Figure 6.3.4 it was found that the final major products should be Sr_2TaO_3N and strontium oxide/hydroxide as a byproduct for all the compositions. Amount of the strontium oxide/hydroxide seemed to increase in proportional to the excess amount of weighed strontium carbonate against tantalum. However, the observed lattice parameters a and c for Sr_2TaO_3N for 2.0≤Sr/Ta≤2.5 after 48h nitridation were identical within an experimental error (a=4.033(2)Å, 4.032(2)Å and 4.032(2)Å; c=12.565(8)Å, 12.568(8)Å and 12.564(9)Å; for Sr/Ta=2, 2.3 and 2.5, respectively)

From the above mentioned observations there were two possible formation mechanisms of Sr_2TaO_3N can be proposed.

At Sr/Ta = 2

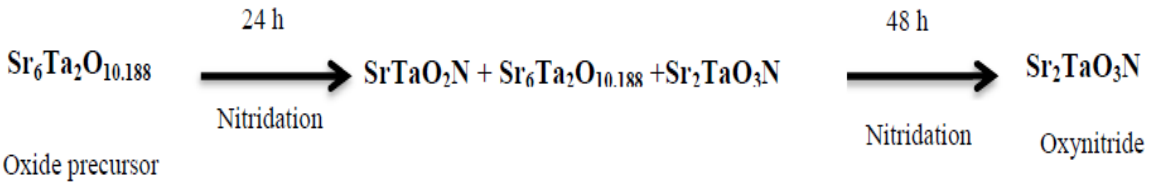

$Sr_6Ta_2O_{10.188}$ as an oxide precursor was prepared by firing a mixture of $SrCO_3$ and Ta_2O_5 with Sr/Ta=2 at 1300˚C. After the first 24h nitridation, $SrTaO_2N$ and $Sr_6Ta_2O_{10.188}$ were detected besides Sr_2TaO_3N. After 48h nitridation, almost single phase of Sr_2TaO_3N was detected since Sr-poor $SrTaO_2N$ would react with Sr-rich $Sr_6Ta_2O_{10.188}$ to form Sr_2TaO_3N.

At Sr/Ta = 3

$$\underset{\text{Oxide precursor}}{Sr_6Ta_2O_{10.04}\cdot(H_2O)_{0.6}} \xrightarrow[\text{Nitridation}]{} Sr_2TaO_3N + SrO,\ Sr(OH)_2$$

$Sr_6Ta_2O_{10.04}\cdot(H_2O)_{0.6}$ as an oxide precursor was obtained when a mixture of $SrCO_3$ and Ta_2O_5 with Sr/Ta=3 was taken. In this reaction during first cycle of nitridation XRD results illustrate Sr_2TaO_3N oxynitride was obtained as a major product. After 48h ammonolysis the oxide precursor was successfully converted into Sr_2TaO_3N, but $Sr(OH)_2$ and/or SrO_2 impurity phase remained in the product. It seemed that Sr-rich composition was favorable to promote the formation of Sr_2TaO_3N.

The obtained Sr_2TaO_3N showed brighter reddish-orange colour than $SrTaO_2N$ though the former oxynitride contains less nitrogen than the latter oxynitride. It is possible that an insertion of SrO layer between the perovskite-type $SrTaO_2N$ unit in the crystal structure of Sr_2TaO_3N would relax the stresses/distortions in the perovskite unit induced by a size mismatch between the constituent ions, so that Sr_2TaO_3N would possess more covalent character in bonding [30] and the bandgap would be shrunk enough to show redder colour.

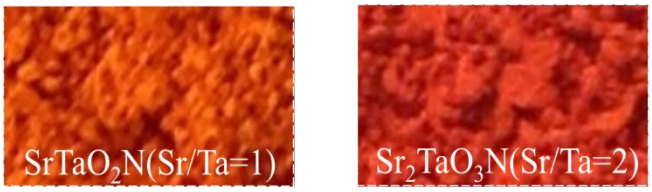

Figure 6.3.5 Photos of $SrTaO_2N$ and Sr_2TaO_3N oxynitride

6.4 Conclusion

Layered perovskite Sr_2TaO_3N could be synthesized after as a short duration as 24-48h nitridation of $Sr_6Ta_2O_{10.188}$ at 1000°C with NH_3, showing redder colour than $SrTaO_2N$. Excess amount of Sr would promote the formation of Sr_2TaO_3N.

Summary and Conclusion

This work is divided into 6 chapters. Introduction and literature survey were briefly discussed in chapter 1. Chapter 2 describes the analysis techniques used to characterize the oxide and oxynitride samples. Chapter 3 explains photoluminescence properties of $(Ba_{1-(x+y)}Sr_xEu_y)_2Si_6O_{12}N_2$ phosphors for white LED application. In this work $(Ba_{1-(x+y)}Sr_xEu_y)_2Si_6O_{12}N_2$ oxynitride phosphors were successfully synthesized by the solid-state reaction method at 1200°C under a H_2(5%) + N_2(95%) atmosphere. The Sr^{2+} content (x) was varied in the range 0-0.6 and the Eu^{2+} content varied in the range 0.05-0.25, with the Si/(Ba+Sr+Eu) ratio fixed at 3. Results show that the emission characteristics of $(Ba_{1-(x+y)}Sr_xEu_y)_2Si_6O_{12}N_2$ phosphors under UV or blue-light excitation was strongly dependent on the chemical composition. The phosphor $(Ba_{0.95}Eu_{0.05})_2$ $Si_6O_{12}N_2$ showed an intense green emission peak at 520 nm, whilst the phosphor $(Ba_{0.45}Sr_{0.5}Eu_{0.05})_2Si_6O_{12}N_2$ had a weaker emission maximum at 548 nm. Ba^{2+} substitution with Sr^{2+} decreased the lattice volume of the $(Ba_{1-(x+y)}Sr_xEu_y)_2Si_6O_{12}N_2$ phosphors and was responsible for the redshift in the emission peak. Optimization of the Eu^{2+} concentration at a fixed Sr^{2+} content of 0.2 identified the phosphor $(Ba_{0.65}Sr_{0.2}Eu_{0.15})_2Si_6O_{12}N_2$ as a potential alternative to YAG:Ce yellow phosphors for white LED applications.

Chapter 4 describes the structural and optical properties of perovskite-type LaTiO2N which is synthesized by using co-nitriding agents such as, Urea and thiourea. In this study, Perovskite-type $LaTiO_2N$ powders were successfully synthesized by thermal ammonolysis of $La_2Ti_2O_7$ at 950 °C in the presence of urea or thiourea as co-nitriding agents. The products formed at different $La_2Ti_2O_7$:urea or $La_2Ti_2O_7$:thiourea mass ratios were systematically characterized by SEM, XRD, particle size distribution analysis, BET, UV-Vis, XPS and O/N analysis. Results show that the addition of urea is highly beneficial for $LaTiO_2N$ synthesis,

yielding pure phase products with higher nitrogen content than $LaTiO_2N$ powders prepared in the absence of urea. Conversely, the addition of thiourea was detrimental to the structural and optical properties of $LaTiO_2N$, due to the formation of La_2O_2S as a side-product. La_2O_2S formation resulted in a sub-stoichiometric La:Ti ratio in the $LaTiO_2N$ products, which dramatically lowered the reflectivity of the product powders above the absorption edge due to excess bulk Ti^{3+} centers. Urea or thiourea addition also decreased the median particle size of the $LaTiO_2N$ powders.

Chapter 5 is based on the optical studies of decent tungsten doped $LaTiO_2N$ by sol-gel methodology. In this investigation, Perovskite-type oxynitride having general formula $La_{1.1}(Ti_{1-x},W_x)(O,N)_3$ with different compositions (X=0.01,0.02,0.03,0.04,0.05) were synthesized by a thermal ammonolysis of oxide precursors prepared via a sol-gel method. Crystal structure and morphological changes of the microstructure with increasing tungsten content has been studied. Appropriate doping of W^{6+} and excess of La relative to Ti in the oxynitride allowed redshifting of the absorption edge were seen. Among all $La_{1.1}(Ti_{1-x},W_x)(O,N)_3$ compositions (X = 0.03) showed the highest redshift with decreasing bandgap.

Chapter 6 is about formation process of the new layered perovskite Sr_2TaO_3N oxynitride having a K_2NiF_4-type structure from oxide precursor of $Sr_6Ta_2O_{10.188}$ was examined under an ammonia flow. Using the oxide precursor, it is possible to make a Sr_2TaO_3N phase within a shorter period of the nitridation than the previous paper reported by Marchant et al. Excess amount of strontium deviated from the stoichiometric composition of Sr/Ta=2 also seemed to promote the formation of Sr_2TaO_3N under the ammonia flow. The synthesized Sr_2TaO_3N after two cycles of 24h-nitridation of the oxide precursors showed brighter reddish-orange colour than $SrTaO_2N$.

In conclusion, this research studies shows several creative work in the oxynitride

perovskite field. The investigations gave a better understanding of the Synthesis, Optical and Structural properties of oxynitride. Synthesis techniques/experimental set-up were developed to obtain homogeneous nitridation in short period of time. It was demonstrated that $LaTiO_{2+x}N_{1-x}$ and $(Ba_{1-(x+y)}Sr_xEu_y)_2Si_6O_{12}N_2$ oxynitride have a diversity of potential applications as non-toxic pigments and phosphor for white LED application. Comparative study on the oxide and oxynitride complex perovskites, the effect of mixed O/N anions on the cation ordering and bandgap have been examined. This research work thus opens a number of different opportunities for future investigations in the synthesis and study of optical properties of the oxynitride powders.

References

1. R. J. Xie, N. Hirosaki, K. Sakuma, Y. Yamamoto and M.Mitomo, Appl. Phys. Lett., 84, 54045406 (2004).
2. T. Suehiro, N. Hirosaki, R. J. Xie and M. Mitomo, Chem.Mater., 17, 308314 (2005)
3. K. Maeda, T. Takata, M. Hara, N. Saito, Y. Inoue and H. Kobayashi, J. Am. Chem.Soc. 2005, 127, 8286.
4. K. Maeda and K. Domen, J. Phys. Chem. C, 111, 78517861 (2007).
5. M. Jansen and H. P. Letschert, Nature 2000, 404, 980.
6. Pérez-Estébanez, R. Pastrana-Fábregas, J. Isasi-Marín and R. Sáez-Puche, J.Mater. Res. 2006, 21, 1427.
7. Y. I. Kim, P. M. Woodward, K. Z. Baba-Kishi and C. W. Tai,Chem. Mater., 16, 12671276 (2004).
8. E. Guenther and M. Jansen, Mater. Res. Bull. 2001, 36, 1399.
9. Kasahara A, Nukumizu K, Hitoki G, Takata T, Kondo J N, Hara M, Kobayashi H and Domen K 2002 J. Phys. Chem. A 106 6750
10. Moriga T, Aoki D, Nishida Y, Kitaji K, Takahara K, Murai K and Nakabayashi I 2006 phys. stat.sol. (a) 203 2818
11. Rong-Jun Xie and Hubertus T. (Bert) Hintzen, Optical Properties of (Oxy) Nitride Materials: A Review J. Am. Ceram. Soc., 96 [3] 665‑687 (2013)
12. L. Katz and R. Ward, Inorg. Chem. 3 (1964) 205-211.
13. J.B. Goodenough and J.A. Kafalas, J. Solid State Chem. 6 (1973) 493-501.
14. R. H. Mitchell, Perovskites: Modern and Ancient, Almaz Press Inc., Ontario 2002.
15. V. M. Goldschmidt, Skrifer Norske Videnskaps-Akad. Oslo, I. Mat.-Nat. Kl. 8 (1926).
16. Mark T. Weller oxford science publications book page 48.

17. C. Li, K. K. S. Chi and Ping Wu, J. Alloy. Compd. 2004, 372, 1, 40.

18. C. Braun, M. Seibad, S. L. Bcrger, O. Oeckler, T. D. Boyko, A. Moewes, G. Miehe, A. Tucks and W. Schnick. (2010). Material Properties and Structural Characterization of $M_3Si_6O_{12}N_2$:Eu2 (M=Ba, Sr)—A Comprehensive Study on a Promising Green Phosphor for pc-LEDs. Chem.Eur.J.2010, 16, 9646-9657.

19. R.J. Xie, N. Hirosaki. (2007, Oct.). Silicon-based oxynitride and phosphors for white LEDs – A review. Science and Technology of Advanced Materials 8 (2007) 588-600.

20. Y.H. Song, T.Y. Choi, K. Senthil, T. Masaki, D.H. Yoon. (2011, July). Photoluminescence properties of green-emitting Eu^{2+}-activated $Ba_3Si_6O_{12}N_2$ oxynitride phosphor for white LED applications. Materials Letters 65 (2011) 3399-3401.

21. P. F. Smet, J. botterman, K. Vander Eeckhout, K. Korthout and D. Poelman. (2014, June). Persistent luminescence in nitride and oxynitride phosphors: A review. Opt. Mater. 36 (2014) 1913-1919.

22. R. Zhang, M. Numata, T. Maea, Y. Akazawa, K. Murai and T. Moriga. (2010, June). Preparation And Luminescence Properties of Eu^{2+}- Activated Ba-Six-O-N Phosphors. Int. J. Mod.Phys. B24 (2010) 3221.

23. M. Mikami, H watanabe, K. Uheda, S. Shimooka, Y. Shimomura, T. Kurushim and N. Kijima.(2009). New Phosphors for white LEDs: Material Design Concepts. Materials Sci and Eng.1. (2009)012002.

24. T. Moriga, R. Zhang, N. Mastsuura, T. Maeda, M. Numata, K. Murai and K. Nakamura. (2011). The peak shift due to a barium deficiency in the Al-27 MAS-NMR spectrum for Eu^{2+}-activated barium aluminum silicon oxynitride phosphors J. Ceram. Proc. Res. 12 (2011) S23-S25.

25. P. Villars, K. Cenzual, J. Daams, R. Gladyshevskii, O. Shcherban, V. Dubenskyy, V. Kuprysyuk, I. Savysyu, $Ba_3Si_6O_9N_4$, Z. Anorg. Allg. Chem. 632 (2006) 949.

26. W.Li, R. Xie, T. Zhou, L. Liu and Y. Zhu. (2014, Jan.). Synthesis of the phase pure $Ba_3Si_6O_{12}N_2$:Eu^{2+} green phosphor and its application in high color rendition white LEDs. Dalton Trans., 2014,43,6132.
27. Y. Lu, G. Shi, Q. Zhang, H. Wang, Y. Li. (2011, Dec.). Photoluminescence properties of Eu^{2+} and Mg^{2+} co-doped $CaSi_2O_2N_2$ phosphor for white light LEDs. Ceramics international 38 (2012) 3427-3433.
28. Klocken R, von Bohlen A. Analytical characterization of artists' pigments used in old and modern paintings by total-reflection X-ray fluorescence. Spcctrochim Acta 1993; 48B(2): 239-246.
29. Aguiar R, Logvinovich D, Weidenkaff A, Rachel A, Reller A, Ebbinghaus SG. The vast colour spectrum of ternary metal oxynitride pigments. Dyes and Pigments 2008; 76:70 -75.
30. Jansen M, Letschert HP. Inorganic yellow-red pigments without toxic metals. Nature 2000; 404:980-982.
31. Fuertes A. Chemistry and applications of oxynitride perovskites. J Mater Chem 2012; 22:3293-3299.
32. Ebbinghaus SG, Abicht HP, Dronskowski R, Muller T, Reller A, Weidenkaff A. Perovskite-related oxynitride – Recent developments in synthesis, Characterisation and investigations of physical properties. Prog Solid State Chem 2009; 37:173-205.
33. Tessier F, Maillard P, Chevire F, Domen K, Kikkawa S. Optical properties of oxynitride powders. J Ceram Soc Jpn 2009; 117(1):1-5.
34. Clarke SJ, Guinot BP, Michie CW, Calmont MJC, and Rosseinsky MJ. Oxynitride Perovskites: Synthesis and structures of $LaZrO_2N$, $NdTiO_2N$ and $LaTiO_2N$ and comparison with oxide perovskites. Chem Mater 2002; 14: 288- 294.
35. Masuda Y, Mashima R, Ikeuchi K, Murai K, Waterhouse GIN, Metson JB, Moriga T.

Relationship between anion and cation nonstoichiometries and valance state of titanium in perovskite-type oxynitrides $LaTiO_2N$. J Ceram Soc Jpn 2009;117:76-81.

36. Moriga T, Ikeuchi K, Mashima R, Aoki D, Murai K. Influence of cation nonstoichiometry on the optical properties of the perovskite-type Oxynitride $LaTiO_2N$. J Ceram Soc Jpn 2007; 115(10):601-603.
37. Moriga T, Aoki D, Nishida Y, Kitaji K, Takahara K, Murai K, Nakabayashi I. Blue-shift of absorption edge in $LaTiO_2N$ by controlling the anion nonstochiometry. Phys Stat Sol 2006; 203(11), 2818-2822.
38. Maegli AE, Otal EH, Hisatomi T, Yoon S, Leroy CM, Schauble N, Lu Y, Gratzel M, Weidenkaff A. Perovskite-type $LaTiO_2N$ for solar water splitting: Influence of the synthesis conditions. Energy Proc. 2012; 22:61-66.
39. Luo W, Li Z, Jiang X, Tao Yu, Liu L, Chen X, Ye J, Zou Z. Correlation between the band positions of $(SrTiO_3)_{1-x}.(LaTiO_2N)_x$ solid solutions and photocatalytic properties under visible light irradiation. Phys Chem Chem Phys 2008; 10:6717-6723.
40. Chevire F, Tessier F, Marchand R. Optical properties Solid solution $LaTiO_2N$-$ATiO_3$ (A=Sr,Ba). Eur J Inorg Chem 2006, 1223-1230.
41. Marozau I, Shakabo A, Dobeli M, Lippert T, Logvinovich D, Mallepell M, Schneider CW, Weidenkaff A, Wokaun A. Optical properties of nitrogen-substituted strontium titanate thin films prepared by pulsed laser deposition. Materials 2009; 2:1388-1401.
42. Logvinovich D, Borger A, Dobeli M, Ebbinghaus SG, Reller A, Weidenkaff A. Synthesis and physical chemical properties of Ca-substituted $LaTiO_2N$. Prog Solid State Chem 2007, 35, 281-290.
43. Maegli AE, Sagarna L, Populoh S, Penkala B, Otal EH, Weidenkaff A. Optical and transport properties of $LaTi_{1-x}M_x(O,N)_3$ (x=0; 0.1, M = Nb^{5+}, $W^{6+)}$ thin films prepared by plasma ammonolysis. J Solid State Chem 2014; 211:106-112.

44. Gomathi A, Reshma S, Rao CNR. A simple urea-based route to ternary metal oxynitride nanoparticles. J Solid State Chem 2009; 182:72-76.
45. Descostes M, Mercier F, Thromat N, Beaucaire C, Gautier-Soyer M. Use of XPS in the determination of chemical environment and oxidation state of iron and sulfur samples: constitution of a data basis in binding energies for Fe and S reference compounds and applications to the evidence of surface species of an oxidized pyrite in a carbonate medium. Appl Surf Sci 2000; 165:288-302.
46. Chen, D., Habu, D., Masubuchi, Y., Torii, S., Kamiyama, T., Kikkawa, S. 2015. Partial nitrogen loss in $SrTaO_2N$ and $LaTiO_2N$ oxynitride perovskites. Solid State Sciences; 2015.08.18.
47. Sarda, N. G., Fujigaki, H., Ogita, Y., Chan, A., Murai, K., Waterhouse, G. I. N. and Moriga T. 2016. Photoluminescence Properties of $(Ba_{1-(x+y)}Sr_xEu_y)_2Si_6O_{12}N_2$ Phosphors for White LED Applications. J. Nano Res., 36: 1-7.
48. Wendusu, Masui, T., Imanaka, N. 2014. Novel environment-friendly inorganic red pigments based on $(Bi, Er, Y, Fe)_2O_3$ solid solutions. J. As. Ceram Soc., 2: 195–198.
49. Sun, S., Masubuchi, Y., Motohashi, T., Kikkawa, S. 2014. Direct synthesis of nearly single-phase $BaTaO_2N$ and $CaTaO_2N$ powders. J. Eur. Ceram. Soc., 35 (12).
50. Ozkan, E., Tepehan., F.Z. 2001. Optical and structural characteristics of sol-gel-deposited tungsten oxide and vanadium-doped tungsten oxide. Sol. Energy Mater. Sol. Cells; 68:265-277
51. Sarda, N. G., Omune, M., Hayashi, T., Chan, A., Kataoka, S., Murai, K., Waterhouse, G. I.N., Moriga, T. 2015. Structural and optical properties of perovskite-type $LaTiO_2N$ synthesized using urea or thiourea as co-nitriding agents. J. Eur. Ceram. Soc., 35: 3311–3317.

52. Lu, J., Rozgonyi, G., Rand, J., Jonczyk, R. 2004. Secondary phase inclusions in polycrystalline sheet silicon. J. Crys. Gro., 269:599–605.
53. Aguiar, R., Kalytta, A., Reller, A., Weidenkaff, A. and Ebbinghaus, S. G. 2008. Photocatalytic decomposition of acetone using $LaTi(O,N)_3$ nanoparticles under visible light irradiation. J. Mater. Chem., 18: 4260-4265.
54. Pan, C., Tanaka, T., Nakabayashi, M., Matsumoto, T., Shibara, N., Ikuhara, Y., and Domen, K., "A complex perovskite-type oxynitride: the first photocatalyst for water splitting operable at up to 600nm," Angew. Chem. Int. Ed. Engl.; 54:2955-2959 (2015).
55. Masubuchi, Y., Sun, S. –K., and Kikkawa, S., "Processing of dielectric oxynitride perovskites for powders, ceramics, compacts and thin films," Dalton Trans., 44:10570-10581 (2015).
56. N. Diot, R. Marchand, J. Haines, J. M. Leger, P. Macaudiere and S. Hull, , "Crystal Structure Determination of the Oxynitride Sr_2TaO_3N," J. Solid State Chem., 146: 390-393(1999).
57. G. Tobias, J. Oro-Sole´, D. Beltran-Porter and A. Fuertes, "Synthesis and crystal structure of novel Ruddlesden–Popper strontium niobium oxynitrides," Crystal Engineering, 5: 479–485 (2002).
58. Dr. L. Le Gendre (private communication).
59. Product information on High-speed X-ray detector with high energy resolution D/tex Ultra, Rigaku Journal (in Japanese), 39:41-42 (2008).
60. H.J. Lee, K.P. Kim, J.S. Yoo, I.W. Park, H.J.Lee, and S.D.Hwang "Optical Properties of Green/red emitting Oxynitride Phosphors synthesized at Low Temperature for LED application," 217th ECS Meeting, Abstract #1469, © The Electrochemical Society.

61. http://www.horiba.com/fileadmin/uploads/Scientific/Documents/Emission/EMGA35.pdf

62. Zoran Stojanovic and Smilja Markovic, “Determination of Particle Size Distributions by Laser Diffractions,” Technics-New Materials, 21: 11–20, (2012).

63. http://www.dsimagingllc.com/courses/

64. Toshihiro Moriga, “Perovskite-type (La,Sr)TiO_2N Oxynitrides Showing a Rainbow Color Changing in Accordance with the Composition,” Journal of the Japan Society of Colour Materials, Vol.83, 115-120, (2010).

65. https://www3.nd.edu/~nsl/Lectures/phys10262/art-chap2-1.pdf

66. V. C. Albarici, PhD Thesis, UFSCar, Sao Carlos, Brazil (2004).

67. http://www.chem.sc.edu/faculty/zurloye/xrdtutorial_2013.pdf